



HAL
open science

Optical traps for Ultracold Metastable Helium atoms

Juliette Simonet

► **To cite this version:**

Juliette Simonet. Optical traps for Ultracold Metastable Helium atoms. Atomic Physics [physics.atom-ph]. Université Pierre et Marie Curie - Paris VI, 2011. English. NNT: . tel-00651592

HAL Id: tel-00651592

<https://theses.hal.science/tel-00651592>

Submitted on 13 Dec 2011

HAL is a multi-disciplinary open access archive for the deposit and dissemination of scientific research documents, whether they are published or not. The documents may come from teaching and research institutions in France or abroad, or from public or private research centers.

L'archive ouverte pluridisciplinaire **HAL**, est destinée au dépôt et à la diffusion de documents scientifiques de niveau recherche, publiés ou non, émanant des établissements d'enseignement et de recherche français ou étrangers, des laboratoires publics ou privés.

DÉPARTEMENT DE PHYSIQUE
DE L'ÉCOLE NORMALE SUPÉRIEURE
LABORATOIRE KASTLER-BROSSEL



THÈSE DE DOCTORAT DE L'UNIVERSITÉ PARIS VI
Spécialité : Physique Quantique
présentée par

Juliette SIMONET

Pour obtenir le grade de
Docteur de l'Université Pierre et Marie Curie (Paris VI)

Sujet de la Thèse:

Optical traps for Ultracold Metastable Helium atoms

Soutenue le 14 mars 2011 devant le jury composé de :

Pierre LEMONDE	Président
Michèle LEDUC	Directrice de Thèse
Denis BOIRON	Rapporteur
Jook WALRAVEN	Rapporteur
Claude COHEN-TANNOUDJI	Examineur
Ennio ARIMONDO	Examineur

Contents

0.1	About metastable Helium	7
0.1.1	Noble gases in the cold atom field	7
0.1.2	Specificities of Helium	8
0.2	Metastable Helium in optical potentials	10
0.3	Outline of this thesis	11
1	New experimental setup for the trapping of He*	13
1.1	The experimental apparatus	13
1.1.1	Vacuum system	13
1.1.2	Optical setup	14
1.1.3	Computer control system	16
1.1.4	Channel Electron Multiplier	17
1.2	Production of a slow beam of metastable Helium atoms	19
1.2.1	Production of an atomic beam of metastable atoms	19
1.2.2	Determination of the atomic longitudinal velocity distribution before slowing	21
1.2.3	Zeeman slower	22
1.3	Magneto-optical trap	26
1.3.1	Performances	26
1.3.2	Collisional regime in the MOT	27
1.3.3	Channeltron diagnosis	30
1.4	Conclusion	33
2	Novel magnetic trap for Bose Einstein Condensation	35
2.1	Cloverleaf magnetic trap	36
2.1.1	Ioffe-Pritchard potential	36
2.1.2	Trap design	37
2.2	Electric circuit	40
2.2.1	Quadrupolar field for the MOT	40
2.2.2	Ioffe-Pritchard trap	40
2.2.3	Switch between the two configurations	42
2.2.4	Control of the bias field	43
2.3	Loading of the magnetic trap	46
2.3.1	Optical molasse	46
2.3.2	Optical pumping	47
2.3.3	1D Doppler cooling	48
2.3.4	Characteristics of the atomic sample in the compressed trap	50

2.4	Towards evaporative cooling	52
2.4.1	RF spectroscopy	52
2.4.2	Evaporative cooling principle	53
2.4.3	Thermalisation rate	54
2.4.4	RF ramp for forced evaporative cooling	55
2.5	Conclusion	57
3	Prospects for experiments in an optical dipole trap	59
3.1	Optical trapping potential	60
3.1.1	Trapping potential	60
3.1.2	Scattering losses	62
3.1.3	Red-detuned crossed dipole trap	62
3.2	Variations of the Penning collision rates with the magnetic field value in a dipole trap	66
3.2.1	Different evaluations for the interaction potential in $^5\Sigma_g^+$	66
3.2.2	Spin-dipole Hamiltonian	68
3.2.3	Inelastic collision rates	69
3.2.4	Discussion of the theoretical evaluation	71
3.2.5	Experimental measurement of the inelastic rates	73
3.3	Conclusion	76
4	Metastable Helium in optical lattices	77
4.1	1D optical lattices: collisional properties in confined dimensions	78
4.1.1	The confining potential, a 1D optical lattice	78
4.1.2	Elastic scattering in axially confined geometries	80
4.1.3	Inelastic scattering in a quasi-2D regime	83
4.1.4	Experimental observation of the quasi-2D collisional regime	84
4.2	3D optical lattice: Mott Insulator - Superfluid phase transition	87
4.2.1	3D optical lattice properties	87
4.2.2	The Superfluid to Mott-insulator transition for Helium	88
4.2.3	Dissipative Bose-Hubbard model	90
4.2.3.1	Effective losses on a single site	90
4.2.3.2	Effective losses over the lattice	91
4.3	Conclusion	96
5	Spectroscopy of a forbidden line of ^4He	97
5.1	Experimental setup	98
5.1.1	Main features of the experimental setup at the VU-Amsterdam	98
5.1.2	Optical dipole trap	99
5.2	Spectroscopy measurement	102
5.2.1	Frequency metrology studies on Helium	102
5.2.2	Measurement and lock of the laser frequency	104
5.2.3	Spectroscopy of the forbidden transition	106
5.2.4	Resonance observed on the ion signal	109
5.3	Evaluation of the experimental frequency shifts	111
5.3.1	Mean field shift	111
5.3.2	Zeeman shift	112

5.3.3	AC Stark shift	113
5.3.4	Conclusion on systematic experimental shifts	114
5.4	Intrinsic transition frequency and measurement accuracy	116
5.4.1	Derivation of the field-free transition frequency	116
5.4.2	Experimental broadening and measurement accuracy	117
5.5	Conclusion and perspectives	119
6	Conclusion	121
A	Optical imaging	125
A.1	Absorption imaging	125
A.1.1	Experimental setup	125
A.1.2	Absorption from the atomic cloud	126
A.1.3	Determination of the atom number	127
A.2	Polarisation	129
A.2.1	Degenerated system	129
A.2.2	Imaging	129
A.3	Linear absorption regime	131
A.3.1	Long duration imaging	131
A.3.2	Retroreflection of the imaging beam	131
A.3.3	Imaging to probe the stray magnetic fields	132
A.3.4	Determination of the temperature	134
B	Frequency comb	137
B.1	Mode locked lasers	137
B.1.1	Compensation of the group velocity dispersion	137
B.1.2	Spectrum of a mode-locked laser	138
B.2	Frequency combs	141
B.2.1	Absolute frequency measurement	141
B.2.2	Accuracy of an optical frequency measurement based on a frequency comb	142
B.3	Determination of an absolute optical frequency using two combs	144

Introduction

Research on ultra-cold atoms is a very rich area of investigation, where different fields of basic research merge, such as atomic, condensed-matter and many-body physics. The first realisation of a Bose-Einstein condensate (BEC) has been observed almost simultaneously in 1995 by three groups working with different alkali atoms (Rb [1], Na [2], Li [3]). Before, BECs have usually been associated with superfluid helium, as it was firstly pointed out by London [4]. The exact link between superfluidity and Bose-Einstein condensation still remains difficult to be understood. However, degenerate dilute gases are much closer to Einstein's original idea of a condensate [5] since atoms are only weakly interacting and thus closer to an ideal gas than superfluid helium is. The first generation of experiments on those quantum objects revealed that their behaviour is described by a macroscopic wave-function [6] governed by a nonlinear Schrödinger equation [7, 8]. Most properties of weakly-interacting Bose-Einstein condensates in three dimensions were investigated in many details. Coherence properties and quantised vortices providing a striking evidence for the superfluidity of Bose-Einstein condensates are well described in a mean-field framework [9, 10, 11, 12]. At the same time, the first degenerate Fermi gases were experimentally realised [13, 14, 15].

Within the last thirty years, research efforts in this field are undergoing a continuous expansion. The precise control of atomic interactions, taking advantage of Feshbach resonances [16, 17] in an external magnetic field, opened the way towards regimes of strong correlations described by complex many-body theories [18]. Such correlation characteristics can also be achieved in optical lattices produced by far-detuned standing waves of laser light. Thanks to the good control on the trapping potentials and the detailed description of atomic interactions, the system is fully described by a model Hamiltonian. Reference Hamiltonians were proposed and extensively studied in the field of condensed matter, for which numerical simulation is impossible. As a consequence ultracold gases constitute a unique tool to investigate open problems from condensed matter, via analogous simulation as initially proposed by Feynman [19].

0.1 About metastable Helium

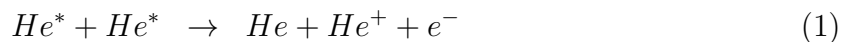
0.1.1 Noble gases in the cold atom field

Noble gases constitute challenging candidates for Bose-Einstein condensation since optical manipulation of their ground state would require light sources in the far UV. But they show long-lived metastable states (7900 s for Helium), which can be considered as effective ground states on the experimental times scales. From those levels atomic transitions can

be induced using state-of-the-art lasers.

Their main specificity is based on their large internal energy of the order of several eV. This energy can be released when hitting any metallic or dielectric surface, emitting one electron by Auger effect. This property allows for a very efficient detection of metastable atoms using electron multipliers (channeltrons or microchannel plates) leading to a single atom sensitivity on a time scale of few nanoseconds. This opens the possibility of new experimental studies, some of which are difficult to realise with alkaline atoms, as for instance the effect of finite particle number working with small condensates. This possibility has also been used for the direct measurement of correlation functions in the groups of W. Vassen and A. Aspect, enlightening the atomic Hanbury-Brown and Twiss effect [20].

This large internal energy also makes metastable atoms intrinsically fragile and difficult to manipulate. Any atomic collision may lead to losses due to the ionisation of one of the colliding particles. Two metastable Helium atoms have a very large probability to undergo Penning ionisation, described by the following equation:



The collision rate of this reaction is of the order of $10^{-10} \text{ cm}^3 \cdot \text{s}^{-1}$ [21], which prevents to achieve the large atomic densities characterising a degenerate gas. However, for Helium, if the colliding partners are spin polarised, the Penning ionisation is inhibited as the electronic spin is not conserved between the initial and final states. A collision rate of $10^{-14} \text{ cm}^3 \cdot \text{s}^{-1}$ has been calculated and experimentally verified [22, 23, 24].

Since the early experiments on slowing down beams of metastable Helium, four groups achieved Bose-Einstein condensation of the isotope $^4\text{He}^*$: Orsay [25], Paris [26], Amsterdam [27], Canberra [28] and recently in the group of W. Ketterle [29]. So far, Xenon, Krypton and Neon atoms in P metastable states have been loaded into magneto-optical traps and cooled down to the mK range. Neon metastable atoms have been loaded into magnetic traps and brought to lower temperatures but the condensation has not been achieved yet (Eindhoven [30], Darmstadt [31], Queensland [32]).

0.1.2 Specificities of Helium

The Helium atom offers another specific advantage : being the simplest atom next to Hydrogen, its atomic structure can be calculated ab initio with great accuracy [33]. On the contrary to alkali atoms, the nuclear spin of ^4He is zero and thus the atomic structure does not show an hyperfine structure as can be seen in figure 1.

In this thesis we report on the first spectroscopy measurement of the triplet-singlet magnetic dipole transition $2^3S_1 \rightarrow 2^1S_0$ realised during my staying in the group of Wim Vassen at the Vrije Universiteit (VU) in Amsterdam. The present experimental error of 10 kHz on the frequency of the atomic transition is substantially smaller than estimates of non-evaluated higher order terms in QED calculations (presently evaluated at 3 MHz [33]) and presents a significant challenge for groups involved in atomic structure

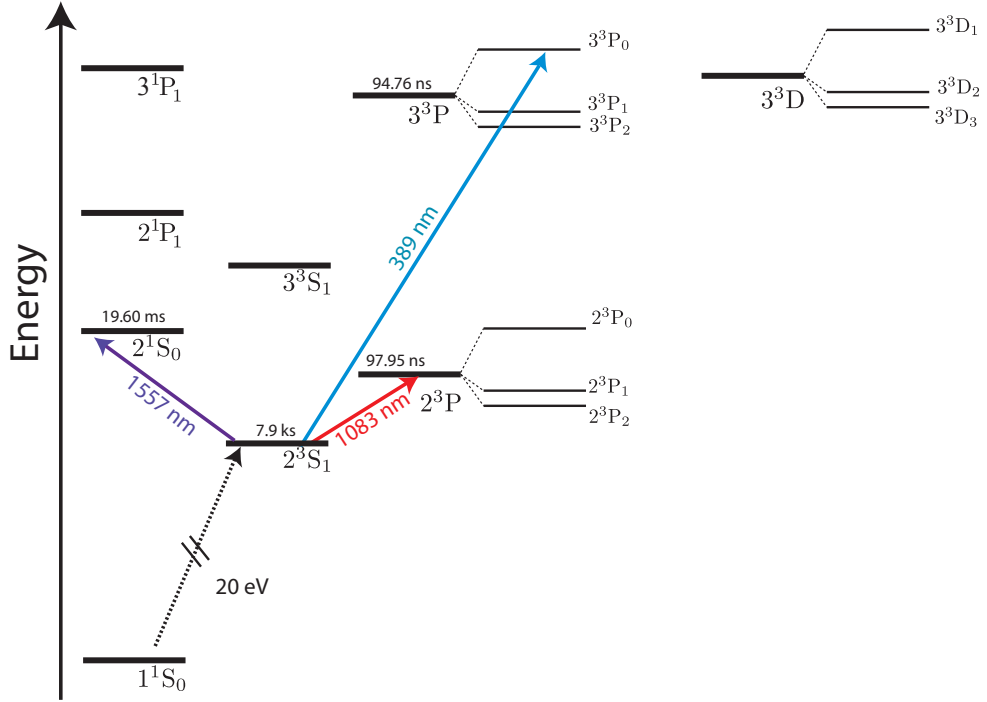


Figure 1: Energy levels of ^4He (not to scale). We work with the triplet 2^3S_1 metastable state as an effective ground state. For cooling and trapping the $2^3S_1 \rightarrow 2^3P_2$ transition at 1083 nm is used. In [34], the $2^3S_1 \rightarrow 3^3P_0$ transition at 389 nm has been used to magneto-optically trap $^4\text{He}^*$. In this manuscript we report on a spectroscopy measurement of the magnetic dipole transition $2^3S_1 \rightarrow 2^1S_0$, first direct link between the singlet and triplet families of Helium.

theory. The very narrow natural linewidth of this transition (8 Hz) allows for possible improvements in spectroscopy measurements and especially concerning the isotope shift of Helium. This atomic transition at 1557 nm has indeed been measured in the group of Wim Vassen for the fermionic isotope ^3He , providing a new and accurate determination of the isotope shift and thus the charge radius. The result is competitive with the present best measurement on the $2^3S_1 \rightarrow 2^3P$ of Helium [35] reaching an accuracy of 5 kHz.

Also molecular potentials between interacting helium atoms can be calculated ab initio [36]. This enables accurate determination for the s – $wave$ scattering length, the parameter describing fully the cold two-body collisions. Previously the ENS group realised two successive measurements of this parameter, using one- and two-photon photoassociation [37, 38]. The basic idea is to deduce the energy of the least bound-state $v=14$ in the $^5\Sigma_g^+$ molecular potential. The latest experiment leads to a very accurate value $a = 7.512 \pm 0.005$ nm, from which a 1 μs lifetime of the molecule can be extracted [39]. This value is in disagreement with the theoretically evaluated lifetime lying in the range of 100 μs [40], which assumes that the lifetime of this exotic dimer is limited by Penning collisions. The new channeltron implemented in the ENS setup, as described in this thesis, could solve this discrepancy. The ability to detect ions, allows to distinguish the losses due to Penning ionisation from other possible decay channels, not considered by theory.

0.2 Metastable Helium in optical potentials

This thesis work follows those photoassociation experiments and presents the construction of a new experimental setup, conceived to allow the implementation of optical potentials for metastable Helium.

The dipole force originating from far-detuned laser beams allows to create versatile optical potentials for neutral atoms. The rapid development of those trapping potentials relies on several advantages over the magnetic ones opening new experimental opportunities. Several directions have been investigated for the future experiments, which could be realised in our group:

- the study of the magnetic field dependency of inelastic collisions in a crossed dipole trap,
- the effect on the Penning collision rates of geometry of reduced dimensionality,
- the specificities of $^4\text{He}^*$ in a 3D optical lattice.

In optical traps, atoms are confined regardless from their spin state, opening the exploration of samples of spin states or mixtures which cannot be controlled in a magnetic trap. The group of Institut d'Optique implemented a dipole trap for metastable Helium and could measure spin-state-resolved Penning ionisation rates [41]. Another profitable aspect of those traps is the release of the constraint on the magnetic field, which hence becomes a free parameter. In this work we present a theoretical study of the magnetic field dependency of the Penning collision rate as first studied in [22, 23], which should be measurable with the new experimental setup implemented.

Another possible application for optical lattices is the confinement of the atomic sample in a geometry of reduced dimensionality, which has been first considered by Bagnato and Keppeler [42]. It is well established that confinement of a gas can strongly modify both the elastic and inelastic collision rates as established in 1D [43, 44] and 2D [45, 46]. The first experimental realisation of traps in which the level spacing approaches the thermal energy, freezing the movement in a plane or a tube, is reported in [47]. In order to experience low-dimensional collisions, the extension of the wave function has to be smaller than the typical range of the interaction potential, which was experimentally achieved in 1D [48] and 2D [49]. Many experimental studies cover the new phenomena resulting from the strong confinement of a quantum gas [50, 51, 52].

Confining He^* atoms in a 1D optical lattice at $\Lambda = 1560$ nm makes it possible to study the modification of the Penning inelastic collision rate induced by a tight axial confinement.

Optical potentials are also easier to be shaped spatially and open the possibility to study strongly correlated states. Optical lattices, resulting from the interference pattern of counter-propagating laser beams, simulate a perfect model crystal in which all the geometry parameters are controlled by the experimentalist. The gas is then described by a Hubbard Hamiltonian, a fundamental model introduced in solid state physics in order

to describe the transition between conducting and insulating systems. As pointed out by Jaksch *et al.* [53], such optical potentials allow to convert a weakly interacting Bose gas (superfluid) into a strongly interacting quantum state (Mott insulator). This predicted quantum-phase transition has been observed by Greiner *et al.* [54] : the destruction of the long-range phase coherence of the superfluid state has been observed entering the Mott insulator state.

Here on-site interaction are large enough to prevent the tunneling and induce strong many-body interaction.

0.3 Outline of this thesis

This thesis work was carried out in the cold atom group at Laboratoire Kastler Brossel under the supervision of Michèle Leduc.

The first two chapters of this manuscript describe the construction of a new experimental setup for the condensation of metastable Helium. Chapter 1 is dedicated to the improvements realised on the existing setup : a new computer-program has been implemented, all the optics redesigned and fiber-coupled to achieve more stability. The glass cell in which experiments are carried out has been replaced in order to gain more optical access. Also a Channel Electron Multiplier (channeltron) has been added in the science chamber providing new diagnostics, which are essential for the future experiments. As detailed in this work, it allows us to characterise more precisely the atomic beam of metastable Helium and its slowing process occurring in the Zeeman coils. The magneto-optical trap (MOT), loaded from this slow beam, contains up to $2 \cdot 10^8$ atoms at a temperature of 1 mK. Diagnostics provided by optical imaging and by the channeltron will be discussed.

In Chapter 2, the implementation of a novel cloverleaf magnetic trap is detailed. This trap has been specifically designed to produce the condensate and efficiently load it in-situ into an optical potential, either a dipole trap or optical lattices. Details about the electric circuit and its performances are reported. Typically 10^8 atoms are loaded in this new magnetic trap and a phase-space density of $\chi \approx 7 \cdot 10^{-6}$ could be reached.

Chapter 3 presents the theoretical background of the different experiments involving optical potentials. After a brief overview of the general principle and properties of optical trapping, we specify the parameters of the crossed dipole trap at $\Lambda = 1560$ nm, which will be soon implemented in our setup. The tests done so far on optical modulators and laser beam spatial profiles are reported. In this dipole trap, we plan to verify the variations of the Penning ionisation loss rates with the magnetic field value, which was first predicted in [22, 23]. A new numerical evaluation, using the latest available molecular potentials for metastable Helium [36], has been realised.

Concerning optical lattices, two thematics are developped in Chapter 4. First a prospective study on the effect of confinement in a 1D optical lattice on the inelastic Penning collision rates is detailed, demonstrating our ability to effectively enter the quasi-2D collisional regime and to measure a modification of the inelastic collision rates induced by

the strong confinement.

The description of metastable Helium in a three-dimensional optical lattice requires an extension of the Bose-Hubbard model, in order to include the dissipation resulting from Penning losses. Such open quantum systems are similar to systems studied in quantum optics, which are driven by an external field and coupled to the environment inducing a non-equilibrium dynamics. Diehl *et al.* suggested to take advantage of this novel possibility to drive an atomic system into a many-body quantum state [55]. For metastable Helium, Penning ionisation opens the way towards strongly correlated system, similarly to a recent experiment realised in one dimension [56]. Large two-body losses thus result in a stabilisation of the system, suppressing double occupancy of lattice sites and as a consequence the losses events.

The last chapter constitutes a separate part of this work and represents the results of four months of experimental work in the group of Wim Vassen at the Vrije Universiteit (VU) in Amsterdam. We report on a spectroscopy experiment on the magnetic dipole transition $2^3S_1 \rightarrow 2^1S_0$ in ^4He , first direct link between the ortho- and para-helium family. This first direct measurement of the transition combines the advantages of the cold atoms field, having a condensate of $^4\text{He}^*$ atoms confined in a dipole trap, with state-of-the-art frequency combs technology. The experimental techniques developed during my stay are described in this chapter. The different experimental shifts and broadening are evaluated in detail, in order to determine the absolute atomic transition energy and the achieved experimental accuracy.

Chapter 1

New experimental setup for the trapping of He*

The experimental apparatus, aiming to produce Bose Einstein condensates of Helium atoms in the 2^3S_1 metastable state, has been almost completely rebuilt. The main changes and improvements accomplished since september 2007 will be detailed in this chapter. The goals were twofolds: on one hand an improvement of the stability and performances of the experiment and on the other hand the development of a more versatile trapping scheme in order to diversify the experimental possibilities. A new detection device (Channel Electron Multiplier or channeltron) has also been mounted in the science chamber to detect either metastable atoms or charged particles produced by Penning ionisation processes.

The first section will briefly present the basic layout on which the whole experiment relies, which means vacuum, optical, computer systems and the different detectors.

The metastable Helium beam produced by supersonic expansion and its subsequent slowing in the Zeeman decelerator are then analysed with the new insights offered by the channeltron recently mounted in the science chamber.

The performances of the Magneto-Optical Trap (MOT) loaded from this slow atomic beam are discussed in details in the last section. A larger quartz cell has been installed, offering more optical access and thus a better geometrical arrangement of the MOT beams. We obtain at this stage an atomic cloud of $2 \cdot 10^8$ atoms at a temperature of 2 mK.

1.1 The experimental apparatus

The general idea of our experiment is that of a 3 stages process which is sketched in figure 1.1. Helium atoms in the 2^3S_1 metastable state are first produced and selected in the source chamber before being slowed down to few tens of $\text{m}\cdot\text{s}^{-1}$ during the Zeeman slowing stage. Finally several 10^8 atoms are trapped in a MOT, described in section 1.3.

1.1.1 Vacuum system

The pumping scheme, depicted in figure 1.1, has been modified to use turbomolecular pumps instead of ion pumps or diffusion pumps. The three sections of the experiment are

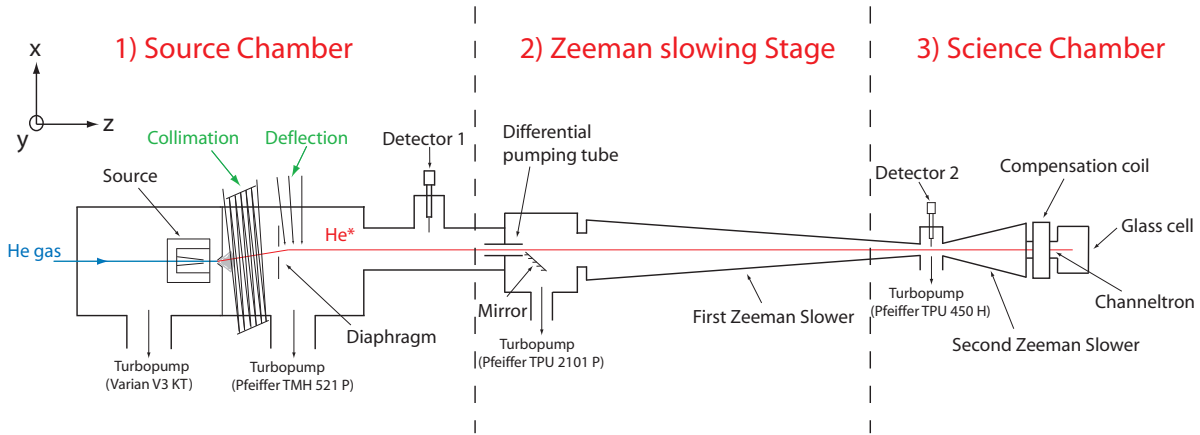


Figure 1.1: Overview of the experimental setup. The metastable atomic beam is successively collimated and deflected in the source chamber, decelerated in the Zeeman slower and trapped in the science chamber.

separated by gate valves with pneumatic actuators, all connected to a safety system. The source chamber has its own primary membrane pump, but the two last sections share the same primary vacuum system.

The source chamber consists of two distinct chambers, called *production chamber* and *selection chamber*, communicating only through a skimmer of 1 mm diameter. This hole realises the first differential pumping stage of the experimental setup. As we will see in the next section, the discharge source produces a high atomic flux containing only a small fraction of atoms in the metastable state. A turbo pump of high pumping speed (Varian V-3KT) maintains a pressure of $2 \cdot 10^{-5}$ mbar when the source operates under optimal conditions. In the selection chamber, where an atomic beam is shaped and propagated, a lower pressure is required. The differential pumping stage and a second turbo pump (Pfeiffer TMH 521 P) allow to reach $5 \cdot 10^{-7}$ mbar.

The second differential pumping stage is located in front of the Zeeman slower using a long cylindrical tube ($\varnothing=1$ cm, $L=10$ cm). A pressure of 10^{-10} mbar is maintained in the Zeeman slower using an additional turbo pump (Pfeiffer TPU 2101 P).

The science chamber, a quartz cell connected to the Zeeman slower via a CF40 flange, is pumped using a last turbo pump (Pfeiffer TPU 450 H) through the second part of the Zeeman slower ($\varnothing=2$ cm, $L=15$ cm) in order to reach 10^{-11} mbar, level required to get lifetimes of several seconds for cold atomic samples.

1.1.2 Optical setup

As already detailed in the PhD thesis of Julien Dugué [57], the optical setup was entirely designed using fiber-coupling offering a much larger stability and improving the optical quality of the beams.

The light source for the laser system is a Diffracted Bragg Reflector (DBR) laser diode emitting at 1083 nm and placed in an external cavity to reduce its linewidth to 300 kHz. This seed is frequency-locked on the $2^3S_1 \rightarrow 2^3P_2$ transition using saturated

spectroscopy. This transition has a linewidth $\Gamma_0 = 1.62$ MHz and a saturation intensity $I_{sat} = 167 \mu\text{W}\cdot\text{cm}^{-2}$.

Two fiber amplifiers (Keopsys), providing respectively 3 W and 1 W, are placed in series to produce enough power for the different stages of the experiment. As depicted in figure 1.2, near resonant laser beams are needed in six phases of a typical experimental sequence: the collimation and deflection of the atomic beam, the Zeeman slowing, the trapping and cooling in the MOT, the detection using absorption images and finally the optical pumping to a magnetically trapped state, which will be discussed in chapter 2. The frequencies needed are derived using acousto-optical modulators (AOM) mounted in double pass configuration in order to have a stable fiber injection at different detunings. Table 1.1 summarizes the power needed for each of those optical beams and their detuning from the atomic resonance.

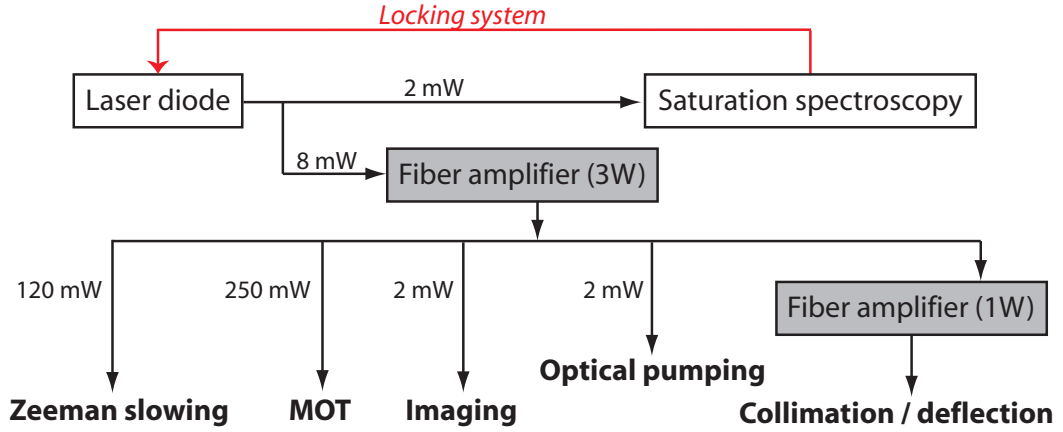


Figure 1.2: *Layout of the laser system. The laser diode, placed in an external cavity, is locked using saturation spectroscopy and retroacting both on its current and the piezo-electric control of the position of the cavity mirror. This seed injects a 3 W amplifier producing all the laser beams required at different stages of the experiment. A 1 W amplifier is dedicated to the optical beams, which collimates and deflects the atomic beam in the selection chamber.*

Optical beam	Power ($\text{mW}\cdot\text{cm}^{-2}$)	Beam diameter (cm)	Detuning (MHz)
Collimation	2×175	1.5	-1.6
Deflection	250	8×2 (elliptical)	-1.6
Slowing	60	2	-240
MOT (each beam)	8.5	2	-45
Imaging	0.02	1	0

Table 1.1: *Typical power and detuning used for the different optical beams. Those values will be discussed in more details in the text.*

1.1.3 Computer control system

Bose-Einstein condensation experiments go through a complicated sequence each time a degenerate gas is produced and require therefore a robust computer control. A new LabView programm has been implemented to operate such sequences and analyse the obtained data. The general layout presented in figure 1.3 involves:

- a digital card (DIO 64) providing 64 digital outputs and generating a 20 MHz clock signal,
- three National Instrument cards (PCI 6722, 6731, 6733) offering 20 analog outputs each.

Those three cards are synchronized and triggered by the digital card which enables to benefit of the onboard 20 MHz clock time stability.

To protect the computer from over-voltage or short-circuit from the experiment, the physical outputs are opto-isolated from the computer bus, each having its own floating ground. The cutoff frequency for the digital outputs is set by the optocouplers around 200 kHz. Therefore the minimal time step duration is limited to $5 \mu\text{s}$, which is short regarding all the experimental time scales.

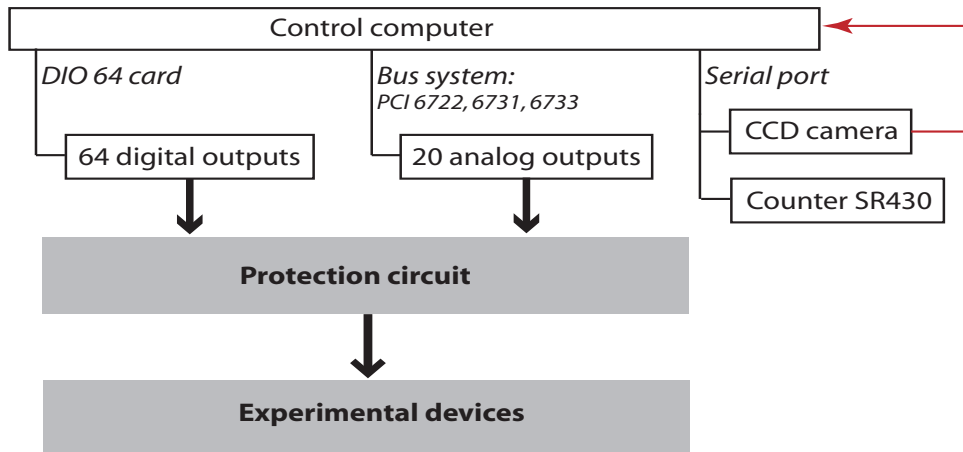


Figure 1.3: Structure of the control system. The computer operates the different devices (shutter, AOMs, power supplies, ...) using a digital/analog outputs system. Data from the CCD camera can be retrieved and analysed at the end of each experimental sequence.

This programm enables the realisation of any experimental sequences involving GPIB or RS-232 communications to set device parameters and retrieve data. The time frame of each sequence can be stored and recalled from the disk. Experimental scans of one or several parameters can be automatically executed. Finally, at the end of each sequence, the pictures taken by the Hamamatsu CCD camera are stored and analysed as well as the data produced by the channeltron's counter (SR430 Stanford Research System).

1.1.4 Channel Electron Multiplier

Channel Electron Multipliers (Channeltron) are vacuum-tube structures meant to detect single incident particles. A channeltron has been mounted in our science cell in order to detect either metastable Helium atoms hitting the front surface of the detector and releasing their high internal energy, or charged particles produced during Penning collisions and attracted by the front voltage. This work will illustrate the new diagnosis offered by this detector for the cooling and trapping of metastable Helium atoms.

General principle: Assuming an incident energy higher than a few eV, one particle impinging into the channeltron lead glass surface induces secondary electron emission. Those electrons are then accelerated down the channel by a positive bias and create an avalanche of electrons: each collision with the internal wall of the channel is creating 2 to 3 electrons for one.

With a bias voltage of 3 kV between the input and the output of the channel, called respectively *front* and *back* (see figure 1.4), approximately 10^8 electrons are created and collected by a metal anode, all having been triggered by just one particle. The curvature of the channel is necessary to prevent ion feedback caused by the high electron density at the end of the channel, which could repel them.

A resistor of $10\text{ M}\Omega$ has been implemented to maintain a potential difference of 100 V between the collection electrode and the back. This voltage accelerates the electron cloud out of the channeltron towards the anode, resulting in an easily detectable pulse of 80ns duration at Full Width Half Maximum (FWHM). The corresponding current is 2 mA, which means 100 mV peak voltage on a $50\ \Omega$ resistor. Those output pulses can be easily detected using a counter (SRS-430 in our experiment).

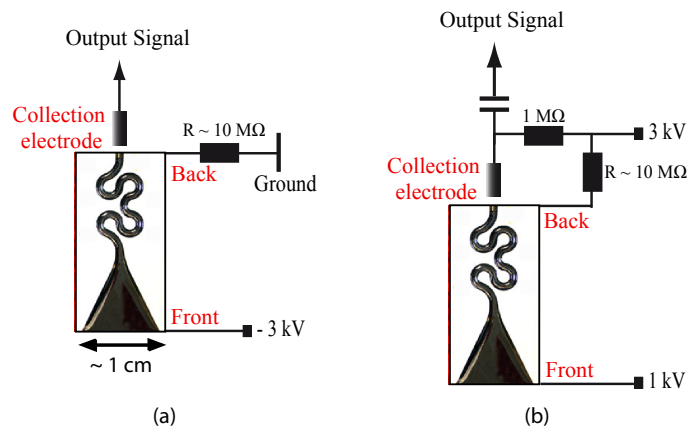


Figure 1.4: *Schematics of the electrical connections for the channeltron: a) to detect positively charged particles, b) to detect negative particles.*

Metastable atoms can be either directly when they hit the channeltron or indirectly from the ions produced by Penning ionisation events.

Detection of metastable Helium atoms: Metastable atoms are detected as soon as they hit the channeltron. The atomic signal can not be filtered out by means of electrical fields. But its contribution is temporally decoupled in the experimental sequence since it only occurs during the loading process, when the atomic beam is on (this will be detailed in section 1.2) or after releasing the atoms from the trap producing a time-of-flight signal analysed in section 1.3.

As will be detailed in this chapter, this signal provides a full characterisation of the velocity distribution of the atomic beam at different stages of the slowing process. The analysis of the time-of-flight signal, obtained after releasing the atoms from the trapping potential, give acces to the cloud temperature. However, the total atom number is difficult to calibrate since the detector is saturated even for the smallest gain.

Detection of charged particles: By choosing the sign of the voltage applied to the front of the channeltron, one can attract and thus detect either positive ions or electrons produced in the trapped cloud. In figure 1.4 the electronic circuits which are used to detect positive or negative charged particle are detailed.

We choose to detect preferably ions because of their smaller velocity, hence being less affected by the magnetic fields present in the science chamber. An important time scale is the delay between the production and the detection of one ion. In the experimental setup, the channeltron is resting at the bottom of a quartz tube centered on the cell, 5cm away from the trapped atomic cloud. Its front voltage of -3 kV produces an electrical field in the cell, whose glass walls are assumed to be at ground potential. One ion resulting from a Penning ionization collision has an initial kinetic energy of $E_{k,0} = E_m - E_i$ where $E_m = 19.8$ eV is the internal energy of the metastable atom and $E_i = 4.8$ eV the ionization energy for Helium from the 2^3S_1 level. Solving Newton's second law for one ion with an initial velocity pointing in the direction opposite to the channeltron (worse case), the delay is evaluated to be of the order of $2 \mu s$. The exact value of this delay is not important, since it is negligible regarding the dynamics time scales in the trapped cloud. The essential quality of this new detection device is its ability to detect single ion and thus to obtain a precise evaluation of the Penning losses in the trapped cloud.

1.2 Production of a slow beam of metastable Helium atoms

This section presents a complete characterisation of the atomic beam: flux, transverse profil, longitudinal or transverse velocity distributions. All the measurements are realised using three detectors positioned along the beam path. As already mentioned, the high internal energy of Helium atoms in the metastable state can be released when hitting a metallic surface, producing one electron. The *first detector* and *second detector* are Faraday cups mounted on vertical translation stages one 1.2 m behind the source chamber and the second in front of the cell (4 m behind the source). The current measured on those devices is proportional to the atom number per second.

The *third detector* is the channeltron described more extensively in section 1.1.4.

1.2.1 Production of an atomic beam of metastable atoms

Helium atoms are excited in the 2^3S_1 metastable state in a discharge source described in [58]. Helium gas is continuously injected into a cylindrical gas reservoir where an intense discharge is produced by applying a voltage of 1 kV onto the cathode while the anode is kept at ground potential. After undergoing electronic collisions, a small fraction (between 10^{-4} and 10^{-6}) of the ground state atoms is excited to higher energetic states before decaying into the long lived 2^3S_1 metastable state. The source is cooled with liquid nitrogen to avoid heating of the reservoir due to the discharge.

The extraction hole of the discharge cavity gives an optimal raw flux for a diameter of 0.4 mm. With a pressure of $2 \cdot 10^{-5}$ mbar and a discharge current of 5 mA, 1 nA are collected on the first detector ($\varnothing=7$ mm), corresponding to an atomic flux of $1.2 \cdot 10^9 \text{s}^{-1}$. Increasing the gas pressure or the discharge current could improve this value, but the efficiency of the deceleration of the atomic beam would be reduced as studied in [58].

Collimation: At this stage the atomic beam undergoes a supersonic expansion through the skimmer into the selection chamber converting thermal energy into kinetic energy. The resulting mean longitudinal velocity is of the order of $1000 \text{ m}\cdot\text{s}^{-1}$ and transverse velocities $v_{lat,i}$ of the order of $60 \text{ m}\cdot\text{s}^{-1}$ leading to a fast divergence of the beam. The propagation of the atomic beam over 4 m in a 2 cm diameter tube sets a higher limit on the transverse velocity of $v_{max} = 2.5 \text{ m}\cdot\text{s}^{-1}$.

To reduce the transverse velocities and thus increase the atomic flux along the beam axis, a collimation is realised with light slightly red-detuned from the transition $2^3S_1 \rightarrow 2^3P_2$ and therefore only affecting atoms in the metastable state. Several reflexions of the laser beam are required to increase the interaction time between the fast atoms and the light. The cooling occurs on a length of approximately 10 cm, corresponding to a cooling duration of approximately $100 \mu\text{s}$. The large intensity of the laser beam (in the range of $600 I_{sat}$) increases the capture range of this process.

Deflection: Another drawback of the atomic beam produced is to contain not only Helium atoms in the metastable state but a mixture of different energy states. The selection of the proper internal state is done by using radiation pressure forces to deflect the wanted metastable atoms. Indeed if a plane wave illuminates at right angles the atomic beam, red-detuned from the atomic transition, the radiation pressure force, directed along the laser wave vector \mathbf{k} , will deflect the metastable atoms from their initial direction. Since this deflection is accompanied by a changing Doppler shift (equal to $\vec{k} \cdot \vec{v}$) which brings the atoms out of resonance, the deflection process quickly becomes inefficient. To avoid this, a converging laser beam is used to change gradually the direction of the wave vector \vec{k} in order to keep $\vec{k} \cdot \vec{v}$ constant as the atom is deflected. The differential pumping tube ($\varnothing=1$ cm, $L=10$ cm) located at the beginning of the Zeeman slowing stage is the diaphragm used to discriminate the non collimated and non deflected Helium atoms.

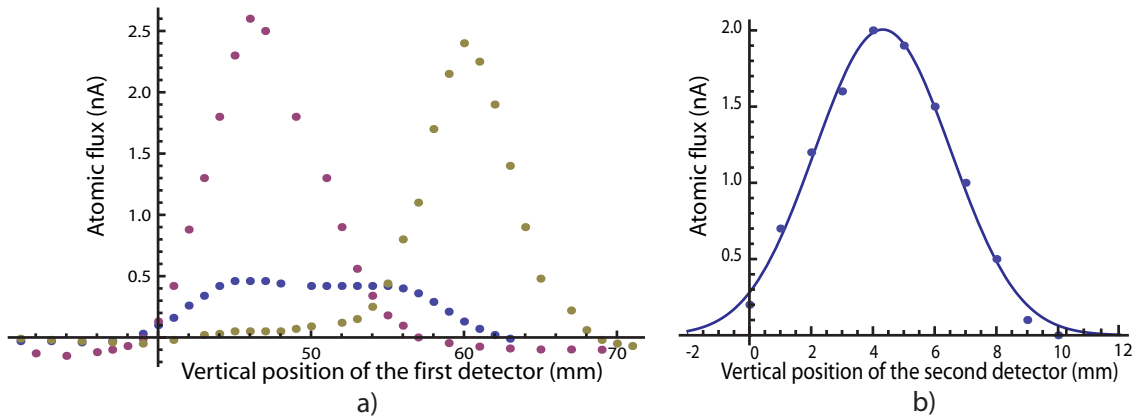


Figure 1.5: *Characterisation of the collimation and deflection efficiency. a) Atomic beam profile 1.2 m behind the source: the raw flux is in blue, the collimated beam in lila, the collimated and deflected beam in green. b) Atomic beam profile 4 m behind the source, with collimation and deflection.*

Experimental efficiency: The vertical profiles of the atomic beam (figure 1.5 a)) are obtained by scanning the raw flux, the collimated beam and then the deflected beam with the first detector. The broadening caused by the 7 mm size of the detector has been deconvoluted.

After collimation, the width of the beam 1.2 m behind is reduced to 5.5 ± 0.5 mm diameter (FWHM), corresponding to an atomic transverse velocity smaller than $5 \text{ m} \cdot \text{s}^{-1}$.

The atomic beam is then deflected with 70% of efficiency (comparison of the areas) and its diameter reduces to 3.5 ± 0.5 mm (FWHM): all the atoms deflected will pass through the diaphragm tube of diameter 1 cm.

Using the second Faraday cup standing very close from the cell the beam diameter is measured to be 4 ± 1 mm (FWHM) after almost 4 m of propagation (see figure 1.5 b)), confirming a negligible atomic transverse velocity after this collimation/deflection stage.

1.2.2 Determination of the atomic longitudinal velocity distribution before slowing

The longitudinal velocity distribution of the atomic beam before slowing can be deduced from the study of the free propagation of one atomic packet. The collimation and deflection laser beams are pulsed such that atomic bunches travel along the Zeeman slower (without deceleration) before being detected by the channeltron placed right in front of the cell. A typical signal registered by the detector is shown in figure 1.6.

The atomic velocity distribution $P_v(v)$ is assumed to be Gaussian just behind the source and thus can be written as:

$$P_v(v) = P_0 \exp\left(-\frac{(v - v_{mean})^2}{2\Delta v^2}\right) \quad (1.1)$$

where P_0 is a normalization factor, v_{mean} the mean velocity and Δv the velocity spread.

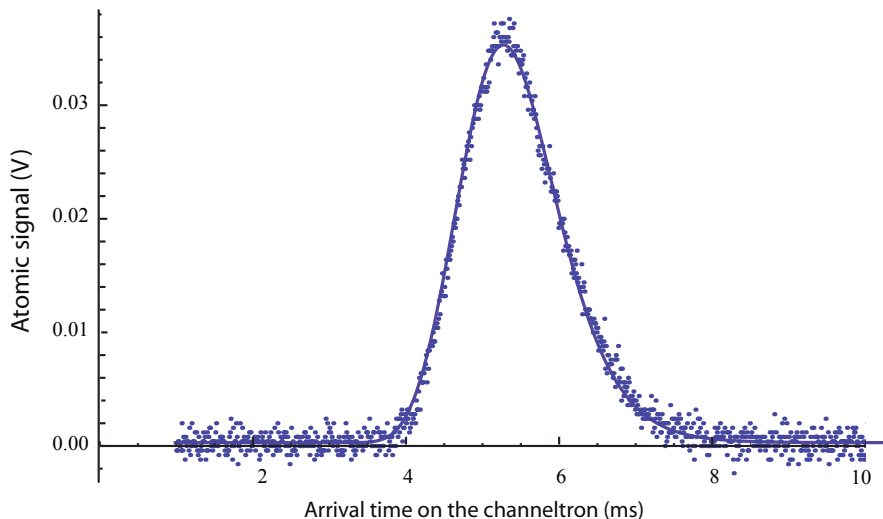


Figure 1.6: *Arrival time distribution of different velocity components of an atomic packet detected on the channeltron. $t=0$ represents the rising edge of the pulse applied on the collimation/deflection stage. The dots are the experimental data and the line is the theoretical model, corresponding to the convolution of equation 1.2 on t_0 . This allows to deduce the two parameters of the gaussian distribution for the velocity profile of the atomic beam produced by the source: $v_{mean} = 840 \text{ m}\cdot\text{s}^{-1}$ and $\Delta v = 200 \text{ m}\cdot\text{s}^{-1}$.*

After propagation over a length L_{tot} , the probability $P_t(t)dt$ to arrive at $t \pm dt$ is equal to the probability $P_v(v)dv$ to have a velocity $v \pm dv$. The arrival time t and the atomic velocity v are simply related via $t - t_0 = vL_{tot}$, where t_0 is the departure time. Hence the arrival time distribution $P_t(t)$ can be expressed as:

$$P_t(t) = P_0 \frac{L_{tot}}{(t - t_0)^2} \exp\left(-\frac{\left(\frac{L_{tot}}{t - t_0} - v_{mean}\right)^2}{2\Delta v^2}\right). \quad (1.2)$$

In order to detect a significant atomic signal, the collimation/deflection light pulse duration cannot be shorter than 0.9 ms, which cannot be neglected regarding a typical

propagation duration of typically 5 ms. As a consequence, several velocity classes can have the same arrival time because atoms start at different times $0 \leq t_0 \leq 9$ ms. The experimental data are thus fitted by the convolution of equation 1.2 on t_0 , where the only free parameters are v_{mean} and Δv . The fitting procedure gives a mean longitudinal velocity of $v_{mean} = 840 \text{ m}\cdot\text{s}^{-1}$ and a velocity spread of $\Delta v = 200 \text{ m}\cdot\text{s}^{-1}$. The good agreement between the experimental data and the fit can be seen on figure 1.6. This mean velocity corresponds to a temperature of 70 K although the source, cooled with liquid nitrogen, is expected to be warmer than its vaporisation temperature $T_{vap} = 77 \text{ K}$. This can be explained by the collimation/deflection stage, which acts as a low pass filter for the velocity distribution: fast atoms having a not sufficiently long interaction time with the light are not deflected enough and filtered before entering the Zeeman slower.

1.2.3 Zeeman slower

Numerous techniques for slowing atoms have been demonstrated to date. Those techniques differ in the way they compensate for the changing Doppler shift of the decelerated atoms. The principle of Zeeman slowing, first introduced by W. D. Philipps in [59], has been implemented in most of the cold atoms experiments. This paragraph intends to characterise the slowing process of the atomic beam using the new diagnosis offered by the channeltron, located in the science chamber. Atomic bunches, produced as described in the previous paragraph, are launched in the Zeeman coils and detected as they reach the glass cell. The slowing process is modeled and compared to the experimental data.

Basic principle: During the slowing process, atoms interact with a resonant counter-propagating laser beam. In order to maintain this matching between the laser frequency and the atomic transition frequency, the changes in the Doppler shift due to the deceleration of the atoms have to be compensated. Therefore a spatial variation of an external magnetic field $B(z)$ will be used to shift the atomic transition frequency ω_0 according to:

$$\omega_a(z) = \omega_0 + (g_P m_{J_P} - g_S m_{J_S}) \frac{\mu_B B(z)}{\hbar}. \quad (1.3)$$

where $g_P=3/2$ and $g_S=2$ are the Lande factors of the 2^3P_2 excited state and of the 2^3S_1 metastable state respectively and $m_{J_P}=2$, $m_{J_S}=1$ the respective magnetic moments of those two states.

The resonance condition linking the velocity vector of an atom $\mathbf{v}(z)$, \mathbf{k}_L and ω_L the wave-vector and frequency of the laser beam and $\omega_a(z)$:

$$\omega_a(z) = \omega_L - \mathbf{k}_L \cdot \mathbf{v}(z). \quad (1.4)$$

An atom will then keep its initial velocity v_{in} until it reaches a position z where the resonance condition expressed in equation 1.4 is fulfilled and then follows the spatial variation of the velocity imposed by the magnetic field profile.

Our Zeeman slower consists of two Zeeman coils creating a magnetic field ranging from 540 G to -140 G and a circularly polarized laser beam detuned by $\Delta = -240 \text{ MHz}$ from the resonant frequency ω_0 . This double-Zeeman configuration has been chosen

to avoid the degeneracy of the two transitions $2^3S_1, m_J = +1 \rightarrow 2^3P_2, m_J = +2$ and $2^3S_1, m_J = +1 \rightarrow 2^3P_1, m_J = 0$ occurring for a 600 G field. Although a σ^+ laser polarization should allow only transitions to the $2^3P_2, m_J = 2$ Zeeman sub-state, possible imperfections of this polarization can induce losses in the total number of slow atoms.

In addition, a non zero field at the end of the Zeeman slower suppresses almost completely the effect of the Zeeman laser beam on the MOT. Indeed its frequency, resonant with slow atoms only in a magnetic field of -140 G, is far detuned from the atomic resonance in the MOT region where the magnetic field is zero ($\approx 150 \Gamma_0$).

The spatial variation of the magnetic field of one Zeeman coil follows:

$$B[z] = B_0 \sqrt{1 - \frac{2\alpha a_{max}}{v_0^2} z}, \quad (1.5)$$

where B_0 is the magnetic field value for which an atom of initial velocity v_0 is resonant with the laser beam detuned by Δ . a_{max} is the maximum acceleration resulting from radiation pressure force F_{pr} expressed as:

$$F_{pr} = \frac{\hbar k \Gamma_0}{2} \frac{s}{s+1} \quad (1.6)$$

with $s = \frac{I}{I_{sat}}$ the saturation parameter ($s \approx 100$ in our experiment) and Γ_0 is the linewidth of the transition. Local defects in the experimental magnetic field profile and the finite laser intensity available are taken into account considering that only a fraction α of this maximal acceleration is effectively decelerating the atom. This factor α is fixed by the length of the Zeeman coil, chosen by the experimentalist.

First Zeeman slower: The first Zeeman coil, described in more details in [58], has been designed to decelerate the atoms down to $250 \text{ m}\cdot\text{s}^{-1}$ within a distance of 1.9 m. Our experimental attenuation factor α can be evaluated to be 0.7.

The magnetic field B_0 at the beginning of the coil is chosen such that atoms with a velocity $v_0 = 1100 \text{ m}\cdot\text{s}^{-1}$ are resonant with the light detuned by Δ . Considering the velocity distribution obtained in section 1.2.2, all the atoms slower than v_0 will be captured in the slowing process, which represents 95% of the velocity distribution.

The figure 1.7 shows the experimental arrival time distribution of one atomic bunch, recorded by the channeltron, with and without deceleration by the first Zeeman slower. To obtain the two first curves, the second Zeeman coil remains switched off. The shape of the decelerated pulse can be modeled quite accurately studying the deceleration of the different velocity classes produced by the source (see 1.2.2) in the first Zeeman and their free propagation in the second slower.

The theoretical model determines for each arrival time $t_{arrival}$, the range of possible initial velocities for starting time $0 \leq t_0 \leq 9 \text{ ms}$. The probability of arriving at $t_{arrival}$ is then given by the integration of the equation 1.2 over this initial velocity range and the arrival time distribution can be generated.

A final velocity of $220 \text{ m}\cdot\text{s}^{-1}$ gives the best agreement with the experimental data. The discrepancy with the expected $250 \text{ m}\cdot\text{s}^{-1}$ final velocity can be explained by a further deceleration occurring between the end of the first Zeeman and the detector, due to power broadening of the resonance. The experimental temporal width of the decelerated bunch is perfectly reproduced by the theoretical model. It is clearly reduced compared to the one of the free propagating bunch because of the velocity synchronisation during the deceleration: atoms starting with different initial velocities will have the same final velocity. The remaining width is mainly caused by the duration of the light pulse generating different starting times for the atoms.

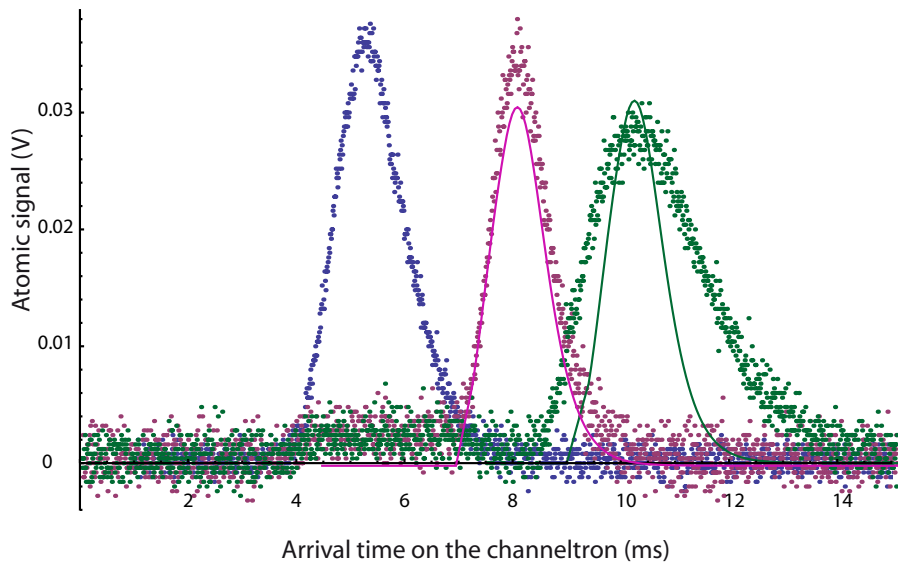


Figure 1.7: *Arrival times on the channeltron of an atomic bunch slowed by the two Zeeman slower in green, by only the first Zeeman unit in purple, non slowed in blue. The dots represents the experimental data, with a contribution of electronic noise around 0. The plain lines represent the theoretical model assuming a final velocity of $v = 220 \text{ m}\cdot\text{s}^{-1}$ in purple (first Zeeman only) and $v_f = 55 \text{ m}\cdot\text{s}^{-1}$ in green.*

Second Zeeman slower: The second Zeeman slower has been entirely rebuilt in order to reduce its transverse size. It consists now of a 20 cm water-cooled cylindrical tube on top of which 5 layers of copper wire are wound. A transverse cut exposes schematically the wiring in figure 1.8 a). The magnetic field measured for $I = 3.6 \text{ A}$ can be fitted using a theoretical model similar to equation 1.5 used for the first Zeeman, with an attenuation factor $\alpha = 0.3$ as reported in figure 1.8 b). A compensation coil minimizes the magnetic leakage from the second Zeeman field into the MOT region (1 G for 3.6 A in the second Zeeman coil).

Since all the atoms have the same velocity at the end of the first Zeeman unit, they will spend the same time being decelerated from $250 \text{ m}\cdot\text{s}^{-1}$ to v_f in the second Zeeman slower. Therefore the arrival time distribution after the second Zeeman should be the distribution

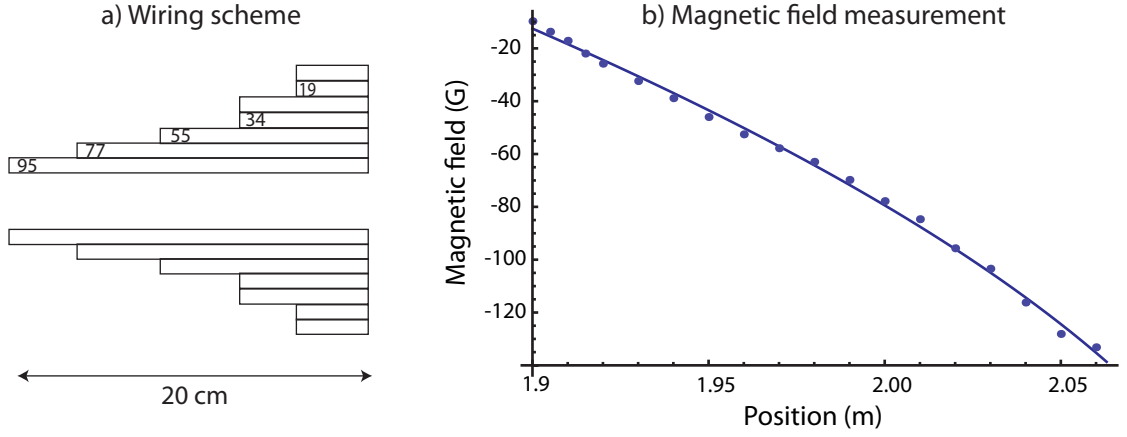


Figure 1.8: a) Wiring scheme of the second Zeeman slower, each layer of copper wire being represented by a rectangle of length proportional to the number of turns. The coil shows different number of turns per layer: 95 turns for the 1st layer, 77 turns for the 2nd, 55 turns for the 3rd, 34 turns for the 4th and 5th, 19 turns for the 6th and 7th layers. b) Magnetic field profile in the second Zeeman slower for a current of 3.6 A. The dots are the experimental data and the plain line is the theoretical field fitted with the attenuation factor α as a free parameter (see text).

obtained after the first Zeeman section shifted by a constant time delay. As shown by the figure 1.7 the temporal width of the decelerated atomic bunch is much larger after the complete slowing process than after the first Zeeman. This model can not describe this broadening but allows to determine the value of the final velocity to be $v_f = 55 \pm 5 \text{ m}\cdot\text{s}^{-1}$.

The efficiency of the atomic beam deceleration can be evaluated comparing the areas of the free propagating and slow atomic bunches. The deceleration to v_f has an overall efficiency of 80%, which is satisfactory. Indeed the capture velocity v_c into a magneto-optical trap (MOT) can be evaluated from the maximal deceleration, $a_{max} = \hbar k \Gamma_0 / 2m$ transferred to one atom by the light inside one MOT beam waist: $v_c = \sqrt{w a_{max}} \approx 68 \text{ m}\cdot\text{s}^{-1}$. After the deceleration with our two Zeeman slowers, all the atoms will thus be captured in the MOT.

1.3 Magneto-optical trap

Suggested by J. Dalibard and first established by Raab *et al.* [60], magneto-optical trapping allows to collect and cool large number (of the order of 10^8) of atoms captured from a slow atomic beam or from a vapor.

The trapping scheme of our magneto-optical trap (MOT) has been considerably modified in the course of the rebuilding of the experiment in its current state. A new quartz cell has been mounted and a completely new magnetic trap, which will be described in more details in the next section, is now operational. With those modifications we can trap typically $2 \cdot 10^8$ atoms at a temperature of 2 mK.

1.3.1 Performances

A magneto-optical trap (MOT) results from radiation pressure forces of 3 pairs of two counter-propagating laser beams crossing at the center of a quadrupole, produced by two coils in an anti-Helmoltz configuration. The MOT beams are red-detuned and circularly σ^+ and σ^- polarized so that a cycling transition is excited when the atom moves away from the trap center.

In the previous experimental setup two of the MOT beams had to share the path of the Zeeman optical beam. This configuration induced depumping of the atoms from the deceleration process at two positions and thus to considerable losses (see [58]). Both a repumping beam and a much higher power in the Zeeman beam were required. In this regime the MOT was pushed by the Zeeman beam despite its large detuning from the resonance, compromising a good transfer of the atomic cloud into the magnetic trap.

The larger dimensions of the new quartz cell ($10 \times 4 \times 6$ cm³) offer more optical access and enable to choose other axis for those beams. The new geometry of the MOT beams is schematically represented in figure 1.9.

The center of the MOT is now located 14 cm behind the end of the second Zeeman. This distance has been minimised within the geometrical constraints in order to limit the effect of ballistic expansion of the slow atomic beam. Our residual lateral velocity of $5 \text{ m}\cdot\text{s}^{-1}$ causes a 10 mm enlargement of the atomic beam diameter at the new position of the MOT. Hence this expansion should not create losses since the MOT optical beams are expanded to 2 cm diameter at $1/e^2$.

The quadrupolar magnetic field is now produced by the two pinch coils of the clover-leaf magnetic trap described in chapter 2. Three power supplies (Delta Elektronika, 70 V - 45 A) connected in parallel provide 100 A resulting in an optimal gradient of $38 \text{ G}\cdot\text{cm}^{-1}$.

A magneto-optical trap of metastable Helium atoms has some specificities due to the Penning collisions introduced in chapter 0.1. For non polarised trapped atoms, the collision rate β is of the order of $10^{-10} \text{ cm}^3\cdot\text{s}^{-1}$ and depends on the detuning and the intensity of the MOT beams as studied in [61]. Indeed resonant light may induce an atomic transition to the 2^3P_2 state, which is interacting more strongly with the atoms in the 2^3S_1 metastable state and has a higher probability to collide (more partial waves are involved) and Penning ionise. To overcome this drawback the laser beams are far detuned from

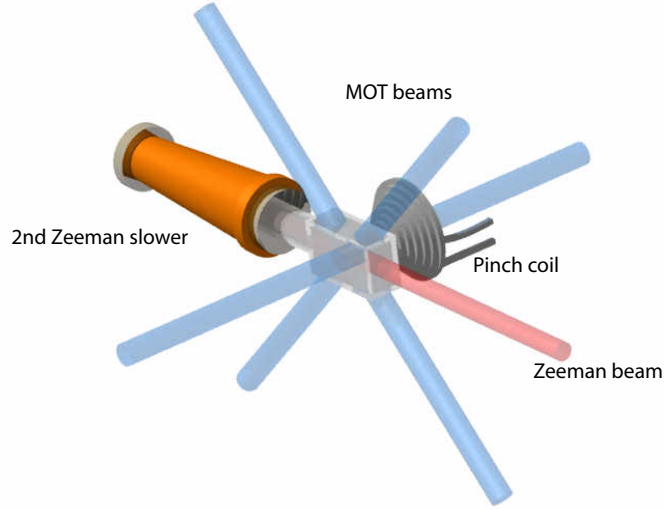


Figure 1.9: *New geometry of the experimental setup. The Zeeman beam is depicted in red, the MOT beams in blue. Two MOT beams are crossing the cell at 45° in a vertical plane and the third one is horizontal and orthogonal to the cell. For a simpler overview the second pinch coil, used to create the MOT magnetic field, is missing.*

the atomic transition in order to minimise the population of the excited state. The atom number is maximal for a detuning of $-45 \text{ MHz} \approx 28 \Gamma_0$. Also the atomic density is reduced, taking advantage of the large diameter of the MOT beams in order to form a large size cloud.

After 500 ms of loading, $2 \cdot 10^8$ atoms are confined in the MOT as shown in figure 1.10. The temperature achieved at the MOT stage is deduced to be 2 mK from absorption imaging (see Appendix A). From such a measurement of the expansion of the cloud widths after release, the RMS radii in situ can be extrapolated to $\sigma_{vert} = 3.3 \text{ mm}$ and $\sigma_{hor} = 4 \text{ mm}$. With $2 \cdot 10^8$ atoms in the trap, the central density is thus $n(\mathbf{0}, t_0) = 2 \cdot 10^9 \text{ cm}^{-3}$.

1.3.2 Collisional regime in the MOT

In the magneto-optically trapped cloud described here, the atom number is limited by two-body losses resulting from light-assisted Penning ionisation events. To demonstrate this point, the atom number trapped in the stationary regime is studied as a function of the loading rate.

Considering one and two body losses (characterised respectively by a lifetime τ and a rate constant β), the evolution of the atom number $N(t)$ under a loading rate Φ can be expressed as a function of the density $n(\mathbf{x}, t)$ in the trap:

$$\frac{dN}{dt} = \Phi - \frac{N(t)}{\tau} - \beta \int n^2(\vec{r}, t) d^3\vec{r}. \quad (1.7)$$

The second term, linear in the atom number, is mainly due to Penning ionization with background gases and the quadratic part is attributed to Penning collisions between

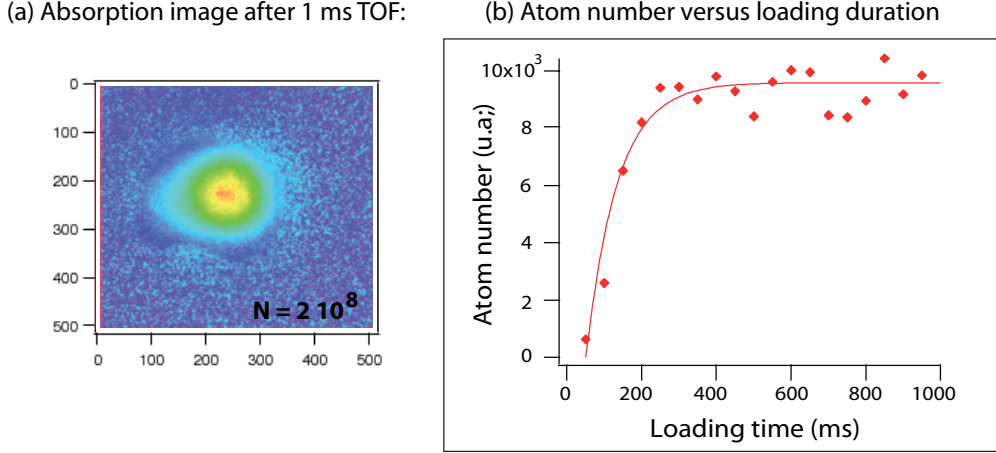


Figure 1.10: *Characterisation of a typical MOT at -45 MHz. a) Absorption image of the MOT after 1 ms time-of-flight. Such an image allows to deduce a total atom number of $2 \cdot 10^8$ and also the cloud widths (see Appendix A). b) Measurement of the number of atoms trapped in the MOT for different loading durations. The maximum atom number, expressed here as the integral of the optical density, is achieved after approximately 500 ms loading.*

trapped atoms, for which the collision rate constant β has been defined in section 1.3.1. The atomic density in the trap presenting a cylindrical symmetry around (Oz) is well described by a Gaussian distribution which can be factorised as:

$$n(\vec{\rho}, z, t) = n(0, t) e^{-\frac{\rho^2}{2\sigma_\rho^2}} e^{-\frac{z^2}{2\sigma_z^2}}, \quad (1.8)$$

with σ_r and σ_z independent from the atom number and time. The integration of equation 1.7 leads to:

$$\frac{dN}{dt} = \Phi - \frac{N(t)}{\tau} - \frac{\beta}{2\sqrt{2}V} N^2(t), \quad (1.9)$$

with $V = (2\pi)^{3/2} \sigma_\rho^2 \sigma_z$ being the trap volume.

When the two body collisions can be neglected, the stationary atom number in the trap is $N_s = \Phi\tau$, depending linearly on the loading rate.

In the opposite case, where two body collisions dominate ($\beta n_s \tau \gg 1$), the atom number in the stationary regime is given by:

$$N_s = \sqrt{\frac{2\sqrt{2}V\Phi}{\beta}} \quad (1.10)$$

which is then proportional to the square root of the loading rate Φ . Figure 1.11 a) reports on the scaling of the trapped atom number with the atomic flux. The collimation/deflection light was modulated at 1 kHz and a MOT was loaded for various duty cycles. The modulation period was carefully chosen to be both:

- larger than the time spent by an atom in the collimation deflection section (of the order of 0.1 ms) to maintain the deflection angle constant

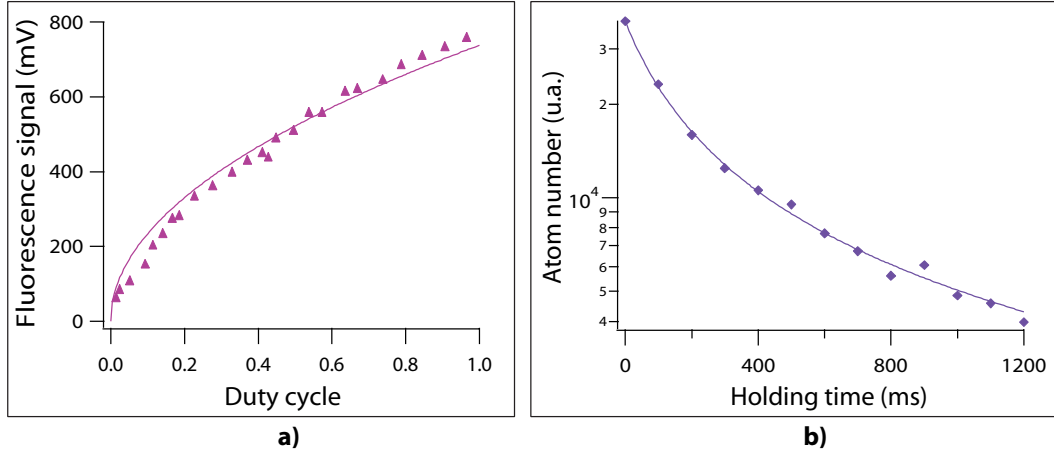


Figure 1.11: a) Trapped atom number versus loading rate: the MOT fluorescence has been measured for different duty cycles. The plain line is a square root fit. b) Lifetime measurement in a semi-logarithmic scale. This graph shows a clear non-exponential decay of the atom number. The data are fitted by equation 1.11 with the Penning collision rate constant as free parameter.

- smaller than the loading time of the MOT (in the range of 100 ms).

As expected, the atomic flux, measured on the second Faraday cup, varies linearly with the duty cycle of the modulation. The total atom number achieved in stationary regime was determined by fluorescence measurement. Its variation is well described by a square root scaling on the loading rate. This experiment confirms that two body losses are limiting the atom number in the MOT for a given flux, corresponding for metastable atoms to light-assisted Penning ionisation.

Since light-assisted Penning collisions are limiting the lifetime, the expected decay of the atom number in time follows [61]:

$$N(t) = \frac{N(t_0)}{1 + \frac{\beta}{2\sqrt{2}}n(\mathbf{0}, t_0)(t - t_0)} \quad (1.11)$$

where β is the light-assisted Penning collision rate constant for non polarised atoms. The lifetime of the MOT is determined experimentally from the evaluation of the atom number at different holding time using absorption imaging (see figure 1.11 b)).

Assuming an initial density of $n(\mathbf{0}, t_0) = 2 \cdot 10^9 \text{ cm}^{-3}$ determined from the other measurements presented in this section, the fit of this model on the experimental data presented in figure 1.11 b) provides a determination of this inelastic collision rate: $\beta = 1.4 \cdot 10^{-9} \text{ cm}^3 \cdot \text{s}^{-1}$ within a factor of 2 accuracy. This value depends both on the detuning of the MOT beams fixed at -45 MHz and their intensity ($50 I_{sat}$). This result is in agreement with the results found in [58] for a comparable MOT beam detuning of and a larger intensity of $80 I_{sat}$.

1.3.3 Channeltron diagnosis

Some characteristics of the MOT can also be determined taking advantage of the new channeltron detector located in the science cell. Two kinds of signals can be recorded: either ions produced by Penning ionisation processes in the trapped atomic cloud or metastable atoms hitting the detector during their time-of-flight (TOF).

Ion signal: In the MOT, the number of ions produced per unit time is given by:

$$\frac{dN_{ion}(t)}{dt} = \beta \int n^2(\vec{r}, t) d^3\vec{r}. \quad (1.12)$$

Assuming the trap volume V independent of the atom number and time, as in the previous paragraph, equation 1.12 can be rewritten as:

$$\frac{dN_{ion}(t)}{dt} = \beta \frac{N^2(t)}{2\sqrt{2}V} \quad (1.13)$$

The ion rate detected on the channeltron is thus simply proportional to the square of the atom number. A second lifetime measurement has thus been realised, recording the channeltron signal after the end of the MOT loading. Such a signal, shown in figure 1.12, allows to deduce the MOT lifetime from a single realisation of the experiment, on the contrary to absorption imaging, where images are taken for different holding times as reported in figure 1.11 b). The experimental data can be fitted by equation 1.11 in order to deduce the product $n(0, t_0)\beta$. The results obtained are in agreement with the lifetime measurement obtained by absorption imaging reported in figure 1.11 b).

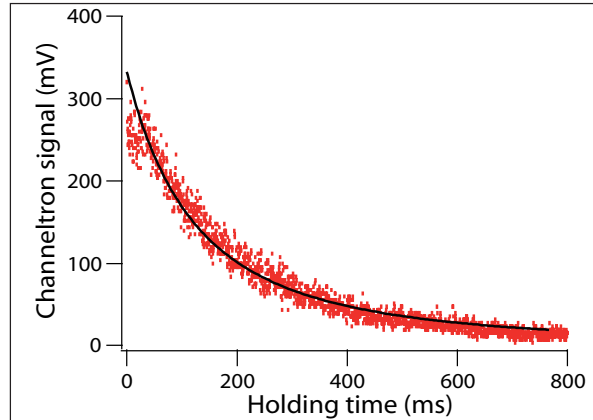


Figure 1.12: Ion rate recorded by the channeltron once the loading has been stopped. $t=0$ corresponds to the time at which the loading is stopped. The plain line corresponds to $N^2(t)$ as expressed in equation 1.11 with the product $n(\mathbf{0}, t_0)\beta$ as fitting parameter.

Atomic signal: When the MOT beams and the quadrupole magnetic field are switched off, the atomic cloud expands under gravity and falls onto the channeltron. Only a fraction of atoms will hit the detector which is lying 1.7 cm below the center of the MOT

and 5 cm sideways (see figure 1.13 a)). From this time-of-flight signal, presented in figure 1.13 b), one can retrieve the temperature of the atomic cloud.

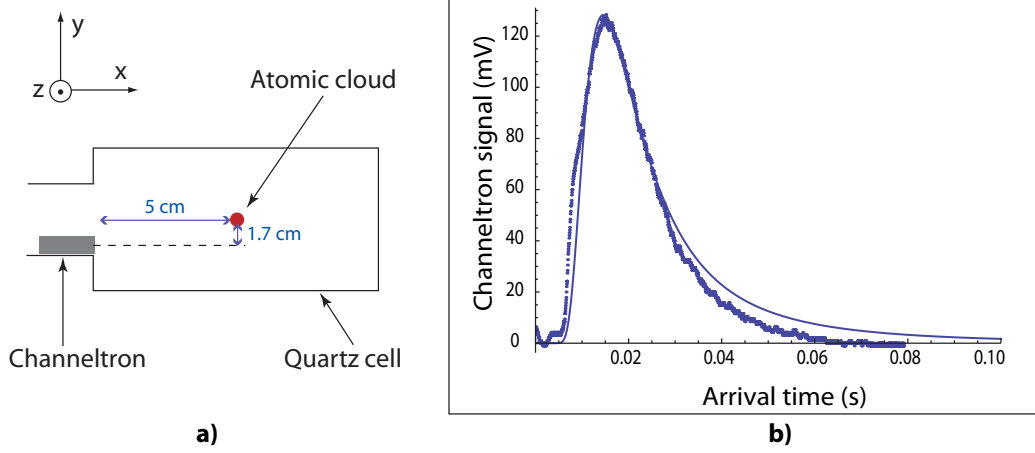


Figure 1.13: a) Schematic representation of the position of the channeltron inside the quartz cell. b) Time-of-flight signal of the MOT recorded on the channeltron. The line represents the analytic model from equation 1.21, for a temperature $T= 2$ mK of the MOT, in good agreement with the determination using optical imaging.

To model the experimental data, the cloud is assumed to be point-like and thus the problem is reduced to a two-dimensional one in the $z=0$ plane of the referential defined in figure 1.13 a). The origin of the coordinates is taken to be the initial location of the atomic cloud, and the position of the detector will be denoted $(x_d, y_d)=(-5$ cm, -1.7 cm). A Maxwell Boltzmann isotropic probability distribution for the velocities along x and y is assumed:

$$N(v_x, v_y) = \frac{1}{2\pi\sigma_T^2} \exp\left(-\frac{v_x^2 + v_y^2}{2\sigma_T^2}\right) \quad (1.14)$$

where $\sigma_T = \sqrt{k_B T/m}$.

To retrieve the channeltron signal, one has to transform equation 1.14 from a function of (v_x, v_y) to a function of (y, t) , the x position of the detector being fixed at x_d .

We use Newton's equations for a ballistic motion of a particle accelerated by the earth's gravitational field to find the relationship between those two coordinates systems:

$$x_d = v_x t \quad (1.15)$$

$$y = v_y t - \frac{1}{2} g t^2 \quad (1.16)$$

After inversion one gets:

$$v_x = \frac{x_d}{t} \quad (1.17)$$

$$v_y = \frac{y}{t} + \frac{1}{2} g t \quad (1.18)$$

To determine how the differential $dv_x dv_y$ transforms into $dydt$, we use the Jacobian determinant J which is:

$$J = \begin{vmatrix} \frac{\partial v_x}{\partial y} & \frac{\partial v_x}{\partial t} \\ \frac{\partial v_y}{\partial y} & \frac{\partial v_y}{\partial t} \end{vmatrix} = \begin{vmatrix} 0 & -\frac{x_d}{t^2} \\ -\frac{1}{t^2} & -\frac{y}{t^2} + \frac{g}{2} \end{vmatrix} = \frac{x_d}{t^3} \quad (1.19)$$

Finally, the number of atoms detected at a time t at a position y is given by:

$$N(y, t) = \frac{x_d}{t^3} \frac{1}{2\pi\sigma_T^2} \exp\left(-\frac{(x_d/t)^2}{2\sigma_T^2}\right) \exp\left(-\frac{(y/t + gt/2)^2}{2\sigma_T^2}\right) \quad (1.20)$$

and the fraction of atoms detected reads:

$$N_d(t) = \int_{y_d-L_d}^{y_d+L_d} N(y, t) dy \quad (1.21)$$

where $L_d= 2$ mm is the size of the detector along y .

This analytic model is used to fit the experimental data reported in figure 1.13 b). The two fitting parameters were the temperature T and the detection efficiency via a coefficient A . The best adjustment is obtained for $T= 2$ mK, in agreement with the value determined by absorption imaging (see Appendix A).

1.4 Conclusion

In this chapter the main changes implemented on the experimental setup during this thesis work have been presented. The stability has been greatly improved by fiber coupling all the optical beams involved in the production of a slow atomic beam of metastable Helium atoms and the trapping of those atoms in a MOT. The experimental sequence is now computer controlled by a new LabView program, which also retrieves and analyses the data from the CCD camera.

This chapter also aims at demonstrating the new insights offered by the detection device mounted inside the science chamber. Therefore the diagnosis provided by this channeltron are modeled and analysed in order to obtain detailed informations on the experimental setup.

The different stages of the production of a slow atomic beam of metastable Helium atoms are fully characterised with the help of the channeltron signal. A study of the arrival time distribution of atomic bunches allowed to determine precisely the longitudinal velocity profile of the atomic beam and to characterise its propagation inside the Zeeman slower. The final velocity and the efficiency of the slowing process have been quantitatively determined.

Finally, we demonstrate the trapping of $2 \cdot 10^8$ atoms in a MOT at a temperature of 2 mK. The setting up of a new quartz cell of larger dimensions offers a new geometrical arrangement of the MOT beams, which avoids the use of the Zeeman axis as was done previously [58] and thus losses during the slowing process.

The study of the number of trapped atoms in the stationary regime as a function of the loading rate provides a clear proof of a limitation due to inelastic light-assisted Penning collisions. The MOT lifetime is studied both via absorption imaging and the ion signal recorded by the new channeltron.

Finally the time-of-flight signal of metastable atoms falling onto the channeltron after release from the MOT is modeled in order to deduce the temperature of the trapped cloud, showing a good agreement with the value derived from absorption imaging (see Appendix A).

Chapter 2

Novel magnetic trap for Bose Einstein Condensation

Temperatures achieved in a MOT or optical molasses are limited to a level of several hundreds of μK by the heating effect due to spontaneous emission. To decrease further the temperature and increase the phase-space density, atoms are transferred into the conservative potential of a magnetic trap, where evaporative cooling is realised.

The design of this novel magnetic trap allows to produce the condensate and efficiently load it in-situ into any optical potential. For experiments involving optical traps, optical access constitutes a crucial issue. Several solutions have been developed, among which two main trends appear: either reach the degeneracy in an all optical trap or perform the MOT and the optical lattice in different chambers. The first scheme does not easily apply to a metastable helium MOT having a temperature of 2 mK and large dimensions (see section 1.3.1): a direct loading would require an important dipole trap depth along with a rather large beam focus. The second solution involves the transport of the cold cloud, either by optical [47], magnetic [62] or mechanical [63] means into a science chamber offering additional optical access. However, such a spatial displacement of atoms adds to the complexity of the setup and induces losses in the metastable atomic cloud.

The new cloverleaf trap presented in this chapter, provides an optical arrangement where the MOT, the Bose-Einstein condensate (BEC) and the optical lattice can be all produced at the same place. As can be seen in figure 2.1, gaps between the cloverleaf coils have been enlarged so that eight optical beam axis are now available. The technical difficulties resulting from the transport are thus avoided.

Technical details concerning the electrical circuit and its performances for the switching of the currents are presented in the second section. Indeed the magnetic coils have a small number of turns to keep a compact configuration and thus large currents are used (≈ 300 A).

The third section details the experimental sequence implemented to load the atoms into the magnetic trap and achieve a phase-space density of $\chi \approx 7 \cdot 10^{-6}$.

The first results obtained with RF frequency and evaporative cooling are finally reported.

2.1 Cloverleaf magnetic trap

2.1.1 Ioffe-Pritchard potential

The potential energy of an atom with a magnetic moment $\vec{\mu}$ in an external field \vec{B} is expressed as a scalar product:

$$U(\mathbf{r}) = -\vec{\mu} \cdot \vec{B}(r). \quad (2.1)$$

When the quantization axis is along the magnetic field vector, the projection of the magnetic moment becomes $\mu = -gm_J\mu_B$, with μ_B the Bohr magneton and g the Lande factor. For the 2^3S_1 metastable state, the Lande factor g equals 2, allowing for a more efficient magnetic trapping than for alkali atoms. Atoms in the state (2^3S_1 , $m_J=+1$) will be trapped at a minimum of the magnetic potential. Magnetic trapping of neutral atoms was first demonstrated using a quadrupole magnetic field, produced by two coils in an anti-Helmoltz configuration [64]. The zero-crossing of the magnetic field at the center causing Majorana spin flips [65] and thus atom losses, harmonic potentials as produced by the Ioffe Pritchard configuration have been favoured [66].

Our setup (see figure 2.1) is based on the cloverleaf trap geometry, modified to offer additional corridors for laser beams to pass through. Two axial coils, called *pinch coils*, are arranged in a Helmholtz configuration, providing axial confinement along the Z -axis, well approximated by a harmonic potential near the trap center. For the radial confinement, each pinch coil is surrounded by four *cloverleaf coils* and connected in an anti-Helmoltz configuration to produce a quadrupolar waveguide field along the Z -axis. Finally, two larger axial Helmholtz coils, called *compensation coils*, are added. They create a quasi uniform field compensating for the large field produced by the pinch at the center of the trap.

The field produced by this arrangement, expressed in cylindrical coordinates, can be approximated near the center by [67]:

$$B_\rho = B'\rho\sin(2\psi) - B''z\rho \quad (2.2)$$

$$B_\psi = B'\rho\cos(2\psi) \quad (2.3)$$

$$B_z = B_0 + B''z^2 - \frac{B''}{2}\rho^2 \quad (2.4)$$

where B_0 is the field value at the center. The axial curvature B'' and the radial gradient B' can be changed independently via the current in the axial and the radial coils respectively. The absolute field is given by:

$$|\mathbf{B}| = \sqrt{(B'^2 - B_0 B'')\rho^2 + (B_0 + B''z^2)^2 - 2B'B''z\rho^2\sin(2\psi) + \frac{1}{4}B''^2\rho^4} \quad (2.5)$$

For small He* clouds lying at the center of the trap, $|\mathbf{B}|$ can be approximated by the second-order expansion of the square root giving a potential:

$$U(\rho, z, \psi) \approx 2\mu_B B_0 + 2\mu_B (B''z^2 + \frac{1}{2}(\frac{B'^2}{B_0} - B'')\rho^2) \approx U_0 + \frac{1}{2}m(\omega_z^2 z^2 + \omega_\rho^2 \rho^2) \quad (2.6)$$

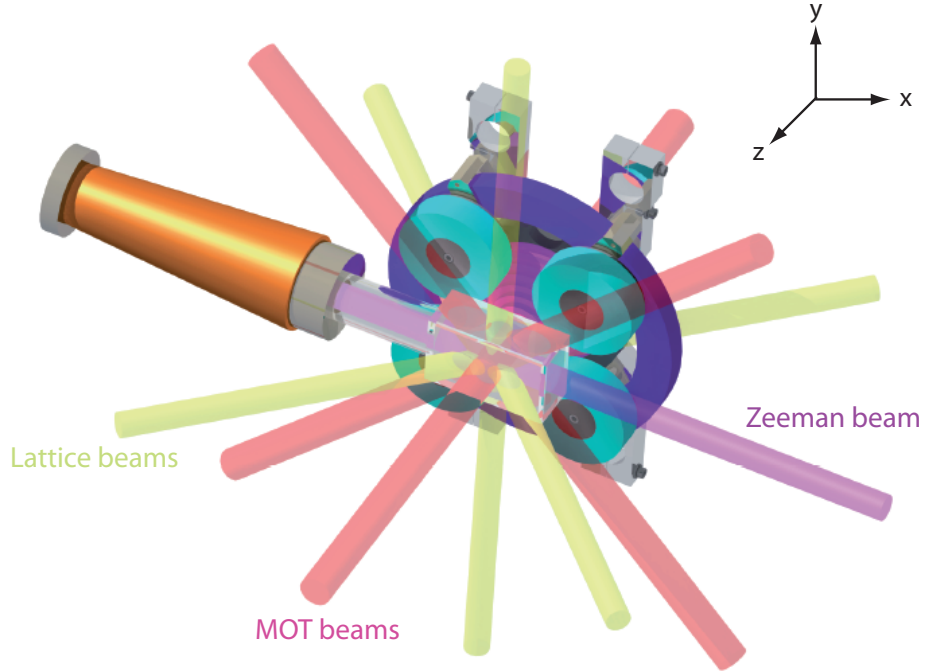


Figure 2.1: *Three-dimensional view of the coil and beam geometry. The $Z=0$ plane is a plane of symmetry for the coil arrangement. In the Z -positive direction the coils are not represented to simplify the overview. The geometry offers distinct paths for the Zeeman beam, the three MOT beams and up to three lattice beams.*

with ω_z and ω_ρ the axial and radial frequencies:

$$\omega_z = \sqrt{\frac{4\mu_B B''}{m}} \quad (2.7)$$

$$\omega_\rho = \sqrt{\frac{2\mu_B (B'^2/B_0 - B'')}{m}} \quad (2.8)$$

Since the radial frequency depends on B_0 , the trap can be compressed radially while reducing the axial bias field at the trap center.

The simulations of the magnetic field produced by this trap were realised for a current of 300 A giving a radial gradient of $B' = 60 \text{ G}\cdot\text{cm}^{-1}$ and an axial curvature of $B'' = 39 \text{ G}\cdot\text{cm}^{-2}$. The resulting axial and radial frequencies are $\omega_z = 2\pi \cdot 74 \text{ Hz}$ and $\omega_\rho = 2\pi \cdot 500 \text{ Hz}$ for a bias field $B_0 = 1 \text{ G}$.

2.1.2 Trap design

The main advantage of the cloverleaf configuration is to offer a free optical access in the full XY plane, as can be seen in figure 2.1. The standard geometry has been adapted to provide additional corridors in the XZ plane for optical beams.

A laser beam can propagate along the Z -axis through the central tunnel of the pinch coils. Their conical shape and an increased spacing between the cloverleaf coils creates

two additional corridors of 25 mm at 45° in the XZ plane. As sketched in figure 2.1 the mechanical arrangement leave enough optical access for two distinct sets of beams for the MOT and the 3D optical lattice.

In order to obtain a compact geometry, the coils are designed with few turns (see figure 2.2) and large currents are used. The narrow dimensions of the new glass cell ($10\text{ cm}\times 6\text{ cm}\times 4\text{ cm}$) enable to position the magnetic coils only few cm away from the atomic cloud and therefore achieve large fields.

The coils are made from copper bars with a square cross section of $5\times 5\text{ mm}^2$ and a $3\times 3\text{ mm}^2$ central bore for water cooling. Electrical isolation of the conducting bars is realised using Kapton film. The detail of the coils winding is shown in figure 2.2 b), where each square represents the external profile of the wire. All the coils are supported by two platforms with the shape of the letter 'H' (each platform holding one compensation, one pinch and 4 cloverleaf coils) connected by four non-conducting rods to avoid conductive loops, which are made from re-enforced glass fiber, represented in figure 2.2 a).

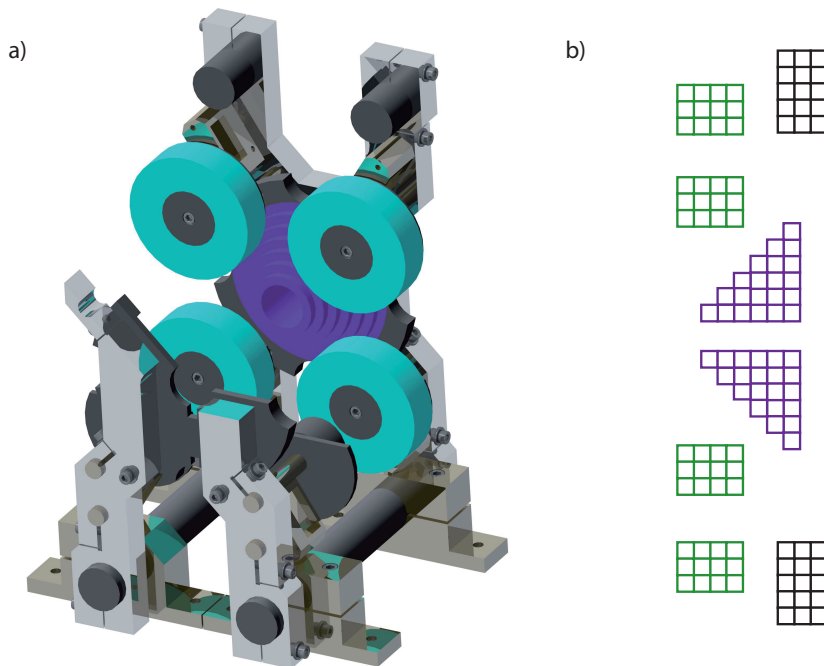


Figure 2.2: a) Mechanical mount holding the coils. Two platforms having an 'H' shape are connected with four non-conducting rods made from re-enforced glass fiber in order to avoid conductive loops. Only four cloverleaf coils in green and one conical pinch coil in lila are represented here to show the enlarged spacing between them opening new optical corridors in the XZ plane. b) Cut through the coils to expose the wiring in a plane resulting from a rotation of the XY -plane by 45° around the Z -axis. Each square represents the $5\times 5\text{ mm}^2$ external profile of the copper bars. The two cloverleaf coils are represented in green, the pinch coil in lila and the compensation coil in black.

A commercial chiller working in closed-circuit mode provides a pressure of 6 bars for

the water cooling of the magnetic coils. A typical water flow of 3 l.min^{-1} is split between five groups of coils having a comparable hydraulic resistance: the two compensation coils are fed in parallel, each pinch coil is fed in series with 2 cloverleaf coils and the last group consists of four cloverleaf coils in series. During a typical experimental sequence, for which the magnetic trap current of 300 A is on during 15 s, no heating of the coils has been resolved. Only the temperature of the feeding cables, non water-cooled, is increasing by 10 C° .

2.2 Electric circuit

The magnetic coils produce both the quadrupolar magnetic field, required during the MOT phase, and the Ioffe-Pritchard potential presented in paragraph 2.1.1. Those two field configurations require respectively an Helmholtz and an anti-Helmholtz configuration for the pinch coils. Therefore the current in one of the pinch coil has to be reversed to load the atoms from the MOT into the magnetic trap. The large velocity of helium atoms before loading sets a higher limit of $500 \mu\text{s}$ on the duration of the switch between the quadrupolar and the Ioffe-Pritchard potentials. Another requirement is the ability to switch off the large currents in the coils within few hundreds of microseconds, to minimise the perturbative effect of magnetic fields during the probing of the released atomic cloud. The complete electrical scheme conceived to satisfy those conditions is represented in figure 2.3.

It consists of four sections having specific functions and constraints. Two distinct sets of power supplies are used for the quadrupolar and Ioffe-Pritchard field configurations and several insulated gate bipolar transistors (IGBT) control the current route. The third section has been designed to accelerate the rising of the current at the beginning of the magnetic trapping phase. The control on the bias field, essential to compress the atomic cloud, is achieved with a last power supply feeding the compensation coils with a current in the reverse direction.

2.2.1 Quadrupolar field for the MOT

Three identical power supplies (Delta Elektronika, 70 V - 45 A) connected in parallel provide 100 A flowing through the pinch coils in an anti-Helmholtz configuration. In figure 2.3 they are denoted PS MOT and to drive the current the IGBTs $I1$ and $I4$ are open whereas $I6$ and $I7$ are closed.

The gradient of the resulting quadrupolar field is measured to be $38 \text{ G}\cdot\text{cm}^{-1}$.

Fast cut off of the current is insured by the two IGBTs $I6$ and $I7$. At the moment of switch off, very large voltages proportional to the pinch coil inductance $L = 30 \mu\text{H}$ (see table 2.1), the current of 100 A and inversely proportional to the switching time are experienced by the IGBTs. To protect the IGBTs from overvoltage, a varistor, mounted in parallel maintain a constant voltage $U_V = 275 \text{ V}$. The current decreases then within $100 \mu\text{s}$ as reported in figure 2.4 a) and the magnetic field returns to zero within approximately 2 ms.

2.2.2 Ioffe-Pritchard trap

In the magnetic trap configuration, two power supplies connected in series (Agilent, 15 V - 440 A) produce a maximum current of 310 A. The IGBTs $I1$ and $I4$ are closed, in order to feed all the coils in series.

To work with a stable current, those power supplies are kept in a current-control mode using only $I_{max} = 280 \text{ A}$. For such a current, voltage drops on the diode $D3$ and the two

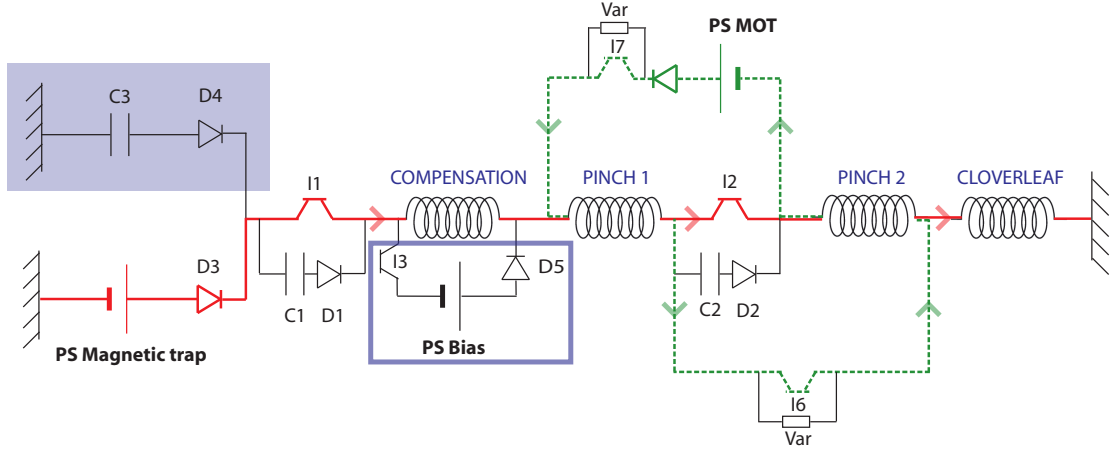


Figure 2.3: *Electrical circuit conceived to provide either a quadrupolar or a Ioffe-Pritchard potential. I1 and I2 are the IGBTs used to switch the current in all the coils; I6 and I7 to switch the anti-Helmholtz configuration in the pinch coils and I3 allows the current from **PS Bias** to flow in the compensation coils. C1, C2 and C3 are large electrolytic capacitors with $C = 1 \text{ mF}$. The current route represented as a green dashed line corresponds to the MOT configuration and as a plain red line to the Ioffe-Pritchard configuration. Two different power supplies, denoted **PS MOT** and **PS Magnetic trap**, produce the current during those two phases. The section in the blue box has been added in order to accelerate the rising of the current at the beginning of the magnetic trapping phase, using the capacitor C3. The last power supply, denoted **PS Bias** inside the blue border, is used to change independently the current passing through the compensation coils and thus control the bias field B_0 .*

IGBTs (2 V on each) limit the available voltage to 24 V. All the electrical connections are realised with large diameter cable and specific connectors to obtain a low total resistance. The corresponding voltage drop is 3.9 V. The magnetic coils, whose resistances are listed in table 2.1, require 18.2 V at I_{max} .

As already mentioned, each IGBT and diode having a voltage of 2 V for a current I_{max} needs to dissipate a power of approximately 600 W. All those components are therefore mounted on a water-cooled aluminium plate. The temperature increase during one sequence is less than 2°C.

	Resistance (mΩ)	Inductance (μH)	Length (m)
Compensation coil	12	30	10
Pinch coil	6	15	5
Cloverleaf coil	3.6	8	3

Table 2.1: *Measured resistance, inductance and length of the different magnetic coils. The trap consists in two compensation coils, two pinch coils and eight cloverleaf coils, corresponding to a total resistance of $R_{tot} = 65 \text{ m}\Omega$ and a total inductance of $L_{tot} = 154 \text{ }\mu\text{H}$.*

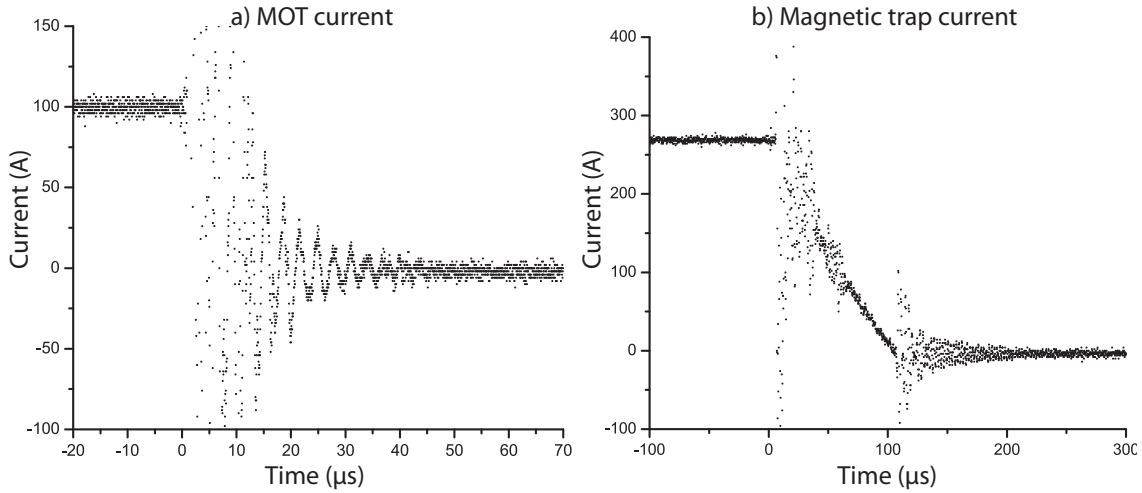


Figure 2.4: Switch of the current measured with a current clamp in one of the pinch coil. The origin of times corresponds to the switch of the IGBTs $I6$ and $I7$ for the MOT phase and $I1$ and $I4$ for the magnetic trap phase. a) After the MOT phase, the current is decreasing from 100 A to 0 A within 50 μs . b) In the magnetic trap, 300 A are flowing through the coils and the current goes to zero after 100 μs .

The IGBTs $I1$ and $I4$ have a maximum collector-emitter voltage of $V_{CE,max} = 1.2$ kV and the collector current has to stay below 600 A. They are deliberately oversized in order to limit the voltage drops reaching 2.5 V on each for $I = 600$ A. Large electrolyte capacitors of capacity $C = 1$ mF (denoted $C1$ and $C2$ in figure 2.3), precharged at a voltage of $U_C = 160$ V by a separate power supply, protect each of the IGBT from overvoltage. When the voltage in the main path rises above U_C , the induced current will charge the capacitors. The surcharge will subsequently be absorbed by the capacitor power supply. The typical energy stored in the coils is $E_L = LI^2 \approx 14$ W and is dissipated in the capacitor at the switch off.

The voltage U_C of the capacitors $C1$ and $C2$ could be set higher (up to 1 kV), but is here limited by the voltage available from the power supplies used to charge them. The complete extinction of the currents in the magnetic coils is achieved after 100 μs as reported in figure 2.4 b).

The three dimensional magnetic field has been measured both along the X -axis and the Z -axis with a Hall probe. It matches the theoretical calculations obtained from the Biot-Savart law and the measurement of the coils positions as shown in figure 2.5.

2.2.3 Switch between the two configurations

The rising time of the current in the magnetic trap is set by the ratio L/R of the coil inductance over their resistance. For the present setup this corresponds to $\tau \approx 3$ ms and a measurement gives 5 ms (see figure 2.6). As will be detailed in the next section, the cloud temperature before loading the magnetic trap is approximately 300 μK and thus

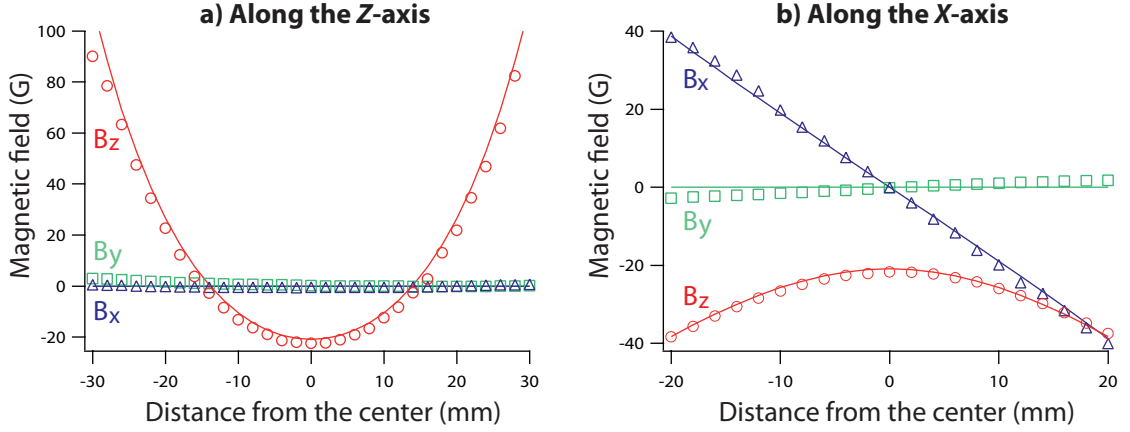


Figure 2.5: *Magnetic field produced by the magnetic trap for a current of 100 A. The three dimensional field has been measured with a Hall probe both along the Z-axis a) and the X-axis b) of the trap: the z-component of the magnetic field is shown as red dots, its x-component as the blue triangles and its y-component as the green squares. The calculated magnetic field components, represented by plain lines, are in agreement with the measured field.*

the thermal velocity of metastable helium atoms is of the order of $80 \text{ cm}\cdot\text{s}^{-1}$. During the switching time τ the cloud widths expand by a factor of approximately 1.6 and the phase-space density is thus reduced by a factor of the order of 4.

In order to reduce this rising time, a capacitor $C3$ is charged under a voltage U_{switch} , storing an energy of $\frac{1}{2}CU_{switch}^2$. When the IGBTs $I1$ and $I4$ are closed, the capacitor unloads in a quarter of period of the L-C circuit, which is $T = \frac{\pi}{2}\sqrt{LC} \approx 500 \mu\text{s}$. The capacitor's voltage decreases until it reaches the voltage of the magnetic trap power supplies, which then provide the electrical power. The voltage U_{switch} of the precharged capacitor should be such that the energy E_L which has to be transferred to the magnetic coils is equal to the energy stored in the capacitor E_C . This corresponds to a voltage $U_{switch} = 120 \text{ V}$. The final voltage has been adjusted to optimise the magnetic trap loading at $U_{switch} = 160 \text{ V}$. Figure 2.6 a) shows the current rise in one of the pinch coils, measured with a current clamp, with and without the capacitor $C3$. As expected, the current reaches its maximal value within $500 \mu\text{s}$ (see figure 2.6 b)).

2.2.4 Control of the bias field

The compensation coils are designed to overcompensate the field at the center when fed with the same current than the pinch coils as measured and reported in figure 2.5. A last power supply (Agilent, 15 V - 440 A) drives a reverse current in the compensation coils, so that the offset field, denoted B_0 , returns to a positive value and can be controlled. Equation 2.8 shows that reducing B_0 leads to an increase of the radial frequency $\frac{1}{2\pi}\omega_\rho$. This is essential in order to compress the atomic cloud and increase its spatial density before starting the evaporative cooling as will be detailed in the next section.

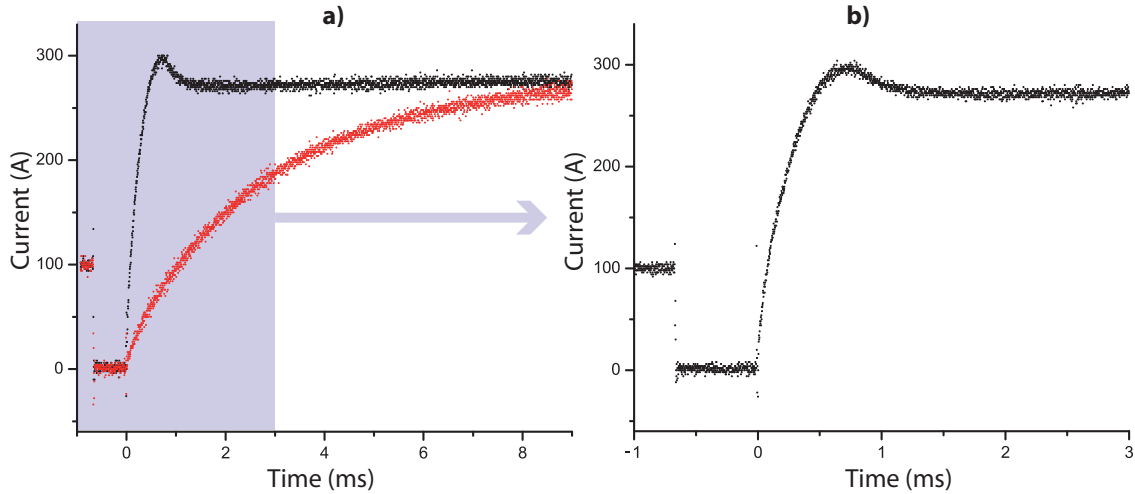


Figure 2.6: *Current rise in the magnetic trap coils. The current is measured with a current clamp in one of the pinch coil. The origin of times corresponds to the switch of the IGBTs I1, I3 and I4. a) The red curve corresponds to the current driven by the magnetic power supplies and the black one to the fast rise realised using the precharged capacitor C3. b) Fast current rise on a shorter time scale. After 500 μ s the current reaches its stationary value.*

The power supply, denoted PS Bias in figure 2.3, drives an inverse current I_{PSBias} ranging from 80 A to 68 A into the compensation coils. Its fluctuations are not correlated to the one of the power supplies driving the main current through all the coils in series, resulting in larger current fluctuations in the compensation coils than for the rest of the trap. A 200 mA rms current fluctuations is specified for the power supplies used. As a consequence the fluctuations of the compensation coils current is expected to be of the order of 300 mA, which corresponds to a 0.9 G rms fluctuation of the value of the bias field. This may be overestimated since the current provided by the power supplies are lower than their maximal values. Nevertheless instabilities of the bias field could be observed and prevented a further optimisation of the evaporative cooling. The relative positions of the magnetic coils have now been changed so to need less reverse current in the compensation coil and achieve a better stability.

The bias field B_0 has been measured using radio-frequency (RF) spectroscopy on an atomic cloud stored in the Ioffe-Pritchard trap, for different values of the current driven through the compensation coil. A RF excitation is applied during one second and, after release, the remaining atom number is determined by absorption imaging. The RF-frequency f_{RF} is scanned and the bias field value corresponds to the first RF-frequency at which all the atoms are lost. B_0 can be measured with an accuracy of 0.4 mG¹, but the current, measured with a current clamp, can only be determined within ± 1.2 A. Figure 2.7 shows two scans of the RF frequency and a graph of B_0 as a function of the current

¹This accuracy is essential to start evaporative cooling where the value of B_0 is set to 1 G, in order to achieve large trapping frequencies.

of PS Bias. The plain line represents a linear fit of the form:

$$B_0 = \alpha I_m + \beta(I_m - I_{PSBias}) \quad (2.9)$$

where αI_m and $\beta(I_m - I_{PSBias})$ are the magnetic fields created at the center respectively for a current I_m through the cloverleaf and pinch coils and for a current $I_m - I_{PSBias}$ through the compensation coils. The adjustment to the data points with I_m fixed at 294 A gives $\alpha = 0.72 \pm 0.03 \text{ G}\cdot\text{A}^{-1}$ and $\beta = 0.93 \pm 0.04 \text{ G}\cdot\text{A}^{-1}$. Those value are in agreement with the calculated magnetic field: $\alpha = 0.75 \pm 0.05 \text{ G}\cdot\text{A}^{-1}$ and $\beta = 0.98 \pm 0.02 \text{ G}\cdot\text{A}^{-1}$ (the error bars result from the measurement of the position of the different coils).

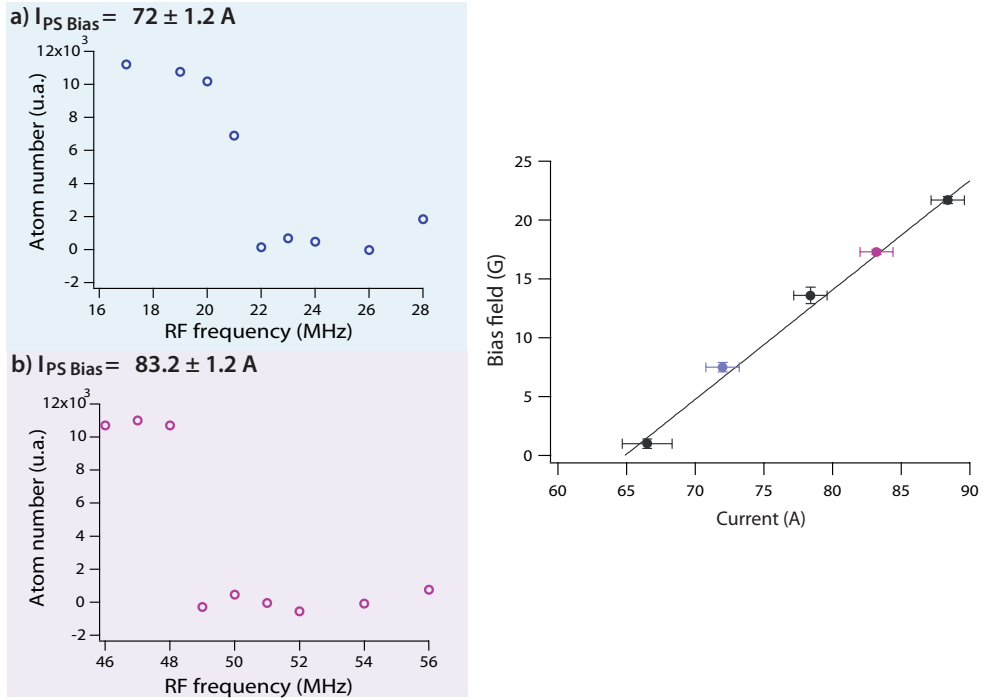


Figure 2.7: a) and b) are two RF-spectroscopy scans: the remaining atom number after one second of RF excitation is measured via absorption imaging for different RF-frequencies. The first RF frequency for which atoms are transferred to non-trapped m_J states and therefore lost, is a measurement of $B_0 = hf_{RF}/2 \mu_B$. On the right hand side, the measured values of the bias field are reported as a function of the current in PS Bias. The blue and purple points corresponds to the values extracted from the scans a) and b). The largest error bars on the data points arise from the current measurement realised with a current clamp limiting the accuracy to $\pm 1.2 \text{ A}$. The plain line corresponds to the fit described in the text.

Table 2.2 summarizes the values of the Ioffe-Pritchard trap parameters (trap frequencies and bias field) obtained for a current of 300 A and two different values of the PS Bias current, flowing through the compensation coils before and after compression of the trap respectively.

	ω_ρ (Hz)	ω_z (Hz)	B_0 (G)
$I_{PSBypass} = 80$ A	74	74	30
$I_{PSBypass} = 68$ A	500	74	1

Table 2.2: Trap frequencies and bias field for a current of 300 A passing through all the coils and I_{Bypass} driven in the opposite direction in the compensation coils. The two sets of values correspond to the Ioffe-Pritchard trap before and after compression.

2.3 Loading of the magnetic trap

This section details the different experimental steps required to load the atoms from the MOT into the magnetic trap. After a stage of 3D molasse and optical pumping, the atomic cloud trapped in the Ioffe-Pritchard trap is compressed adiabatically, resulting in an increase of its temperature. A 1D-Doppler cooling phase allows to increase the phase space density by a factor of 8 and reaches $\chi \approx 7 \cdot 10^{-6}$, similar value than previously in our group before starting the evaporative cooling [58].

2.3.1 Optical molasse

To further decrease the temperature after the MOT phase, the magnetic fields are switched off and the MOT beams are brought close from resonance while reducing their intensity in order to realise an optical molasse.

At the intersect of six counterpropagating beams, red-detuned from the atomic transition by Δ , the slowing force is proportional to velocity, resulting in a viscous damping. In a one dimensional model and for low intensities, insuring that the two light waves of vector $k = 2\pi/\lambda$ act independently on the atoms, the force can be approximated by [68]:

$$F = 4\hbar k \frac{I}{I_{sat}} \frac{kv(2\Delta/\Gamma_0)}{[1 + (2\Delta/\Gamma_0)]^2} = \alpha v \quad (2.10)$$

where $\Gamma_0 = 2\pi \cdot 1.62$ MHz is the linewidth and $I_{sat} = 167 \mu\text{W} \cdot \text{cm}^{-2}$ the saturation intensity of the $2^3S_1 \rightarrow 2^3P_2$ atomic transition. Atoms are not trapped because there is no restoring forces on atoms that have been displaced from the center.

The damping force F leads to a kinetic energy loss rate of $Fv = \alpha v^2$ and thus a typical time-scale of $\tau_{damping} = m/\alpha$, where m is the atomic mass. For He* this corresponds to a typical duration of 10 μs , for $I = 0.5I_{sat}$ and $\Delta = \Gamma_0$.

The average force F damps the atomic velocity but its fluctuations produce heating. At the equilibrium, the heating and cooling rate are equal and the final temperature achieved can be expressed as:

$$k_B T = \frac{\hbar\Gamma_0}{4} \frac{1 + (2\Delta/\Gamma_0)^2}{2\Delta/\Gamma_0} \quad (2.11)$$

With the laser detuning fixed at $\Delta = \Gamma_0$, the achieved temperature should be $T_D = 50 \mu\text{K}$.

The low laser intensity is required here to reduce the effect of stimulated emission: an atom could absorb a photon from one beam and reemit in the counterpropagating beam, resulting in large, velocity-independent changes in the atom's velocity. Typically, 3% of the MOT beams intensity is still deflected by the AOM at this detuning, corresponding to an intensity of $0.5 I_{sat}$ per beam.

Experimentally, after an optical molasse stage of $500 \mu s$ the cloud temperature reaches $T_{molasse} = 300 \mu K$.

Two main technical reasons limit the cloud temperature. First, the magnetic fields are not zero during the short optical molasse stage and therefore not all the atoms are seeing the optimum detuning. For $\Delta = 5 \Gamma_0$, which corresponds to a field of 2 G, the achieved temperature is only $200 \mu K$.

A second reason lies in the retroreflection of the MOT and molasse beams. Indeed optical molasse are highly sensitive to beam imbalance inducing large drift velocities. The imbalance between two counterpropagating beam is here of the order of 5%, due to absorption from the atomic cloud (the absorption can be evaluated to be of the order of 37% at resonance, corresponding to 7% at a detuning $\Delta = \Gamma_0$). Nevertheless the lack of laser power does not allow to produce six independent beams.

The atomic losses occurring during this short duration of the optical molasse are negligible, even if the Penning rate constant is increasing for small detunings of the laser light. The lifetime of the molasse is indeed of the order of 100 ms, so that the losses are at the % level.

Additional compensation coils have been added to match the three dimensional position of the molasse with the magnetic trap center. They produce typically 1 G for 1 A of current to compensate for stray magnetic fields, especially from the second Zeeman slower.

Perfect mode-matching of the MOT and the magnetic trap [69] is not required since a 1D Doppler cooling phase has been implemented, increasing the final phase-space density achieved in the compressed trap. The atomic transfer into the magnetic trap has thus been optimised in order to maximise the atom number and not the phase-space density.

2.3.2 Optical pumping

At the end of the optical molasse stage, atoms are equally distributed between the different Zeeman substates. In order to maximise the trapped atom number, an optical pumping stage drives the atoms in the $m_J = +1$ magnetically trappable state. The optical pumping beam has a circular polarisation (σ^+) and is retro-reflected to form a standing wave along the Z -axis and thus avoid any acceleration effect induced by radiation pressure. Its intensity is typically of $7 I_{sat}$ in total and has been chosen to optimise the atomic transfer into the magnetic trap.

The optical pumping pulse lasts $50 \mu s$ and is shined during the rise of the magnetic fields ($150 \mu s$ after the switch of the current). Its detuning is adjusted experimentally to

match the atomic resonance in presence of the rising field. Since the currents in the coils are rising over $500 \mu\text{s}$, the magnetic field can be considered as constant over the short duration of the optical pumping and defines a proper quantisation axis.

The channeltron positioned in the cell can detect small numbers of trapped atoms after time-of-flight. The channeltron signals recorded with and without optical pumping confirm the expected change by a factor of three for the atom number.

The efficiency of the loading is of the order 50% and typically 10^8 atoms are transferred into the magnetic trap. The cloud is subsequently compressed by reducing the bias field B_0 from 30 G to 12 G, increasing the magnetically trapped cloud temperature to approximately $T_l = 800 \mu\text{K}$.

2.3.3 1D Doppler cooling

Before further compression, another retroreflected σ^+ -polarised beam along the trap axis cooling the sample to about 0.2 mK. For this 1D-Doppler cooling the laser is red-detuned from the atomic resonance frequency in presence of the bias field. As a consequence, atoms will preferentially absorb photons from the beam directed against their direction of propagation and the sample is cooled along the Z -direction. Cooling of the radial degrees of freedom relies on reabsorption of scattered photons and requires thus optically dense clouds [70].

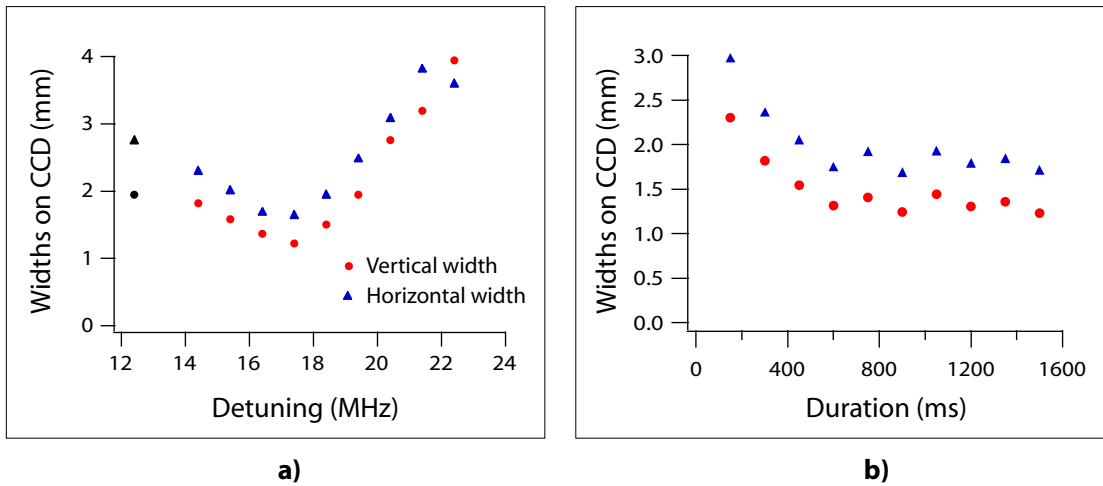


Figure 2.8: a) Scan of the detuning of the Doppler beam from the atomic transition. The horizontal and vertical widths (FWHM on the CCD camera) are obtained from the fit of the imaged cloud after 2 ms time-of-flight. Minimal widths are obtained for $f = 17$ MHz corresponding to a red-detuned beam for $B_0 = 12$ G. The most left black points represent the widths of the cloud without 1D-Doppler cooling stage. b) Scan of the 1D-Doppler duration. The optimum duration is 800 ms with respect to the minimisation of the cloud widths after 2 ms time-of-flight and losses.

This 1D-Doppler cooling stage is realised at a large bias field of 12 G. The different optical transitions are separated by 16.8 MHz, which prevents off-resonant excitations and thus losses due to depumping to non-trapped spin states. The laser frequency is red-detuned from the atomic resonance in an external field of B_0 so that absorption preferentially occurs at the trap minimum where velocity is highest in order to cool efficiently. The intensity has to be small compared to I_{sat} to avoid light-pressure forces due to intensity imbalance between the two counterpropagating cooling beams. Indeed the optically dense atomic sample absorbs almost 40 % of the incident beam intensity.

The Doppler beam has an intensity of the order of $10^{-3} I_{sat}$ and is shined during 800 ms. The detuning is adjusted experimentally in order to maximise the cooling effect as shown in figure 2.8 a). The FWHM widths after 2 ms time-of-flight are measured by optical imaging for different frequencies of the Doppler beam. A clear effect of heating as the laser frequency is blue detuned from the atomic transition can be observed. The duration of the 1D-Doppler stage has also been optimised (see figure 2.8 b)).

This 1D-Doppler cooling stage increases the phase-space density by a factor of 8 without losses. We achieve a final temperature similar to the other groups having implemented 1D-Doppler cooling for magnetically trapped metastable Helium [27, 71, 72, 73]. A determination of the temperature, analysing the time-of-flight signal on the channeltron as in section 1.3.3 is presented in figure 2.9: $T_D = 250 \pm 20 \mu\text{K}$. Because the atomic transition is narrow ($\Gamma_0 = 1.62 \cdot 10^6 \text{ MHz}$) and sensitive to magnetic field (1.4 MHz/G), short time scale fluctuations of B_0 may reduce the efficiency of this method.

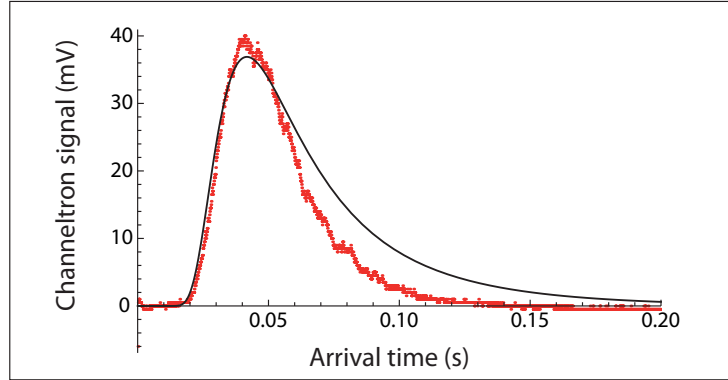


Figure 2.9: *Time-of-flight signal recorded on the channeltron for a Doppler cooled cloud. The experimental data are reported as the red thick line and the fit function from section 1.3.3 is represented as the black plain line. The temperature obtained is: $T_D = 250 \pm 20 \mu\text{K}$. The slowest atoms from the distribution are not properly detected, presumably because of their curved trajectories. An acceptance angle for the detector has been included in the model describing the time-of-flight signal, but the results were critically depending on the chosen cut value and were therefore abandoned.*

2.3.4 Characteristics of the atomic sample in the compressed trap

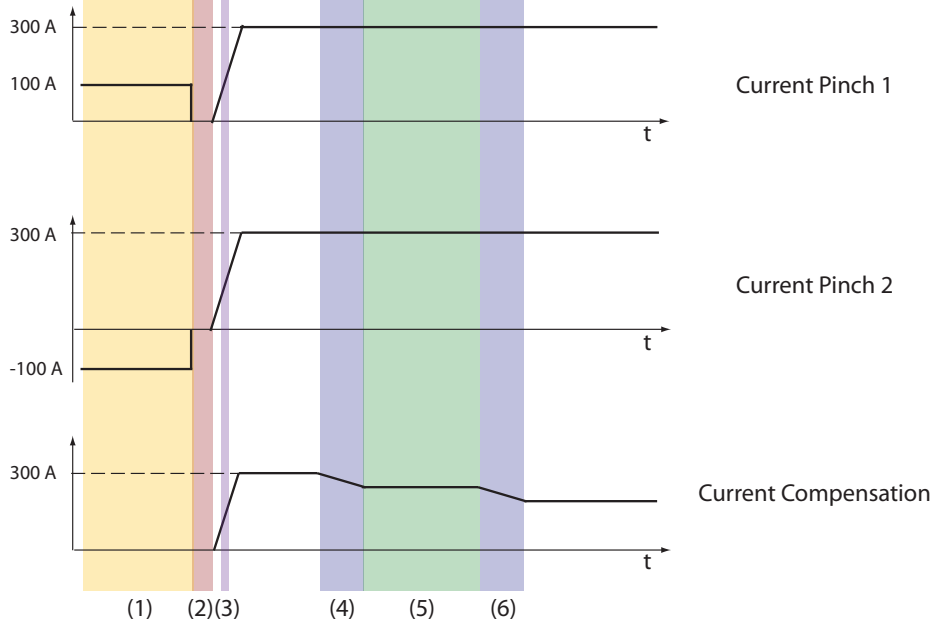


Figure 2.10: *Temporal sequence for the loading of the magnetic trap (not to scale). The current in the pinch and compensation coils are depicted for the different phases of the sequence: (1) MOT phase, (2) Molasse cooling, (3) Spin polarisation, (4) First compression, (5) 1D Doppler cooling, (6) Second compression.*

Further compression to a final bias field $B_0 \approx 1$ G is realised, increasing the central density and ellipticity of the trapped cloud. For an adiabatic transformation, the entropy is conserved and thus the final temperature, higher than the Doppler one, can be evaluated. Let us consider a thermal cloud of N atoms, at a temperature T in a trap of mean frequency ω_{mean} . The fugacity $z = e^{\mu/k_B T}$ can be introduced. The chemical potential μ is related to the total atom number by:

$$N = \left(\frac{k_B T}{\hbar \omega_{mean}} \right)^3 g_3(z), \quad (2.12)$$

where $g_\alpha(z)$ is defined as:

$$g_\alpha(z) = \sum_{p=1}^{\infty} \frac{z^p}{p^\alpha}. \quad (2.13)$$

The entropy of such a thermal gas is equal to [11]:

$$S = k_B N \left(4 \frac{g_4(z)}{g_3(z)} - \log z \right). \quad (2.14)$$

For a starting temperature after 1D Doppler cooling $T_i = 200 \mu\text{K}$ and an initial radial frequency of 70 Hz, the temperature achieved after compression to a typical radial frequency

of 500 Hz is: $T_f \approx 320 \mu\text{K}$.

In order to fulfill the adiabatic requirement, the compression is realised over approximately 1 s, which is long compared to the slowest trapping oscillations of 15 ms. The temperature has been measured to increase to $300 \mu\text{K}$. A more pronounced heating could be observed for durations shorter than 300 ms.

The complete temporal sequence is depicted in figure 2.10. The MOT is loaded during 800 ms, followed by a molasse cooling stage during $300 \mu\text{s}$. The spin polarisation stage covers $50 \mu\text{s}$ during the rise of the magnetic fields, which takes $500 \mu\text{s}$. The compression is done in two stages, separated by a 1D Doppler cooling phase.

The temperature of the atoms has been measured after different holding times in the magnetic trap and over 10 s no heating could be resolved. The final temperature has been measured via absorption imaging of the cloud expansion and via an RF-spectroscopy in the magnetic trap has reported in section 2.4: $T_f = 300 \mu\text{K}$.

The lifetime of the atomic cloud has been measured to be 25 s at $1/e$ as can be seen in figure 5.2, favorable to start evaporative cooling. It is essentially limited by collisions with the background gas. Indeed with a central density of $n_0 = 6 \cdot 10^{10} \text{ cm}^{-3}$, the Penning ionisation in a spin-polarised atomic sample would result in a lifetime of ≈ 100 s and is thus not the limiting factor here.

The effect of the source pressure has been investigated as it impacts on the vacuum of the science cell, but the lifetime remains constant in the range of our working parameters.

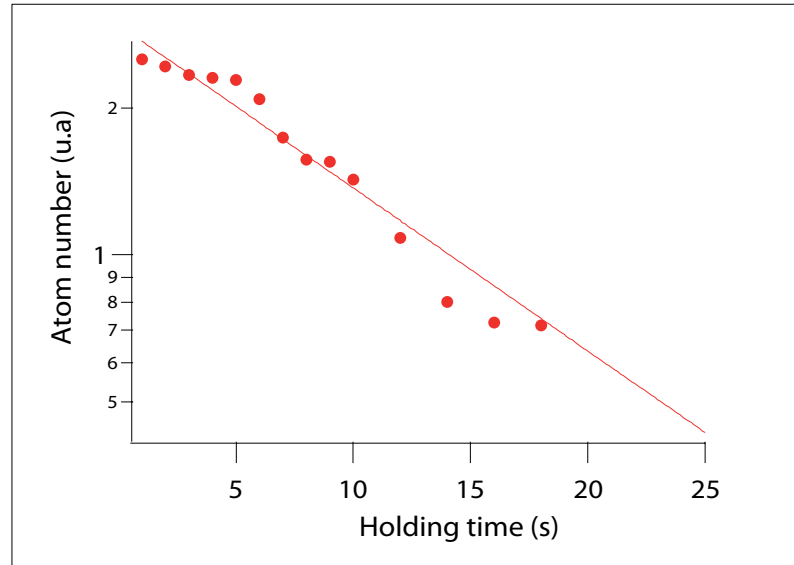


Figure 2.11: *Lifetime of the trapped cloud in a logarithmic scale. The points represents experimental data, averaged over five images, and the plain line a fit of $f(t) = A \exp(-t/\tau)$, with $\tau = 25 \pm 1$ s.*

2.4 Towards evaporative cooling

In the compressed magnetic trap of trapping frequencies $\omega_\rho = 500$ Hz and $\omega_z = 70$ Hz, with 10^8 atoms at a temperature $T_f \approx 300$ μ K, the spatial density at the center is $n_0 = 6 \cdot 10^{10}$ cm^{-3} . The phase-space density χ can be evaluated from:

$$\chi = n_0 \lambda_{dB}^3 = n_0 \left(\frac{h}{\sqrt{2\pi m k_B T_f}} \right)^3 \quad (2.15)$$

where λ_{dB} is the de Broglie wavelength. With the parameters characteristic of the atomic sample in the compressed magnetic trap: $\chi \approx 7 \cdot 10^{-6}$, similar to the starting conditions in [58].

2.4.1 RF spectroscopy

A radio-frequency (RF) spectroscopy of the atomic sample in the Ioffe-Pritchard trap allows to determine two essential parameters: the cloud temperature and the bias field B_0 . We are working with a RF antenna positioned 5 cm away from the atomic cloud along the X axis of the trap. The coil is composed of three turns of dimensions 4×6 cm^2 . The frequency generator (HP-Agilent E4400B) is amplified up to 40 dB by a separated amplifier, corresponding to a maximal power of 15 W.

Radio-frequency waves induce transitions between the trapped spin state $m_J = 1$ to the $m_J = 0$ and $m_J = -1$ states, which are non trapped. For a RF excitation of frequency f_{RF} with 1 W of RF power, it has been experimentally verified that all the atoms with energies above $\epsilon_t = h(f_{RF} - f_0)$ leave the trap within 1 s. The energy hf_0 corresponds to the magnetic potential energy due to the non-zero bias field. Since the gravitational potential energy can be neglected for Helium atoms, this spilling experiment directly probes the Boltzmann energy distribution. The number of atoms outcoupled from the trapping potential by the RF denoted N_{loss} is thus expressed as:

$$N_{loss} = \int_{\epsilon_t}^{\infty} \rho(\epsilon) f(\epsilon) d\epsilon \quad (2.16)$$

where $\rho(\epsilon)$ is the energy density of states and $f(\epsilon)$ represents the Boltzmann distribution defined as:

$$f(\epsilon) = n_0 \lambda_{dB}^3 e^{-\epsilon/k_B T}. \quad (2.17)$$

$n_0 \lambda_{dB}^3$ corresponds to the occupation number of the lowest energy state in the trapping potential.

Assuming an harmonic trapping potential for simplicity (which is not exactly true considering the temperature of the cloud), the energy density of states is proportional to ϵ^2 . Integrating equation 2.16 one can deduce the number of remaining atoms, denoted N_r :

$$N_r = N e^{-\epsilon_t/k_B T} \left(1 + \frac{\epsilon_t}{k_B T} + \frac{1}{2} \left(\frac{\epsilon_t}{k_B T} \right)^2 \right). \quad (2.18)$$

The number of remaining atoms after 1 s of RF excitation was determined by optical imaging for different RF frequencies. Adjusting the experimental data with equation 2.18 enable us to deduce the temperature of the atomic cloud from the data presented in the top of figure 2.12. An independent determination of the temperature from the expansion of the cloud during time-of-flight (absorption imaging) has been realised in the same experimental conditions: before and after the 1D Doppler stage (bottom graphs of figure 2.12). Both measurements are in agreement as one can see from table 2.3.

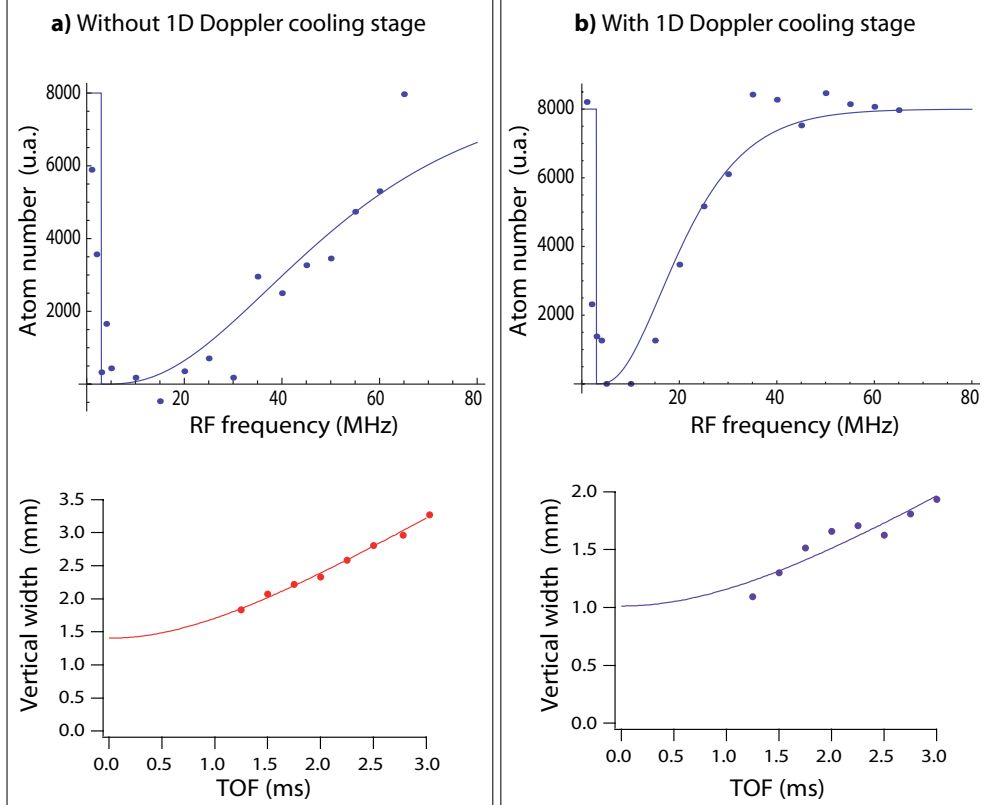


Figure 2.12: *Temperature determination of the atomic cloud in the fully compressed trap, without a) and with b) the 1D Doppler cooling stage. The two top graphs present the experimental data of the RF spectroscopy measurement described in the text: the number of remaining atoms after 1 s of RF excitation at different frequencies has been evaluated with optical imaging and fitted using the function of equation 2.18 with B_0 fixed. The two bottom graphs report the expansion of the vertical width of the atomic cloud, determined by absorption imaging, allowing to deduce the temperature (see Appendix A). The comparison of the temperature obtained by those two independent measurements are reported in table 2.3.*

2.4.2 Evaporative cooling principle

For a cloud at temperature T , in thermal equilibrium in a magnetic trap, the velocity distribution is maxwellian. The evaporative cooling consists in removing the hottest atoms

	From absorption imaging	From RF spectroscopy
Without 1D Doppler cooling	$800 \pm 30 \mu\text{K}$	$800 \pm 100 \mu\text{K}$
With Doppler cooling	$270 \pm 40 \mu\text{K}$	$310 \pm 60 \mu\text{K}$

Table 2.3: *Temperatures determined before and after the 1D Doppler cooling stage by two independent measures: the expansion of the cloud during time-of-flight using absorption imaging and the RF spectroscopy of the magnetically trapped sample.*

from the distribution, having a kinetic energy much larger than $k_B T$. The mean kinetic energy per particle is thus reduced. Subsequently, via elastic collisions the thermal equilibrium can be reached again, with a temperature lower than the initial one.

Evaporative cooling has been first proposed by H. F. Hess in 1986 [74] for spin-polarised Hydrogen and is realised here with RF outcoupling of the hottest atoms [75]. As introduced in the previous paragraph, the frequency f_{RF} determines the minimal kinetic energy $\epsilon_t = h(f_{RF} - f_0)$ of the particles undergoing the transition. If elastic collisions insure thermalisation, the parameter $\eta = \frac{\epsilon_t}{k_B T}$ for a fixed RF frequency increases with time. Simultaneously the probability for an atom of having a kinetic energy larger than ϵ_t decreases and the cooling process becomes slower. To decrease further the temperature, one has to diminish the value of f_{RF} continuously, to force the evaporation. Kinetics is therefore an essential parameter of evaporative cooling.

Three times scales are thus involved in the evaporative cooling process: the thermalisation time, the time scale on which f_{RF} is changed and finally the lifetime of the trapped cloud, denoted $\tau_l \approx 25$ s.

2.4.3 Thermalisation rate

First the thermalisation time has to be short compared to the lifetime of the trapped cloud, meaning that the elastic collision rate Γ_{el} has to be large compared to the inelastic loss rate $\Gamma_{in} = 1/\tau_l$. The critical value of this ratio can be evaluated from a study of the kinetics of the evaporative cooling (in the case where $\eta = \epsilon_t/k_B T$ remains constant during the cooling) [76, 77] and depends only on the geometry of the magnetic potential. In the case of a semi-linear trap, the elastic collision rates increases if $\Gamma_{el} \geq 34\Gamma_{in}$ [76].

In order to evaluate the elastic collision rate in the magnetic trap, before starting the evaporation, a thermalisation experiment has been realised as done in [58]. The atomic cloud is prepared in a non-equilibrium state, by compressing non adiabatically the magnetic potential over 10 ms, increasing the temperature in the radial plane. The time needed for the cloud to reach a final equilibrium state, denoted τ_{therm} , is evaluated from the ellipticity of the cloud as shown in figure 2.13. Just after the compression, the ellipticity remains equal to its value in the starting isotropic potential. After thermalisation, the ellipticity corresponds to the trapping frequency ratio of the compressed trap, which gives $e = 7$. After 1.5 ms time-of-flight, one expects $e = 1.7$ which is larger than the measured value. This discrepancy could result from a wrong theoretical evaluation of the trapping

frequencies.

Since elastic collisions insure the energy exchange between the different degrees of freedom, $\tau_{thermalisation}$ is inversely proportional to Γ_{el} . With a Monte-Carlo simulation, the authors of [78, 79] found, for an harmonic potential, that the number of collisions needed to thermalise is 2.7 ($\tau_{therm} = 2.7 \Gamma_{el}^{-1}$). From the data reported in figure 2.13, $\tau_{therm} = 130$ ms and one can finally deduce: $\Gamma_{el} \approx 21 \text{ s}^{-1}$ and thus $\Gamma_{el}/\Gamma_{in} \approx 540$, which is favorable to start evaporative cooling.

This number of collisions required to thermalise the sample has the right order of magnitude but has been evaluated theoretically under the hypothesis of an harmonic trapping potential and for an initial temperature of $30 \mu\text{K}$. The temperature difference between the initial and final states in fact matters and could change the proportionality factor between τ_{therm} and Γ_{el} .

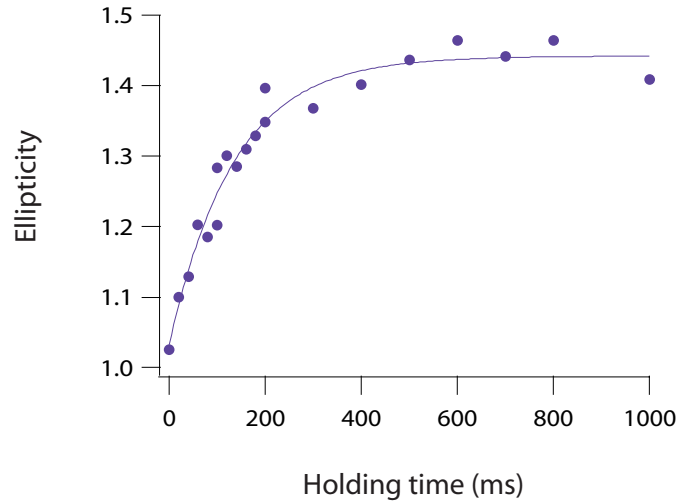


Figure 2.13: *Evolution of the cloud ellipticity (temperature independent) during the rethermalisation in the magnetic trap after a sudden compression. The initial ellipticity is around 1 as expected in an isotropic potential. The final ellipticity is expected to be of the order of 1.7 after 1.5 ms time-of-flight differs from the obtained result. This discrepancy could result from a wrong theoretical evaluation of the trapping frequencies. The plain line represents an exponential fit, from which a thermalisation time can be deduced: $\tau_{therm} = 130 \pm 4$ ms.*

2.4.4 RF ramp for forced evaporative cooling

The study of the kinetics also shows that the parameter η has to be fixed and maintained constant at a value close to 6. For a starting temperature of $400 \mu\text{K}$ and a bias field of the order of 1 G, this corresponds to $f_{RF,start} \approx 40$ MHz. The time-scale at which f_{RF} is varied has to be slow compared to the thermalisation time, but its appropriate value is fixed experimentally. The collision rate should not decrease during the evaporation in

order to reach low temperatures. In an harmonic trap, the elastic collision rate is proportional to the ratio of the atom number N over the temperature T , corresponding to the optical density at the center of the cloud.

The radio-frequency ramp is divided into segments for which the start and end values are fixed and the duration is varied in order to keep a constant optical density at the center. The first segment covers the interval from 40 MHz to 20 MHz and we could observe a division of both the temperature and the atom number by a factor two. As reported in figure 2.14, the optical density at the center remains constant for a RF power of the order of 1 W and the atom number is divided by a factor of two. The temperature has been determined by optical means to be $150 \pm 50 \mu\text{K}$.

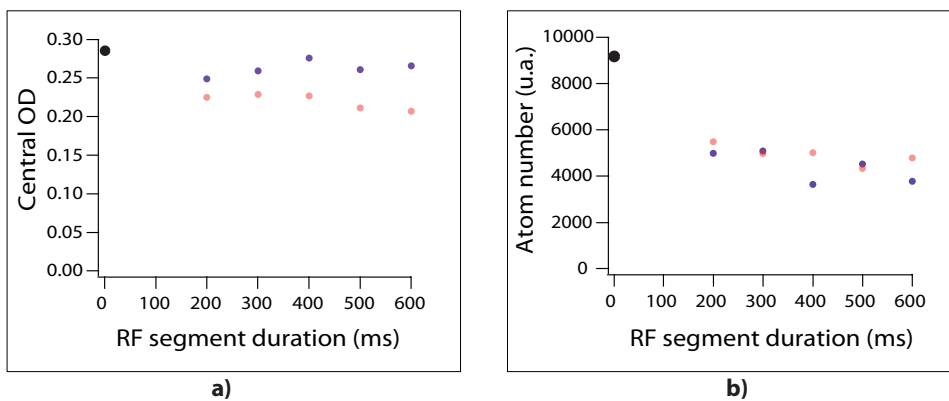


Figure 2.14: Effect of a linear ramp of the RF frequency from 40 MHz to 20 MHz on a) the central density and b) the atom number. The ramp duration is varied between 200 ms and 600 ms. The large black data points correspond to the central density and atom number of the initial atomic cloud. The red (light grey) points corresponds to a power of -15 dB and the lila (black) points to a power of -5 dB, corresponding to a RF power of approximately 1 W.

Reproducible results were until now difficult to obtain, mainly because of the instability of the bias field, fluctuating by 500 mG. Such fluctuations affect mainly the 1D Doppler cooling, changing its efficiency and thus the initial temperature of the evaporative cooling over time because of the narrow linewidth $\Gamma_0 = 1.6$ MHz. An optimisation of the ramp parameters was therefore difficult to realise. Hence, it has been decided to change the relative positions of the coils in order to inject less current in the overcompensating compensation coil: a bias field $B_0 = 1$ G is now achieved for an inverse current of few amperes only, provided by a more stable power supply. We hope to gain in stability and pursue the evaporative cooling process.

2.5 Conclusion

In this chapter the design and the construction of a novel magnetic trap for metastable Helium atoms are presented. This cloverleaf trap configuration allows to load in situ a Bose-Einstein condensate into optical lattices of different dimensionalities.

The performances of the electrical circuit detailed in section 2.2 fulfill the requirements of fast switching of the currents. The typical switching off last 500 μs both for the currents of the MOT quadrupolar field and of the Ioffe Pritchard trap. An additional capacitor permits a fast rising of the current during the switch between the two magnetic field configurations, in order to limit the atomic cloud expansion and thus achieve a higher loading efficiency into the magnetic trap.

Up to 10^8 atoms are loaded into an isotropic magnetic potential, having a trapping frequency of 70 Hz. The loading efficiency can be evaluated to be 50%. Subsequently a 1D Doppler cooling stage increases the phase-space density by a factor of 8, before final compression of the radial frequencies to 500 Hz achieved for a bias field of 1 G. The final phase-space density $\chi \approx 7 \cdot 10^{-6}$ is similar to the one previously obtained in [58]. The lifetime of the trapped atomic sample is limited by collisions with background gases to $\tau_l = 25 \pm 1$ s.

To reach the degeneracy, an evaporative cooling stage has to be implemented. A 'spilling' experiment demonstrates a selective RF outcoupling of the trapped atoms and provides an additional determination of the cloud temperature. In order to start evaporative cooling the ratio of the thermalisation rate Γ_{el} over the inelastic collision rate Γ_{in} has to be larger than 34 (semi-linear magnetic trap) [76]. An experimental determination of Γ_{el} is presented, setting $\Gamma_{el}/\Gamma_{in} \approx 540$. Under those favorable conditions, the first RF frequency ramp to force the evaporative cooling has been optimised to reach a final temperature $T_f = 150 \mu\text{K}$.

Reproducible lower temperatures could not be achieved, mainly because of the instability of the bias field B_0 . The efficiency of the 1D Doppler cooling stage, and thus the phase-space density, depends indeed critically on the value of the bias field. The relative positions of the magnetic trap coils have been changed to improve the bias stability. Less reverse current in the compensation coils is now needed and a more stable power supply is used. Further optimisation of the evaporative cooling is continued.

Chapter 3

Prospects for experiments in an optical dipole trap

For neutral atoms, it has become routine to produce ensembles in the microkelvin region on the basis of three different interactions, each class having specific properties. We have already described the *radiation-pressure traps* [80, 60] resulting from the dissipative force caused by the momentum transfer of absorbed and emitted photons. With near-resonant light the typical depth reaches few kelvins, allowing for the capture of atoms from a vapor or a slow beam. But the attainable temperature is limited by the photon recoil and the density by light-assisted inelastic collisions.

Therefore *magnetic traps* were developed, based on the state dependent force on the magnetic dipole moment in an inhomogeneous field [81, 82]. They represent ideal conservative traps with typical depth of hundreds of mK. A fundamental restriction is then that the trapping mechanism relies on the internal atomic state.

Optical traps rely on the electric dipole interaction with the light field, which is much weaker than all mechanism discussed above. This interaction causes a shift of the atomic energy levels, also called AC-Stark shift. The laser light is usually tuned far away from an atomic resonance frequency, such that spontaneous emission effects from resonant excitations can be neglected and the resulting trapping potential is purely conservative in nature [83].

The rapid development of optical traps since 2000 is a consequence of two main advantages over magnetic ones. First, all spin states can be trapped allowing for more flexibility in the choice of the atomic internal state. Second the magnetic field can be then varied freely. Nowadays Bose Einstein condensate or degenerate Fermi gases are produced without the implementation of a magnetic trap, loading directly the MOT into an optical dipole trap [84, 85].

Those optical potentials and their properties will be presented in the first section (a complete review can be found in [86]). Also the parameters required to implement a crossed dipole trap at $\Lambda = 1560$ nm for metastable helium atoms will be detailed.

To date, experiments involving metastable helium have been largely based upon magnetic trapping that guarantees the spin polarization and thus enables the high density

needed to reach degeneracy. However all-optical potentials formed from far-detuned laser beams present great advantages for novel studies especially of the Penning collisions and were therefore recently implemented by most of the group working with this atom. In such a trap atoms are confined regardless from their spin state, opening the exploration of sample of spin state or mixtures which cannot be controlled in a magnetic trap. This spin degree of freedom has been used to measure spin-state-resolved two-body inelastic loss rate coefficients in [41].

Another new external degree of freedom is the magnetic field: this experimental parameter can now be varied without modifying the trapping conditions. This allows to study the variations of the Penning ionisation rates with the magnetic field value predicted by Schlyapnikov in [22, 23] as detailed in the next chapter.

A new numerical evaluation of the inelastic decay processes in presence of an external magnetic field, using the latest available molecular potentials for metastable helium from [36], will be presented in the second section. The faisability of an experimental test of those theoretical predictions will be discussed.

3.1 Optical trapping potential

In a classical description, optical traps rely on the interaction between an induced dipole moment in an atom and an external electric field. Such a field can, for example, be provided by the oscillating electric light field from a laser, which induces an oscillating dipole moment in the atom while at the same time interacts with this dipole moment in order to create a trapping potential.

3.1.1 Trapping potential

The interaction between atom and light can be described semi-classically using the dipolar Hamiltonian: $H = -\vec{\mu} \cdot \mathbf{E}$, where $\vec{\mu} = -e\mathbf{r}$ represents the electric dipole operator. The perturbation of far-detuned laser light on the atomic levels can be treated according to the second order time-dependent perturbation theory. For non-degenerate states, an interaction described by an hamiltonian H leads to an energy shift of the i th state of unperturbed energy E_i due to non-resonant transitions to final states j :

$$\Delta E_i = \sum_j \frac{|\langle j | H | i \rangle|^2}{E_i - E_j} \quad (3.1)$$

To obtain the non perturbed energies E_i , the dressed state view has to be applied [87, 88]. In its ground state the atom has a zero internal energy and the field energy is $n\hbar\omega$ where n is the photon number and ω the field frequency. When the absorption of a photon promotes the atom in an excited level, the total energy is then the sum of the atomic internal energy $\hbar\omega_0$ and the field energy $(n-1)\hbar\omega$. Thus the denominator in 3.1 becomes $E_i - E_j = \hbar(\omega - \omega_0) = \hbar\Delta_{ij}$, denoting Δ_{ij} the detuning of the laser from the considered atomic transition.

For a two-levels atom the interaction Hamiltonian reduces to $H = -\mu E$, and the energy shift for the ground $|g\rangle$ and excited $|e\rangle$ states respectively:

$$\Delta E = \pm \frac{|\langle e | \mu | g \rangle|^2}{\Delta} |E|^2. \quad (3.2)$$

Introducing the more readable parameters which are the laser intensity $I = 2\epsilon_0 c |E|^2$ and the spontaneous decay rate from the excited level Γ via:

$$\Gamma = \frac{\omega_0^3}{3\pi\epsilon_0 \hbar c^3} |\langle e | \mu | g \rangle|^2 \quad (3.3)$$

one gets the expression of the AC Stark shifts of the energies level of the two level atoms due to far-detuned light:

$$\Delta E = \frac{3\pi c^2}{2\omega_0^3} \frac{\Gamma}{\Delta} I. \quad (3.4)$$

However, for multilevel atoms one has to sum over several excited levels, all involved in the energy shift of the ground state. For a metastable helium atom interacting with laser light at $\Lambda = 1560$ nm, the main atomic transition involved in the shift of the metastable level 2^3S_1 is the cooling transition $2^3S_1 \rightarrow 2^3P$ at $\lambda_0 = 1083$ nm. The other non resonant atomic transitions are too far detuned to contribute in a quantitative way. Moreover, since the laser detuning is very large ($\Delta \approx 10^{14}$ Hz) compared to the typical frequency scale of the fine structure energy levels ($\approx 10^9$ Hz), the latter is not resolved. Therefore the He* atom can be considered as a pure two-level atom coupled via a unique transition, yielding the equation 3.4 as exact.

Equation 3.4 indicates that a spatial variation of the laser intensity creates a spatial variation of the AC Stark shift of the two levels denoted $|g, n\rangle$ and $|e, n-1\rangle$ as depicted in figure 3.1. If one neglects the spontaneous emission, the atomic wave packet will adiabatically follow the spatial variations of either $|g, n\rangle$ or $|e, n-1\rangle$, experiencing an effective potential energy. For a fixed laser detuning Δ , the sign of the dipolar force depends on the internal state of the atom.

Spontaneous emission will change the atomic internal state and thus the sign of the force acting on it. The mean dipolar force acting on an atom is the average of the two opposite forces weighted by the time spent in the ground and excited atomic levels. For far-detuned light, the atom will spend most of the time in the ground internal level and therefore the effective trapping potential is produced by the spatial change in the energy of the dressed state $|g, n\rangle$.

The sign of the detuning will then determine the region of trapping:

- **blue-detuned traps:** above resonance, the dipole interaction repels the atoms from the light maxima. Since several years, experimentalist developed specific methods to trap the atoms at a minimum of the laser light (for example light sheets [89], hollow laser beams [90], evanescent waves [91])

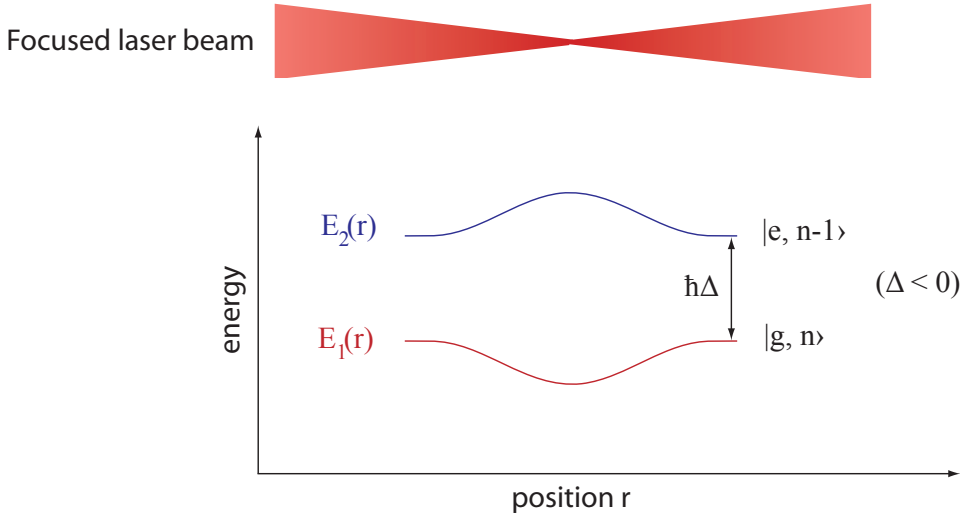


Figure 3.1: Variation of the AC-Stark shifts for a two level atom across a red-detuned focused laser beam.

- **red-detuned traps:** below resonance, atoms are trapped at positions of maximum intensity. In this case, a single focused Gaussian beam constitutes a dipole trap confining the atom in the waist region, where the intensity is maximum.

3.1.2 Scattering losses

The scattering losses can be expressed as [86]:

$$\Gamma_{sc}(\mathbf{r}) = \Pi_e \Gamma = \frac{3\pi c^2}{2\omega_0^3} \left(\frac{\Gamma}{\Delta} \right)^2 I(\mathbf{r}). \quad (3.5)$$

where Π_e is the population in the excited state. From equations 3.4 and 3.5, the advantage of this potential appears: the scattering rate proportional to I/Δ^2 decays faster with the detuning from the atomic transition than the trap depth, which is proportional to I/Δ . One may thus achieve the situation of a non-dissipative potential.

In the case of metastable helium, the depolarisation of the sample due to spontaneous emission is critical because it produces high Penning losses. To reduce Γ_{sc} , a large detuning is necessary and a red-detuning is chosen to produce both a dipole trap and optical lattices as it will be detailed in the two next sections. Among the lasers available, which are red-detuned from $\lambda_0=1083$ nm, lasers at $\Lambda=1560$ nm providing an interesting compromise between the trap depth and the scattering losses have been retained.

3.1.3 Red-detuned crossed dipole trap

In order to create a quasi-isotropic trap, two orthogonal red-detuned Gaussian beams at $\Lambda=1560$ nm intersects at their waist of $w_0=100$ μm .

From equation 3.4, a single focused Gaussian beam propagating along the z axis will create a trapping potential depending on its waist $w(z)$ and power P :

$$U_{dip}(r, z) = \frac{3\pi c^2 \Gamma}{2\omega_0^3 \Delta} \frac{2P}{\pi w(z)^2} e^{-2r^2/w(z)^2} \quad (3.6)$$

where: $w(z) = w_0 \sqrt{1 + (z/z_R)^2}$ and $z_R = \pi w_0^2/\Lambda$ is the Rayleigh length.

The potential depth U_0 created by this single beam at the center can be expressed as:

$$U_0 = \frac{3\pi c^2 \Gamma}{2\omega_0^3 \Delta} \frac{2P}{\pi w_0^2} \quad (3.7)$$

For two crossed beams, propagating respectively along x and y , each of them having a power of 5 W and a waist of 100 μm , the achieved trap depth is 70 μK , corresponding to 35 E_{rec} (defined from the unperturbed energy level). For metastable Helium the recoil energy $E_{rec} = h^2/2\lambda^2 m$ (where $\lambda = 1083$ nm is the wavelength of the atomic transition) is large since the atomic mass m is 20 times smaller than for rubidium. One thus needs to compensate with larger intensities in the dipole trap beams, or smaller waists. The resulting dipolar potential is shown in figure 3.2. This potential can be considered harmonic when the cloud sizes are small compared to the beam waist w_0 and approximated by:

$$U_{dip}(x, y, z) = -2U_0 \left[1 - \left(\frac{x^2 + y^2 + 2z^2}{w_0^2} \right) \right] \quad (3.8)$$

x and y being the propagation axis of the two laser beams. The trapping frequencies are such that:

$$\omega_x = \omega_y = \omega_r = \sqrt{\frac{4U_0}{mw_0^2}} \quad (3.9)$$

$$\omega_z = \sqrt{2}\omega_r \quad (3.10)$$

For our experimental parameters: $\omega_r = 2\pi \cdot 1.2$ kHz and $\omega_z = 2\pi \cdot 1.7$ kHz.

The light source is an Erbium Micro Fiber Module from NP Photonics providing 60 mW of linearly polarised light at $\Lambda = 1560$ nm. The wavelength can be tuned 20 GHz around the central frequency by changing the temperature of two internal gratings. The output power is then splitted to inject two Erbium doped amplifiers (Keopsys) providing 10 W of output power each.

Each of the dipole trap beam will single-pass through acousto-optic modulators (AA Opto-Electronic) with different central frequencies (80 MHz and 110 MHz) in order to produce a differential frequency shift and thus avoid interferences in the trapping volume. These AOMs also enable fast changes in the trap depth, and especially fast switching of the laser beams. The AOMs are made of TeO_2 material and have an active aperture of 33 mm^2 which is specified for a laser beam diameter of 1 to 2.5 mm. This material has been tested to withstand a maximum power intensity of up to 5 $\text{W}\cdot\text{mm}^{-2}$ and can be

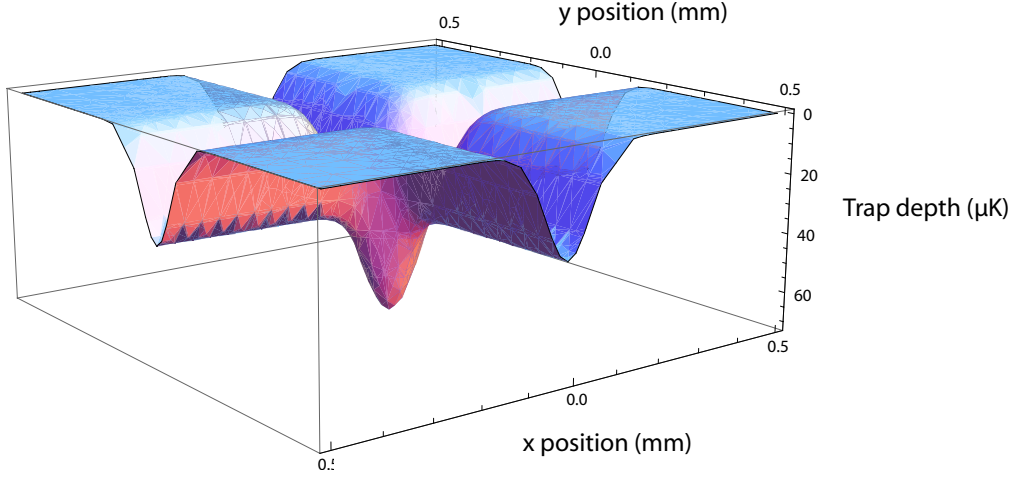


Figure 3.2: *Dipolar potential created by two orthogonal beams having a power of 5 W each and of waist $w_0 = 100 \mu\text{m}$. The trap presents a cylindrical symmetry around the z axis and its depth is then $70 \mu\text{K}$.*

driven with a maximum RF power of 2.2 W with no obvious heating.

At the output of the amplifier fiber, the beam is Gaussian and has a measured waist of $0.59 \pm 0.03 \text{ mm}$. The AOM, placed just after, has a deflection efficiency of 87% and preserves the gaussian profile and the initial waist of the beam. We implemented a telescope to expand the beam using two lenses of respective focal lengths 50 mm and 100 mm. Since a collimated Gaussian beam of waist w and wavelength Λ is focused by a lens of focal length f to a waist w_0 which can be approximated by:

$$w_0 = \frac{f\Lambda}{\pi w} \quad (3.11)$$

one expects to achieve the desired waist w_0 of $100 \mu\text{m}$ with $f = 250 \text{ mm}$.

The final beam waist has been characterised to be $w_0 = 95 \pm 20 \mu\text{m}$ from measurements, using a pinhole, for different distances from the final lens as presented in figure 3.3 a). The Rayleigh length being large ($z_R \approx 1.5 \text{ cm}$) compared to the size of the cold atomic cloud (less than 2 mm), the intensity can be considered to be constant across the sample.

The coil arrangement of the cloverleaf magnetic trap, presented in chapter 2, offers a large optical access and enables to create the dipole trap at the position of the MOT and the magnetic trap center, avoiding the transport of the cold cloud. Different choices for the propagation axis, free from other optical beams, for the two dipole trap beams are possible as shown in figure 3.3 b).

The atomic cloud will be first evaporatively cooled in the magnetic trap to load efficiently the atoms into the crossed dipole trap of depth $70 \mu\text{K}$. An adiabatic loading from

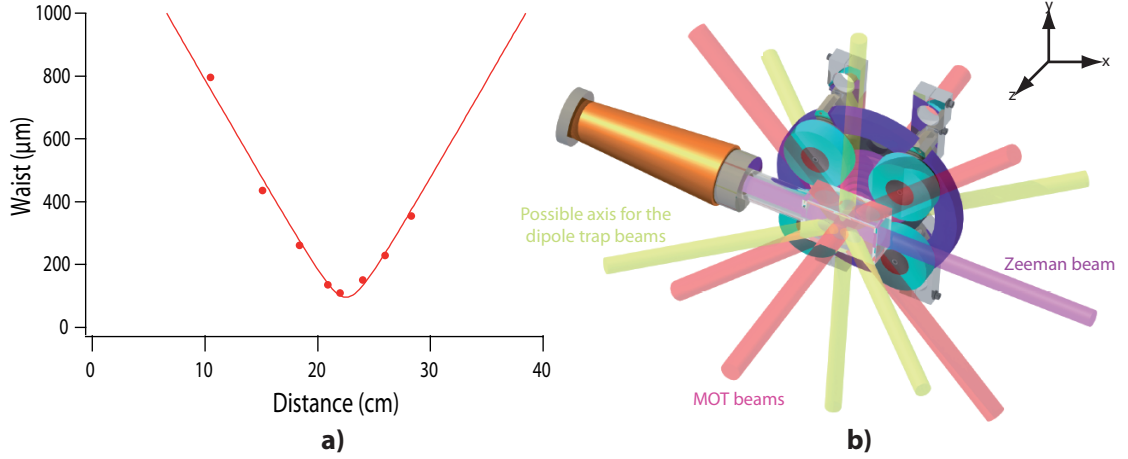


Figure 3.3: a) Measurement of the beam waist for different distances from the final lens. The experimental data have been fitted by the theoretical longitudinal profile of a converging Gaussian beam: $f(z)=w_0\sqrt{1+\left(\frac{z-z_0}{z_R}\right)^2}$, with z_0 , z_R and w_0 as free parameters. One obtains: $w_0=95\pm 20\ \mu\text{m}$, $z_0=22.6\pm 0.2\ \text{cm}$ and $z_R=1.5\pm 0.3\ \text{cm}$. b) Possible axis for the dipole trap beams around the science cell. The propagation axis are the one planned for the lattice beams and are free of other optical beams.

the actual cloverleaf magnetic trap will heat the cloud since the trapping frequencies of the optical trapping potential are larger. The trapping frequencies of the harmonic magnetic potential have been characterised to be: $\omega_{\rho,mag}=2\pi\ 500\ \text{Hz}$ and $\omega_{z,mag}=2\pi\ 70\ \text{Hz}$. Since the entropy is conserved, the initial temperature required in the magnetic trap after evaporative cooling is approximately $15\ \mu\text{K}$, in order to achieve a final temperature of $70\ \mu\text{K}$ in the crossed dipole trap of frequencies: $\omega_{\rho,opt}=2\pi\ 1.2\ \text{kHz}$ and $\omega_{z,mag}=2\pi\ 1.7\ \text{kHz}$.

3.2 Variations of the Penning collision rates with the magnetic field value in a dipole trap

This section is dedicated to the study of the Penning ionisation in a sample of spin-polarised atoms, regime in which they are largely inhibited. Indeed, as explained in section 0.1, the collision rate is reduced by four orders of magnitude allowing to reach the degeneracy for metastable atoms. However those inelastic processes are still occurring due to the spin-dipole interaction, described in 3.2.2, which tends to depolarise the sample. The leading mechanism involves then virtual spin-relaxation transitions in the colliding pair of atoms from the initial $S=2$ quasimolecular state ${}^5\Sigma_g^+$ to the $S=0$ state ${}^1\Sigma_g^+$, which autoionizes through the ordinary Penning mechanism.

To start, a brief review on the different models for the interaction potential in the ${}^5\Sigma_g^+$ electronic state is presented.

After introducing the spin-dipole Hamiltonian and its characteristics, two inelastic collision rates will be defined in order to describe both the depolarisation of the atomic sample and the Penning collisions induced by this depolarisation.

Their theoretical changes in different magnetic field values has been studied in [22, 23]. Here the last *ab initio* molecular potentials for the ${}^5\Sigma_g^+$ electronic state from [36] has been used to numerically evaluate the inelastic collision rates in an external magnetic field at $T = 0$ K.

The last part of this section will focus on the experiment planned to test those theoretical predictions and its faisability.

3.2.1 Different evaluations for the interaction potential in ${}^5\Sigma_g^+$

In this problem, a pair of spin-polarised atoms in the ($2^3S_{1,m_J=1}$) metastable state collide with a low relative energy (typically $T < 70 \mu\text{K}$ for an atomic cloud trapped in the crossed dipole trap). The collision can be studied within the Born-Oppenheimer approximation, which treats separately the position and impulsion variables of the nuclei and the electronic ones. The eigenenergy of each electronic state is determined under the assumption of a fixed inter-nuclear distance r . Subsequently, the movement of the nuclei is described as governed by a potential energy $V(r)$ associated to a particular electronic state. The quantum state of an atomic pair is then the product of a rovibrational state $|\Phi\rangle$ and an electronic state $|\chi\rangle$: $|\Psi\rangle = |\Phi\rangle \otimes |\chi\rangle$.

The electronic state of the atomic pair $|\chi\rangle$ can be written in the basis of the product states of two independent atoms. In the absence of interactions, such product states are eigenstates of the Hamiltonian.

Nevertheless, if the Hamiltonian includes an interaction, those product states are coupled and the new eigenstates, denoted *molecular states*, are linear combinations of different atomic orbitals. The initial state can be described by the following quantum state: $|\mathbf{S} = 2, M_S = 2, l = 0, M_l = 0\rangle$ corresponding to a ${}^5\Sigma_g^+$ electronic state and a zero orbital momentum¹. The spin-dipole Hamiltonian presented in the paragraph 3.2.2 couples the

¹In this notations S represents the total spin of the atomic pair l its total orbital momentum ; M_S and M_l corresponds to their respective projections on the quantisation axis.

initial $^5\Sigma_g^+$ electronic state with zero orbital momentum to different final states among which the ($^1\Sigma_g^+$, $l=2$) state, from which Penning ionisation is allowed.

The theoretical description of such collisions relies on the chosen modelisation of the interaction potential $V_q(r)$. It consists of two distinct parts: a repulsive short range part and an attractive long range one.

The repulsive short range part of this potential is due to the exchange interaction, resulting from the overlap of the electronic wave functions of the two atoms. The size of an electronic cloud of a metastable helium atom is of the order of $3 a_0$ (mean value of the size of an hydrogen atom in the electronic state ($n=2, l=0$)) and therefore $6 a_0$ corresponds to a 'rough' range of the interaction responsible for the repulsive part of the potential. The minimum of the different potentials lies indeed at $r_{min} = 7.3 a_0$ as can be seen in figure 3.4.

At large distance, the interaction is attractive due to the electrostatic interaction of the charge distributions of the two neutral atoms. The lowest order in $1/r$ corresponds to the dipole-dipole interaction ($1/r^3$), which can be treated perturbatively. As the atoms are in a S state, the first order of the perturbative treatment contains only terms proportional to the zero matrix element $\langle L=0 | \hat{D} | L=0 \rangle$, where \hat{D} is the electric dipole operator. The order two of the perturbation is then proportional to $1/r^6$, when the retardation effect due to the finite speed of light is neglected [92]. As a consequence, this attractive long range part of the potential is modeled by a term written as C_6/r^6 . Higher order terms due to the electric quadrupole and octopole are also taken into account via coefficients denoted C_8 and C_{10} .

Those long range coefficients can be determined from a method, considered as exact, where the polarisability of the electric dipole, quadrupole and octopole, together with the coupled dispersive coefficients, are calculated from the wave functions composed from an ensemble of basis variationally determined [93]. Those dispersive coefficients correct the various terms of the expansion for charge overlap effects, via a damped incomplete Gamma function.

The first potential, which was accurate enough to predict the proper number of bound states, has been proposed by J. Starck and W. Meyer in [94]. This article presents the advantage of providing an analytical expression of the potential. However, the long range part of this potential is inexact (the C_6 , C_8 and C_{10} coefficients are not in agreement with the one determined in [93]) and no error bar has been provided. This potential is the one used in the evaluation of the variations of the inelastic collision rates with the magnetic field value in [22, 23].

Another potential has been proposed in [95] and [96] based on *ab initio* calculations for interatomic distances smaller than $18 a_0$ and on perturbative calculations for the long range part. The main difficulty lies in the interpolation of those two parts of the potential. Depending on the position of the transition between short range and long range interactions, the resulting position of the last bound state and thus the scattering length varies.

The latest theoretical evaluation of this potential has been realised by M. Przybytek and B. Jeziorski in [36]. It is based on the Born-Oppenheimer potential adding adiabatic,

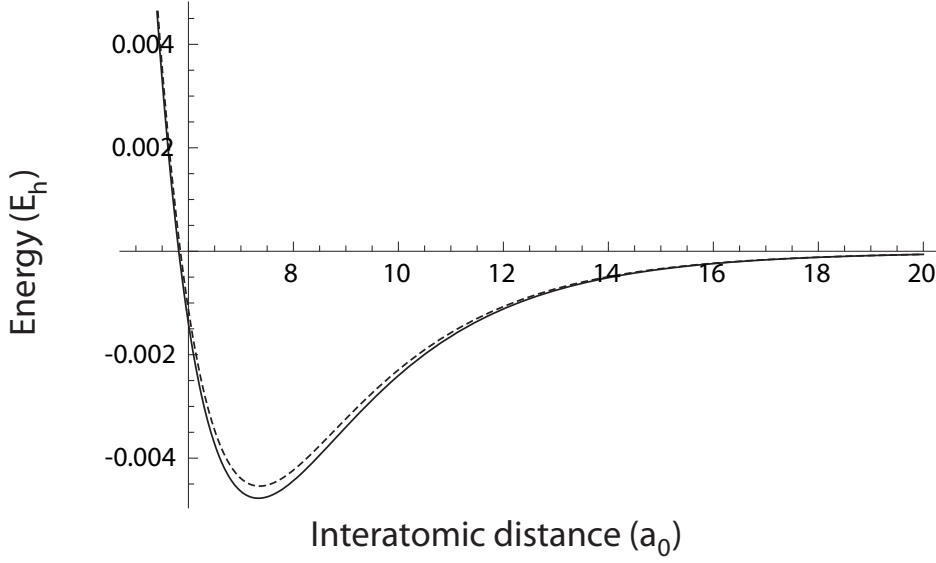


Figure 3.4: Potential energy curves V_q for the ${}^5\Sigma_g^+$ electronic state as a function of the interatomic distance in Bohr radius a_0 . The energy are expressed in atomic units. The dashed line corresponds to the potential obtained by J. Starck and W. Meyer [94] and used in the evaluation of the magnetic field dependency in [22, 23]. The plain line represents the potential derived by M. Przybytek and B. Jeziorski in [36].

relativistic and QED corrections. They provide an analytical expression of the potential valid for any interatomic distance. The error bar results from the weight of the different corrections (estimated at $\pm 10\%$ for adiabatic corrections and $\pm 20\%$ for relativist and QED corrections) as well as the choice of the mass (atomic or nuclear) of Helium in the Schrödinger equation. The scattering length of $a = 7.64 \pm 0.2$ nm determined from this potential is in remarkable agreement with the experimental results obtained in our group [38].

As can be seen in figure 3.4, the two models from [94] and [36] differ by up to 10% at the position of the potential minimum. This will lead to notable changes in the evaluation of the inelastic scattering rates as detailed in paragraph 3.2.4.

3.2.2 Spin-dipole Hamiltonian

The spin-dipole Hamiltonian describes the interaction between the magnetic dipoles \mathbf{M}_1 and \mathbf{M}_2 of two helium atoms (see figure 3.5). The magnetic momenta are related to the atomic spin via $\mathbf{M}_i = g_S \mu_B \mathbf{S}_i$, with $g_S = 2$ the Lande factor for the state 2^3S_1 and $\mu_B = e\hbar/2m_e$ the Bohr magneton expressed as a function of the electron charge e and mass m_e . This Hamiltonian expresses the interaction energy of the dipole momentum \mathbf{M}_2 with the magnetic field created by \mathbf{M}_1 . Denoting as \mathbf{r} the interatomic vector, this long-range interaction Hamiltonian can be written as (see [97], Appendix B_{XI}):

$$H_{sd}(\mathbf{r}) = -\frac{\mu_0 (g_S \mu_B)^2}{4\pi r^5} (3(\mathbf{S}_1 \cdot \mathbf{r})(\mathbf{S}_2 \cdot \mathbf{r}) - (\mathbf{S}_1 \cdot \mathbf{S}_2)r^2). \quad (3.12)$$

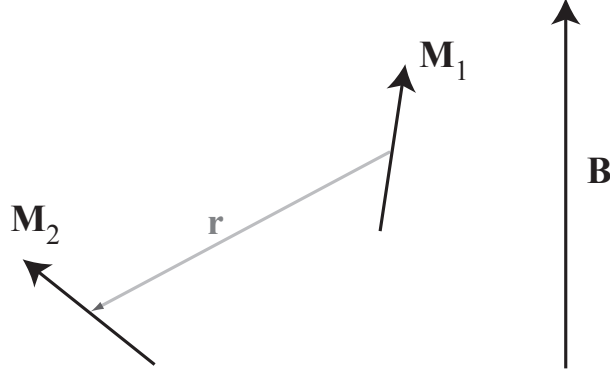


Figure 3.5: *Relative disposition of two magnetic dipoles. The magnetic operators are usually expressed in a basis linked to the experimental magnetic field \mathbf{B} , defining the quantum axis. On the contrary, the kinetic momentum related to the atomic rotation is naturally expressed in a basis linked to \mathbf{r} , colinear to the molecule axis.*

The action of this Hamiltonian has now to be expressed in the basis of the electronic states $|S(S_1S_2)M_S\rangle$ using the total electronic spin $\mathbf{S} = \mathbf{S}_1 + \mathbf{S}_2$ of projection M_S along the laboratory quantification axis, and in the basis of the spherical harmonics $|lM_l\rangle$. Different spin states but also different spherical harmonics will be coupled as the spin-dipole coupling is anisotropic. Only the total angular momentum $\mathbf{J} = \mathbf{S} + \mathbf{l}$ is conserved. The details for this decomposition can be found in [98] and finally the initial state $|S = 2, M_S = 2, l = 0, M_l = 0\rangle$ is coupled to the three final states:

$$\begin{aligned} &|S = 2, M_S = 1, l = 2, M_l = 1\rangle \\ &|S = 2, M_S = 0, l = 2, M_l = 2\rangle \\ &|S = 0, M_S = 0, l = 2, M_l = 2\rangle \end{aligned} \quad (3.13)$$

with spin-dipole Hamiltonian matrix elements equal to:

$$\langle 2, 2; 0, 0 | H_{sd} | 2, 1; 2, 1 \rangle = -\sqrt{\frac{6}{5}} \frac{\beta}{r^3} \quad (3.14)$$

$$\langle 2, 2; 0, 0 | H_{sd} | 2, 0; 2, 2 \rangle = -\frac{2}{\sqrt{5}} \frac{\beta}{r^3} \quad (3.15)$$

$$\langle 2, 2; 0, 0 | H_{sd} | 0, 0; 2, 2 \rangle = -\sqrt{\frac{2}{5}} \frac{\beta}{r^3} \quad (3.16)$$

with $\beta = \frac{\mu_0}{4\pi} (g_S \mu_B)^2$. This expression is different from [22, 23] where cgs units are used and the integration is done only on the spin variables.

3.2.3 Inelastic collision rates

In the case of transitions where $S_f = S_i = 2$, the final states of the scattering process can not lead to Penning ionisation since the atoms remains in the electronic state $^5\Sigma_g^+$. The scattered part of the wavefunction in the state $|S = 2, M_S, l = 2, M_l = 2 - M_S\rangle$ will propagate

in an effective potential:

$$V_{eff}^{S=2, M_{S_f}} = V_q(r) + \frac{l(l+1)}{2\mu r^2} - E_m(M_{S_f}) \quad (3.17)$$

where $l=2$ is the final orbital momentum and $E_m(M_S) = 2\mu_B B(2 - M_S)$ the final magnetic energy of the atomic pair.

In the case of $S_f=0$, an autoionisation process may happen since the atoms are no longer spin-polarised. As Penning ionisation occur with probability close to unity at inter-particle distance smaller than $7a_0$ [99], the interatomic potential is modeled by a perfectly absorbing boundary at a distance $r_0 = 7a_0$ and, at larger r , by the purely elastic potential $^1\Sigma_g^+$, denoted $V_s(r)$ and taken from [99]. The effective potential is in this case:

$$V_{eff}^{S=0, M_{S_f}=0} = V_s(r) + \frac{l(l+1)}{2\mu r^2} - E_m(0) \quad (3.18)$$

where again $l=2$ is the final orbital momentum.

The collision between two spin-polarised metastable atoms is thus fully described by the following coupled Schrödinger equations:

$$\left(-\frac{\hbar^2}{2\mu} \Delta + V_q(r) \right) y_{l=0}^q(r) = -\sqrt{\frac{6}{5}} \frac{\beta}{r^3} y_{l=2, m_l=1}^q(r) - \frac{2}{\sqrt{5}} \frac{\beta}{r^3} y_{l=2, m_l=2}^q(r) - \sqrt{\frac{2}{5}} \frac{\beta}{r^3} y_{l=2, m_l=2}^s(r) \quad (3.19)$$

$$\left(-\frac{\hbar^2}{2\mu} \Delta + V_q(r) + \frac{l(l+1)}{2\mu r^2} - E_m(1) \right) y_{l=2, m_l=1}^q(r) = -\sqrt{\frac{6}{5}} \frac{\beta}{r^3} y_{l=0}^q(r) \quad (3.20)$$

$$\left(-\frac{\hbar^2}{2\mu} \Delta + V_q(r) + \frac{l(l+1)}{2\mu r^2} - E_m(0) \right) y_{l=2, m_l=2}^q(r) = -\frac{2}{\sqrt{5}} \frac{\beta}{r^3} y_{l=0}^q(r) \quad (3.21)$$

$$\left(-\frac{\hbar^2}{2\mu} \Delta + V_s(r) + \frac{l(l+1)}{2\mu r^2} - E_m(0) \right) y_{l=2, m_l=2}^s(r) = -\sqrt{\frac{2}{5}} \frac{\beta}{r^3} y_{l=0}^q(r) \quad (3.22)$$

Transitions to different final electronic states are then characterised by the radial flux scattered for $r \rightarrow \infty$ in the different final states $|\mathbf{S} = 2, M_S = 1, l = 2, M_l = 1\rangle$, $|\mathbf{S} = 2, M_S = 0, l = 2, M_l = 0\rangle$ and $|\mathbf{S} = 0, M_S = 0, l = 2, M_l = 2\rangle$, which is called spin-relaxation rate and denoted α_{rel} . Using the formalism introduced in Appendix ??:

$$\alpha_{rel} = \frac{2\pi\hbar}{k\mu} \left(|S_{2,2;0,0}^{2,0;2,0}|^2 + |S_{2,2;0,0}^{2,1;2,1}|^2 \right) \quad (3.23)$$

where $S_{2,2;0,0}^{2,0;2,0}$ and $S_{2,2;0,0}^{2,1;2,1}$ are the S matrix elements for the corresponding transitions.

The radial flux of the wavefunction of the final state $|\mathbf{S} = 0, M_S = 0, l = 2, M_l = 2\rangle$ onto the absorbing boundary at $r = r_0$ corresponds the spin-relaxation induced ionization rate, denoted α_{ri} . Indeed an atomic pair in the $^1\Sigma_g^+$ electronic state, will Penning ionise if their internuclear distance becomes smaller than r_0 .

It is important to notice that those inelastic collision rates correspond to different limits for the interparticle distances, describing respectively the depolarisation of the initial

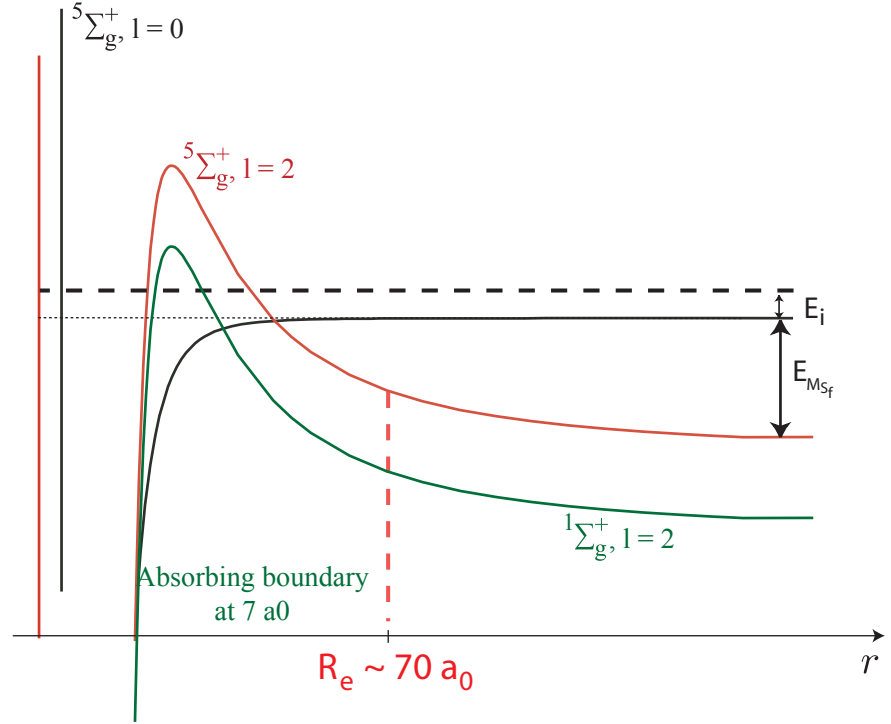


Figure 3.6: Interaction potentials (${}^5\Sigma_g^+, l=0$) for the initial state, (${}^5\Sigma_g^+, l=2$) and (${}^1\Sigma_g^+, l=2$) for the different final states as a function of the interatomic distance expressed in Bohr radius. The quintet and singlet potentials are coupled by the spin-dipole Hamiltonian and separated by the Zeeman energy $E_{M_{S_f}} = 2g_S\mu_B B$. E_i is the initial energy of the two colliding spin-polarised metastable helium atoms. $r_0 = 7a_0$ is the distance at which the absorbing boundary is set on the potential (${}^1\Sigma_g^+, l=2$) to describe Penning ionisation losses.

sample and the Penning ionisation losses occurring only at short interparticular distances.

The initial and final interaction potentials involved are represented in figure 3.6 as a function of the interparticular distance r . Any variation of the magnetic field value will change their relative positions and therefore modify the inelastic collision rates α_{rel} and α_{ri} .

3.2.4 Discussion of the theoretical evaluation

To obtain the magnetic field dependency of the collision rates, those coupled Schrödinger equations have been solved for each value of the field, affecting the relative position of the electronic potential via $E_m(M_{S_f})$, with an exact numerical method described in Appendix ???. The results obtained are reported in figure 4.3, together with the evaluation from [22, 23].

In low magnetic fields ($B < 100$ G) relaxation-induced ionisation is field independent

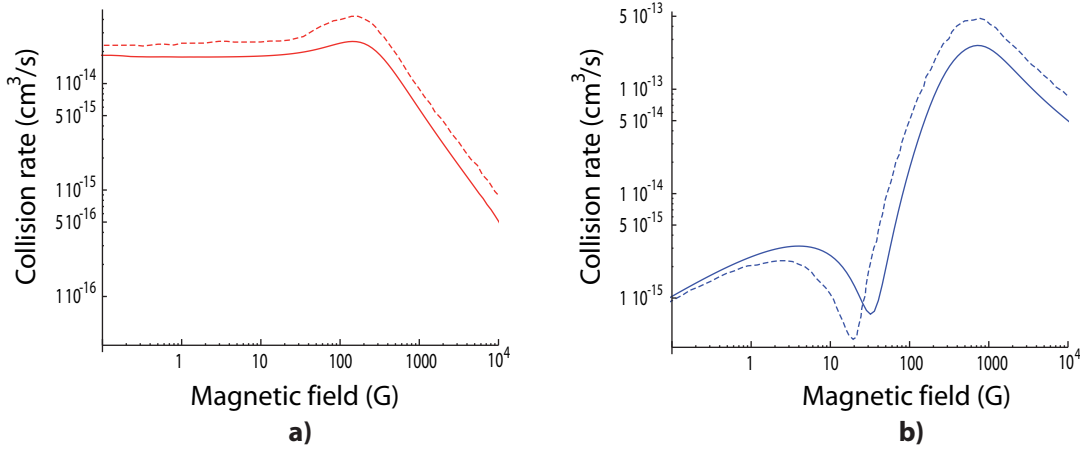


Figure 3.7: Variation of the two inelastic rate constants with the magnetic field (logarithmic scales). In both graphs, the plain line represent the present evaluation and the dashed line the result from [22, 23]. a) Variations of the spin-relaxation induced ionisation α_{ri} with the magnetic field, radial flux in the scattered wave ($|\mathbf{S} = 0, M_S = 0, l = 2, M_l = 2\rangle$) for $r = R_0$ (position of the absorbing boundary to describe the Penning ionisation) in a) and of the spin-relaxation α_{rel} , radial flux in the scattered waves for $r \rightarrow \infty$ in b).

with a rate constant of $\alpha_{ri} \approx 2.10^{-14} \text{cm}^3 \cdot \text{s}^{-1}$, and is the main two-body decay channel of the spin polarized helium gas. In higher fields, α_{ri} decreases and spin relaxation, which is strongly field dependent, produces the main losses from the cloud. The rate constant α_{rel} reduces in higher magnetic field but never drops below the low-field value of the relaxation-induced ionisation. Therefore low fields are better to form and study metastable helium Bose-Einstein condensates.

To get an intuition of the typical distance at which the interaction occurs, the energy conservation in the quintet potential can be expressed:

$$E_T = \frac{\hbar^2 l(l+1)}{mR_{int}^2} - E_m(M_{S_f}) \quad (3.24)$$

where E_T is the thermal energy of the initial particles (neglected here). In the regime of low fields where $E_m \ll E_T$ the interaction occurs at distance such that $R_{int} \approx 1/k_T$. For larger fields: $R_{int} \approx 1/k_f$, where k_f is due to the magnetic energy. The larger the value of the magnetic field, the smaller this interaction radius becomes.

Concerning the spin-relaxation rate, one may notice a strong cancellation at magnetic fields of the order of 60 G, for which $R_{int} \approx 1/k_f \approx a$. This can be interpreted in the framework of the first order approximation adopted in [22, 23]. The spin-relaxation rate is proportional to:

$$\alpha_{S,M} \propto \left| \int_0^\infty \chi_{2,l_i}(k_i, R) \chi_{S,l_f}(k_f, R) \frac{dR}{R^3} \right|^2 \quad (3.25)$$

where the function $\chi_{S,l}$ describes l elastic scattering in the potential U_S . From the selection rules of the spin-dipole Hamiltonian: $l_i = 0$ and $l_f = 2$.

At large distance $\chi_{2,0}$ can be approximated by the s – $wave$ scattering function proportional to $(1-a_s/R)$, leading to a strong cancellation in the integral 3.25. As a consequence, the position of the dip in the spin-relaxation rate α_{rel} is a measure of the scattering length a_s of metastable Helium. From the potentials evaluated in [22, 23], one can deduce $a_s = 167.7 a_0$. The value extracted from the new evaluation is $a_s = 141.9 a_0$, which is in agreement with the last experimental measurement of this quantity [38].

Effect of the interaction potential: As can be seen in figure 4.3, this evaluation is strongly dependant from the modelisation of the interatomic potential in the electronic state $^5\Sigma_g^+$. Measuring those collisions rates may therefore improve our knowledge on the short range part of this potential. Since the long range part of the potential is well determined, simulations have been realised by multiplying the short range part of the potential either by 1.01 or 0.99 and the resulting curves are presented in figure 3.8.

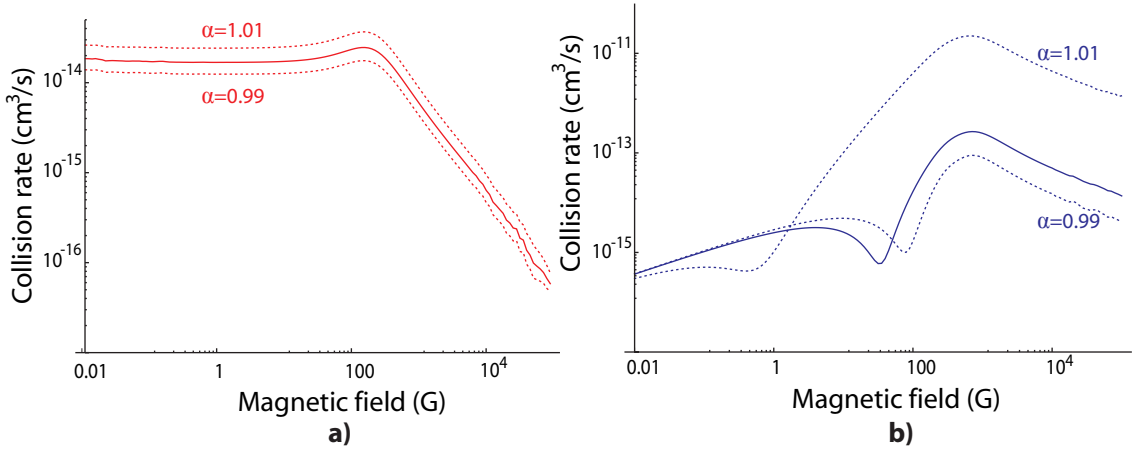


Figure 3.8: *Effect of a multiplication of the short range part of the potential by either 1.01 or 0.99. in both graphs, the plain line represents the actual evaluation. a) α_{ri} is larger for a multiplication of the short range part of the potential by a factor 1.01. b) The variations of α_{rel} with the magnetic field and especially the position of the dip are strongly modified by a change of 1% in the short range part of the potential.*

Effect of the temperature: This evaluation is restricted to the zero temperature case but the influence of temperature has been investigated in [23]. Relaxation-induced ionisation conserves the same behaviour with the magnetic field, but has higher collision rate for lower temperature: 30% changes are expected between 0 K and 1 mK. The spin-relaxation rate is more temperature sensitive and the strong dip at 40 G cancels for larger temperature.

3.2.5 Experimental measurement of the inelastic rates

The experimental determination of those inelastic collision rates for different magnetic fields may improve our knowledge about the interaction potential $V_q(r)$ in the $^5\Sigma_g^+$ elec-

tronic state.

Assuming the ultracold sample of spin-polarised atoms is trapped in the crossed dipole trap, it is now possible to perform a measurement of the relaxation rates presented above as a function of the magnetic field. The coils will produce a constant magnetic field up to 500 G. In order to distinguish the two loss mechanisms, the channeltron located in the quartz cell will be used as a complementary detection method from the usual absorption imaging.

The channeltron, polarised by -3 kV, will attract and detect each ion produced during Penning ionisation events. Therefore the relaxation-induced ionisation rate α_{ri} will be directly recorded by the channeltron. As one can see from figure 4.3, α_{ri} is ranging from $2 \cdot 10^{-14} \text{ cm}^3 \cdot \text{s}^{-1}$ for $B < 100 \text{ G}$, to $1 \cdot 10^{-15} \text{ cm}^3 \cdot \text{s}^{-1}$ for $B = 500 \text{ G}$. For a cold cloud with 10^6 atoms and sizes of $100 \times 10 \times 10 \text{ } \mu\text{m}^3$, this corresponds to a change from 0.13 to 0.013 Penning ionisation per second. The single-ion detection efficiency will enable a very accurate determination of this loss rate.

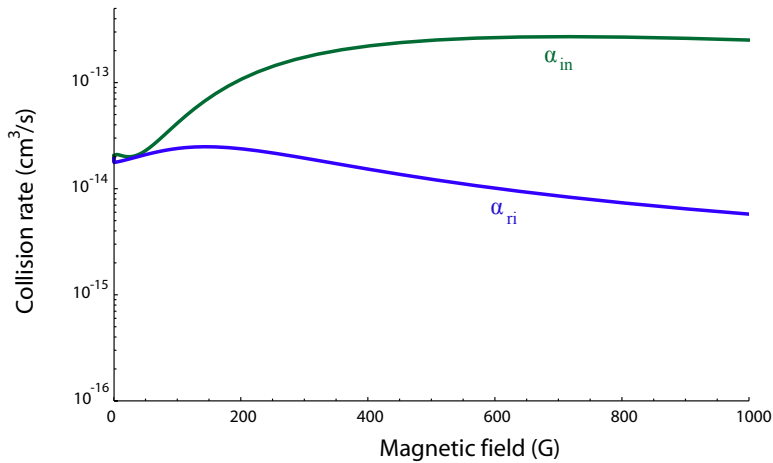


Figure 3.9: Variation of the measurable inelastic collision rates with the magnetic field. The relaxation-induced ionisation rate α_{ri} will be deduced from the channeltron signal. The total atomic losses evaluated via absorption imaging are due to the contribution of the two inelastic loss channels and characterise $\alpha_{in} = \alpha_{ri} + \alpha_{rel}$. The coils will produce a magnetic field up to 500 G.

The spin relaxation rate α_{rel} can also be observed experimentally, although not in a direct way. During a spin-dipole transition, the change of Zeeman energy is given by $E_{M_{S_f}} = 2\mu_B B(2 - M_{S_f})$, which is minimum for $M_{S_f} = 1$ with $E_1 \approx 130 \text{ } \mu\text{K} \cdot \text{G}^{-1}$. Consequently, for magnetic field larger than 1 G, the final states of a spin-dipole will acquire sufficient kinetic energy to escape from the optical trap. The measurement the total atom losses via an absorption imaging technique, characterises the sum of the two inelastic collision rates α_{ri} and α_{rel} , whose variation with the magnetic field is depicted in figure 3.9. Finally the spin-relaxation rate will be deduced from $\alpha_{rel} = \alpha_{in} - \alpha_{ri}$, but will be limited by the accuracy of the measurement of α_{in} . Indeed the atom number

3.2. VARIATIONS OF THE PENNING COLLISION RATES WITH THE MAGNETIC FIELD VALUE

determination may be too unaccurate to obtain low values α_{rel} for $B < 100$ G.

3.3 Conclusion

The first section of this chapter presented the characteristics of the crossed optical dipole trap, which will be implemented on the experimental setup. This optical trap, releasing the constraint on trapped spin states and on magnetic field, opens novel studies on the properties of the inelastic collision rates of $^4\text{He}^*$. A single beam dipole trap, implemented in the group from Institut d'Optique (Palaiseau), has allowed a recent measurement of spin-state-resolved Penning inelastic rate coefficients [41].

An exact numerical evaluation of the spin-relaxation and spin-relaxation induced ionisation rates in different magnetic fields has been presented. The scattering length a_s , deduced from the cancellation of the spin-relaxation, shows a good agreement with the experimental result obtained in a previous work [38].

The new detection device implemented recently constitute a key element for the experimental measurement of the spin-relaxation and spin-relaxation induced ionisation rates. The core of this measurement is indeed the ability to distinguish between losses due to Penning ionisation, producing a signal on the channeltron, from the others. The complementary diagnosis of absorption imaging will provide a complete determination of those inelastic rates.

One could also take advantage of this channeltron to verify whether the limiting process for the lifetime of a dimer of metastable Helium $^4\text{He}_2^*$ is the autoionisation Penning induced by spin relaxation. This assumption indeed leads to a theoretical evaluation of $\approx 120 \mu\text{s}$ lifetime [40], two orders of magnitude larger than the measured value of $1.4 \pm 0.3 \mu\text{s}$ [39].

Chapter 4

Metastable Helium in optical lattices

Taking advantage of the dipolar interaction presented in chapter 3, periodic potentials can be formed simply by overlapping two counter-propagating laser beams. The interference between the two laser beams forms an optical standing wave with period $\lambda/2$, which can trap the atoms. By interfering more laser beams, one can obtain one-, two- and three-dimensional periodic potentials. The implementation of the novel cloverleaf magnetic trap, presented in chapter 2, constitutes an essential step towards a new generation of experiments involving such optical lattices.

Storing ultracold quantum gases in those artificial periodic potentials of light has opened innovative manipulation and control possibilities. Indeed, the geometry and depth of the potential are under the complete control of the experimentalist. The inelastic Penning collisions occurring in metastable Helium present intriguing additional features over other atomic species.

Collisional properties of ultracold gases strongly confined in one or two directions attract a great deal of interest since low-dimensional geometry can be experimentally achieved using optical lattices. It is well established that confinement of a gas can strongly modify both the elastic and inelastic collision rates as established in 1D [43, 44] and 2D [45, 46].

Confinement-induced resonances (CIR) [51], occurring in such regimes, have been recently experimentally observed. The investigation of mixed-scattering occurring when the collisional partners are confined in different dimensions (3D and 2D in this case) have revealed mixed-dimensional resonances [52].

The first section is thus dedicated to a prospective study of the modification of the inelastic Penning collision rates induced by a quasi-2D geometry in a deep 1D optical lattice.

The second section focuses on the description of metastable Helium atoms stored in a 3D optical lattice. To account for the dissipation induced by Penning ionisation events, the Bose-Hubbard model has to be modified. Dissipative Bose-Hubbard models have already been investigated both theoretically and experimentally [56, 100, 55]. The effect of the dissipation will be described in the frame of a three-level model both in the limit of weak losses (polarised sample of $^4\text{He}^*$) and of strong losses (non-polarised sample of $^4\text{He}^*$). In the later case, a strongly correlated quantum system can be reached, in which tunneling is suppressed. Large two-body losses thus result in a stabilisation of the system,

suppressing double occupancy of lattice sites and as a consequence the losses.

4.1 1D optical lattices: collisional properties in confined dimensions

Confining He* atoms in a 1D optical lattice at $\Lambda=1560$ nm makes it possible to study the modification of the inelastic collision rate induced by a tight axial confinement. The deep confinement achieved allows to enter the quasi-2D collisional regime as defined in [45, 46]. This regime presents peculiar features, which will be recalled in this section.

The idea is to freeze the motion along one dimension, taking advantage of a tight harmonic trapping of frequency ω_z . Working at temperatures lower than the energy spacing of the axial harmonic oscillator of frequency ω_z , forces the atomic wave-function into the ground-state of this oscillator. From a thermodynamic point of view, the gas is thus considered to be 2D if $k_B T \ll \hbar\omega_z$.

However this criterion does not determine if two-body collisions can be regarded as two-dimensional. Concerning collision, the relevant quantities are the extension of the wave function in the axial direction $l_z = \sqrt{\hbar/m\omega_z}$ and the scattering length a_s . This section presents an evaluation of the modification of the inelastic Penning collision rate induced by the confinement, in a strongly confined regime where $l_z=4.3 a_s$. Such regimes, in which l_z becomes comparable to a_s , have not been accessed experimentally except for a two-component Fermi gas [101].

4.1.1 The confining potential, a 1D optical lattice

A red detuned Gaussian standing wave along z creates several traps, spaced by $d = \Lambda/2$, with a high confinement along the laser direction according to:

$$U_{1D}(r, z) = 4U_0 \cos^2\left(\frac{2\pi z}{\Lambda}\right) \exp\left(-\frac{2r^2}{w_0^2}\right) \quad (4.1)$$

where the factor 4 is coming from interference and U_0 is the trap depth produced by a single beam of waist w_0 and power P . The expansion of U_{1D} around the trap center results in the following expressions for the trapping frequencies:

$$\omega_r = \sqrt{\frac{4U_0}{mw_0^2}} \quad (4.2)$$

$$\omega_z = \sqrt{\frac{4\pi^2 4U_0}{m\Lambda^2}} \quad (4.3)$$

in the radial and axial directions respectively.

For a power $P=5$ W and a waist $w_0=20$ μm , the trapping potential is represented in figure 4.1. The trap depth reaches $U_0 = 3625 E_{rec}$ corresponding to 3.6 mK. In this

large intensity regime, the scattering losses of $\Gamma_{scat} = 0.45 \text{ s}^{-1}$ remains small compared to the dynamical time scales.

The trapping frequencies are then: $\omega_r = 2\pi \cdot 43 \text{ kHz}$ and $\omega_z = 2\pi \cdot 2.5 \text{ MHz}$.

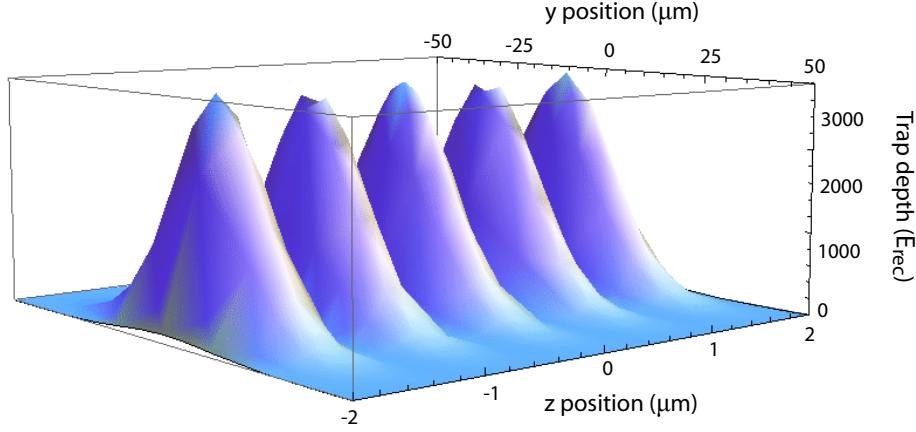


Figure 4.1: *Optical lattice created by a single laser beam having a power $P = 5 \text{ W}$ and a waist $w_0 = 20 \mu\text{m}$. The trap depth reaches $3625 E_{rec}$ corresponding to 3.6 mK and the axial frequency is $\omega_z = 2\pi \cdot 2.5 \text{ MHz}$. Typically 150 different traps are produced, all separated by a distance $d = \Lambda/2$.*

A degenerated atomic sample will be loaded into this 1D optical lattice in order to obtain an array of highly isotropic trapped clouds. For a condensate of $100 \mu\text{m}$ width (FWHM), typically 100 pancake-shaped clouds will be formed.

Two main consequences result from the large trapping frequencies achieved in the optical potential:

- An adiabatic loading in such a confined trap from a magnetic trap will induce a large heating. The loading may thus be followed by an evaporative cooling stage to achieve a kinetic energy ϵ in each of the atomic cloud lower than $\hbar\omega_z \approx 120 \mu\text{K}$.
- The different atomic clouds can be considered as independent since the axial extension of the cloud l_z is much smaller than the lattice spacing d for typical experimental parameters and tunneling is strongly forbidden.

Let us consider from now one single cloud of N_p atoms trapped in an optical potential of frequencies ω_z and ω_r :

$$U_{1D} = \frac{m}{2} (\omega_z^2 z^2 + \omega_r^2 \rho^2) \quad (4.4)$$

In this deep trapping potential, the energy spacing between the eigenstates of the axial harmonic oscillator reaches $\hbar\omega_z \approx 120 \mu\text{K}$, which opens the possibility to reach a regime where only the ground state of this oscillator is populated. To enter this regime, both the typical relative kinetic energy ϵ as well as the interaction energy per particle for a non ideal gas must be small compare to $\hbar\omega_z$. The axial part of the wave function is then

simply described by the ground state ϕ_0 of the axial harmonic oscillator:

$$\phi_0(z) = \frac{1}{\pi^{1/4}\sqrt{l_z}} \exp\left(-\frac{z^2}{2l_z^2}\right) \quad (4.5)$$

with $l_z = \sqrt{\hbar/m\omega_z}$ the axial extension of the atomic wave function. For the largest trapping frequencies, one gets $l_z = 32 \text{ nm} = 4.3 a_s$, regime in which the geometrical confinement will have the largest effect on the collisional properties.

The radial harmonic oscillator having an energy spacing of the order of $\hbar\omega_r \approx 2 \mu\text{K}$, the xy motion will be treated classically. If the motion along z is completely frozen, the 2D character of the relative motion of the particles will manifest itself both for elastic or inelastic collisions.

4.1.2 Elastic scattering in axially confined geometries

The effect of a strong confinement along one dimension on the atomic collisional properties has been studied in [45, 46]. To enlight the peculiar properties of the elastic collisions in confined geometry, it is interesting to study their link to the three-dimensional results.

Three-dimensional collision: In three dimensions, elastic collisions are characterised by the scattering amplitude $f_{3D}(k)$ which only depends on the relative kinetic energy $E = \hbar^2 k^2/m$ of the colliding particles of mass m . In cold atoms experiments, one may frequently regard the limit of this quantity for zero relative energy: the s -wave scattering length denoted a_s (for He^* , $a_s = 7.51 \text{ nm}$ [38]). The elastic collision rate α_{3D} is equal to $\langle \sigma_{3D} v \rangle$ where $\sigma_{3D} = 4\pi a_s^2$ in the scattering cross section and $v = \hbar k/m$ the atomic velocity:

$$\alpha_{3D}(k) = \frac{\hbar k}{m} 4\pi a_s^2 \quad (4.6)$$

in the low energy limit.

Quasi-2D regime: This problem contains two length scales: the extension l_z of the wave function in the z direction and the characteristic radius $r_{int} = 70 a_0$ (a_0 being the Bohr radius) of the ${}^5\Sigma_g^+$ interaction potential denoted U_{int} and described in chapter 3.2. For typical experimental parameters, $l_z \gg r_{int}$ which insures that the relative motion of the atoms in the region of interatomic interaction is not influenced by the tight axial confinement. In the two limits $r \ll l_z$ and $r \gg r_{int}$, the solution of the scattering problem can be expressed easily.

At separation r larger than the range r_{int} of the interaction potential U_{int} , the stationary state can thus be written as a linear combination of products of an harmonic-oscillator eigenstate (labelled by a quantum number ν) in the confined direction and a free wave (labelled by a wave vector \mathbf{q} corresponding to a relative kinetic energy $\epsilon = \hbar^2 q^2/m$) in the radial plane. In the quasi-2D regime, due to the condition $\epsilon \ll \hbar\omega_z$, the incident

and scattered waves have quantum number $\nu=\nu'=0$ for the motion in the axial harmonic potential U_{1D} . As a consequence the scattered 2D wave function may be written as:

$$\psi_{scat}^{2D}(\rho, z, q) \rightarrow \phi_0(z)e^{i\mathbf{q}\cdot\rho} + f_0(q)\phi_0(z)\sqrt{\frac{i}{8\pi q\rho}}e^{iq\rho} \quad (4.7)$$

where $f_0(q)$ is the effective 2D scattering amplitude in the low energy limit. By definition, the corresponding 2D scattering cross-section is given by the integration of this quantity over the angular variable:

$$\sigma_{2D}(\vec{q}) = \int \frac{|f_0(q)|^2}{8\pi q\rho} d\vec{\rho} = \frac{|f_0(q)|^2}{4q} \quad (4.8)$$

The 2D elastic collision rate α_{2D} , equal to $\langle\sigma_{2D}v_{2D}\rangle$, is thus given by:

$$\alpha_{2D}(\vec{q}) = \frac{\hbar}{m} \frac{|f_0(q)|^2}{4}. \quad (4.9)$$

At short separations such that $r \ll l_z$, one can neglect the confining trap and the collision recovers the aspects of a usual 3D collision at energy ϵ . As a result, there is a region where the wave function is proportional to the usual 3D s-wave scattering wave function:

$$\psi_{scat}(\mathbf{r}) = \eta(\epsilon)\phi_0(0)\left(1 - \frac{a_s}{r}\right) \quad (4.10)$$

writing the normalisation coefficient as $\eta(\epsilon)\phi_0(0)$.

Using Green's formalism to match ψ_{scat}^{2D} with the free-space expression ψ_{scat} , one finds the relation between the effective 2D scattering amplitude f_0 and the 3D scattering length a_s [45, 46]:

$$f_0(\epsilon) = 4\pi\phi_0^2(0)a_s\eta(\epsilon) \quad (4.11)$$

where

$$\eta(\epsilon) = \left[1 + \frac{a_s}{l_z} \frac{1}{\sqrt{2\pi}} \left(\ln\left(\frac{B\hbar\omega_z}{\pi\epsilon}\right) + i\pi\right)\right]^{-1} \quad (4.12)$$

with $B=0.915$.

The 2D elastic collision rate can now be linked to the 3D one:

$$\alpha_{2D}(\epsilon) = \frac{\hbar}{m} \frac{|f_0(\epsilon)|^2}{4} = \alpha_{3D}(\epsilon) \frac{1}{kl_z^2} |\eta(\epsilon)|^2 \quad (4.13)$$

with k the 3D wave vector defined as $\epsilon = \hbar^2 k^2/m$.

Omitting the factor $|\eta(\epsilon)|^2$, this expression can be easily derivated from the reduction from 3 to 2 dimensions. For temperature $T \ll \hbar\omega_z$, a characteristic value of the 3D density is $n_{3D} \approx n_{2D}/l_z$ and thus the elastic collisional frequency can be written as $\Omega_{el} \approx \alpha_{3D}n_{2D}/l_z$ giving $\alpha_{2D} = \alpha_{3D}/l_z$. On the other hand, the total kinetic energy for two colliding atoms with relative energy ϵ can be expressed as:

$$\epsilon = \frac{\hbar^2 k^2}{m} = \frac{\hbar^2 q^2}{m} + \frac{\hbar^2}{l_z^2 m} \quad (4.14)$$

As a consequence, for $q \rightarrow 0$ one gets $k \approx 1/l_z$. One finally obtains a similar expression to equation 4.13 without the corrective factor $|\eta(\epsilon)|^2$: $\alpha_{2D} = \alpha_{3D} \frac{1}{kl^2}$.

As a consequence, the 2D kinematics of the relative motion manifests itself via the adimensional parameters $\epsilon/\hbar\omega_z$ and a_s/l_z in the geometrical factor $|\eta(\epsilon)|^2$ (see equation 4.12). One can see that for $a_s/l_z \ll 1$, this factor is equal to 1. In figure 4.2 a), $|\eta(\epsilon)|^2$ is represented as a function of a_s/l_z in the range of experimentally accessible parameters: the higher the trapping frequency, the larger the deviation from 1. Large changes of the order of 50% can be observed. For the largest confinement available, a_s/l_z can be set to approximately 0.25 and thus the logarithmic temperature dependency can be observed: $|\eta(\epsilon)|^2$ varies by 20% as reported in figure 4.2b).

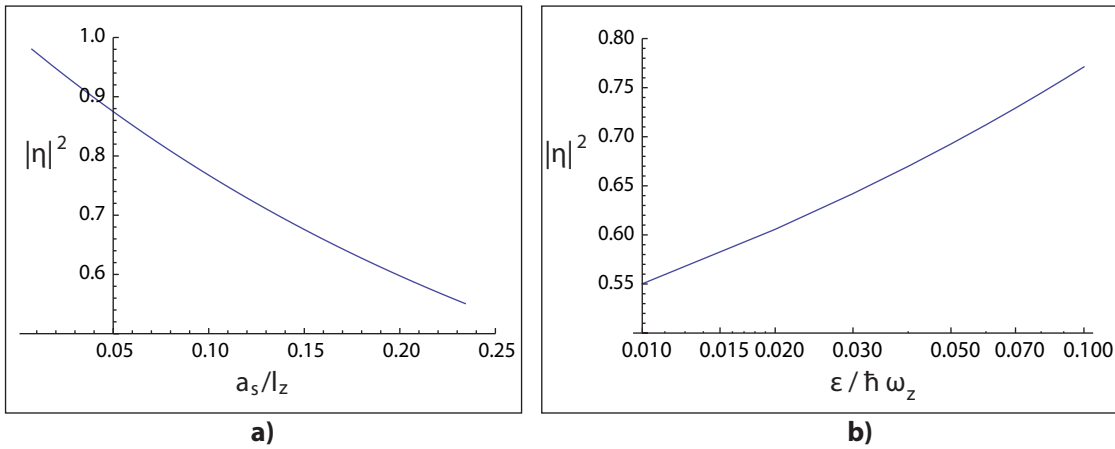


Figure 4.2: a) $|\eta(\epsilon)|^2$ as a function of a_s/l_z for $\epsilon = 0.01\hbar\omega_z$. The ratio a_s/l_z can be varied up to 0.25 corresponding to the maximal confinement of the 1D optical lattice. In the limit of large l_z , the corrective factor is equal to 1, as expected. b) Variations of $|\eta(\epsilon)|^2$ with the temperature in a logarithmic scale. In the ratio $\epsilon/\hbar\omega_z$, ω_z was fixed at the highest frequency achievable for which $l_z = 4.3 a_s$. The temperature range considered is well in the quasi-2D regime since $\epsilon \leq 0.01 \hbar\omega_z$. As the temperature is decreased, the corrective factor further deviates from 1. For $\epsilon \leq 0.01\hbar\omega_z$, the radial motion can no longer be considered as classical.

The modification of the 2D coupling constant g_{2D} induced by the axial confinement can be written as [45, 46]:

$$g_{2D} = \frac{2\sqrt{2\pi}\hbar^2 a_s}{m} \frac{1}{l_z \left(1 + \frac{a_s}{2\pi l_z} \left(\ln\left(\frac{B\hbar\omega_z}{\pi\epsilon}\right) + i\pi \right) \right)}. \quad (4.15)$$

For $a_s \leq 0$, g_{2D} has a resonant dependence in l_z : the interaction changes from attractive for very large l_z to repulsive for $l \leq (|a|/\sqrt{2\pi}) \ln(B\hbar\omega_z/\pi\epsilon)$. Such a resonance is called confinement induced resonance (CIR) analog to the 1D case [43, 44].

One may introduce the dimensionless coupling parameter $\tilde{g}_{2D} = \sqrt{8\pi}a_s/l_z$, quantifying the confinement. Until now, most of the experiments involving 2D gas have been performed in the weak confinement limit ($\tilde{g}_{2D} \ll 1$), in which the logarithm and the imaginary term in equation 4.15 can be neglected [18]. The deep confinement provided by the 1D optical

lattice allows here to reach the strong confinement regime, since typically $\tilde{g}_{2D} \approx 0.9$. It appears that such a quasi-2D regime is peculiar in the sense that the coupling coefficient is intrinsically energy dependent, by contrast to 1D and 3D systems. Another particularity is contained in the imaginary part, which lacks of physical interpretation. Recently, CIR in a strongly confined two-component Fermi gas have been studied [101]. The authors suggest that at a position where the coupling constant is purely imaginary, the gas is not collisionless because the total cross section $\sigma_{2D} = -\Im(f(q))/q = 4/q$ retains a non zero value.

4.1.3 Inelastic scattering in a quasi-2D regime

Inelastic scattering is also influenced by the tight axial confinement of the atomic motion. The inelastic collisions are caused by the weak spin-dipole interaction studied in chapter 3.2 and therefore can be treated within perturbation theory.

To first order in perturbation theory the amplitude of inelastic scattering is given by the general expression:

$$f_{in,2D}(\epsilon) = \frac{m}{\hbar^2} \int \psi_i^{2D}(\mathbf{r}) U_{int}(\mathbf{r}) \psi_f^{2D}(\mathbf{r}) d^3r \quad (4.16)$$

Here ψ_i^{2D} and ψ_f^{2D} are the true wave functions of the initial and final states of the relative motion of colliding atoms. Since inelastic collisions occur at very short interparticular distances, much shorter than l_z , the collision recovers the aspects of a free-space one, described by the 3D potential $U_{int}(\mathbf{r})$.

The wave function ψ_f^{2D} is also the same than in 3D because the relative kinetic energy in the final state is much larger than $\hbar\omega_z$. Thus the only difference from the 3D case is related to the form of the wave function ψ_i^{2D} in such a confined geometry.

As for elastic collisions, the matching of the free space expression 4.10 with ψ_i^{2D} gives a relation between the 2D scattering amplitude $f_{in,2D}$ and the free space one denoted $f_{in,3D}$:

$$f_{in,2D}(\epsilon) = \eta(\epsilon) \phi_0(0) f_{in,3D} \quad (4.17)$$

Therefore, the 2D mean rate constant β_{2D} can be expressed as:

$$\beta_{2D}(\epsilon) = |f_{in,2D}|^2 = |\eta(\epsilon)|^2 \frac{\beta}{\sqrt{\pi} l_z} \quad (4.18)$$

where $\beta = |f_{in,3D}|^2$ is the 3D inelastic collision rate at zero energy. Omitting the factor $|\eta(\epsilon)|^2$, characterising the quasi-2D collisional regime, this expression can be simply derived from the conversion of the 3D atomic density into a 2D atomic density:

$$\beta n = \beta \frac{n_{2D}}{\sqrt{\pi} l_z} = \beta' n_{2D} \quad (4.19)$$

where $\beta' = \frac{\beta}{\sqrt{\pi} l_z}$ is then a two-dimensional inelastic collision rate, obtained while neglecting the quasi-2D collisional regime.

Again, the effect of the quasi-2D collisional regime is contained into the factor $|\eta(\epsilon)|^2$, which is intrinsically energy dependent as reported in figure 4.2 b). Figure 4.3 represents the 2D inelastic collision rate β_{2D} as a function of the ratio $\epsilon/\hbar\omega_z$.

For metastable Helium atoms, one has to be careful: since $a_s \geq r_{int}$, the three dimensional collision rate β depends also on the relative momentum k of the particles [46]:

$$\beta(\epsilon) = \left\langle \frac{\beta}{1 + k^2 a_s^2} \right\rangle_\epsilon \quad (4.20)$$

where the brackets stand for a thermal average. Anyway this produces very small changes in the studied temperature range as one can see from figure 4.3.

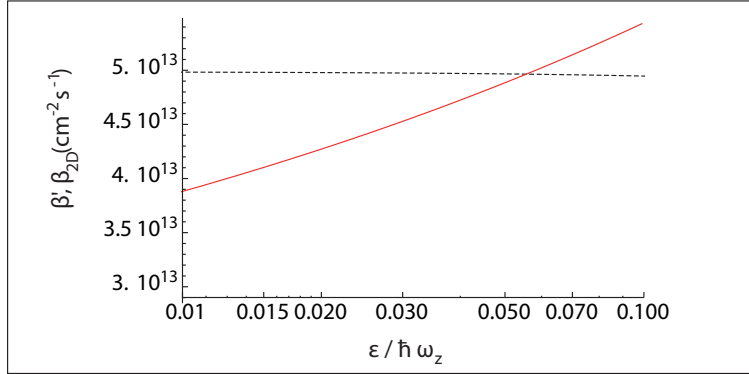


Figure 4.3: *Inelastic collision rates as a function of $\epsilon/\hbar\omega_z$. The black dashed line corresponds to $\beta' = \frac{\beta}{\sqrt{\pi}l_z}$ obtained assuming three-dimensional collisions, almost constant in the studied temperature range. The red plain line represents β_{2D} , varying by more than 20%.*

4.1.4 Experimental observation of the quasi-2D collisional regime

To effectively observe the behaviour described in the previous paragraph, two conditions have to be experimentally realised:

- the possibility to vary freely the temperature of the atomic cloud, only realistic if the cloud remains thermal. Indeed if the atomic cloud is degenerate, the energy ϵ is fixed at the value of the chemical potential μ [102],
- the interaction energy in the cloud has to remain small compared to $\hbar\omega_z$.

Description of the atomic cloud: Assuming both conditions of the quasi-2D collisional regime fulfilled, the number of atoms N' occupying the excited states of the trap cannot exceed the critical value N'_c [102]:

$$N'_c = \sum_{j=1}^{\infty} \frac{j+1}{\exp(j\beta\hbar\omega_r) - 1} \quad (4.21)$$

where $\beta = 1/k_B T$ and ω_r is the radial trapping frequency. As a consequence, for temperatures lower than 10 μK , a cloud of more than 50 atoms will be degenerate and g_{2D} will

depends on μ .

The radial profile of the cloud may thus be described by a 2D Thomas-Fermi model. The coupling constant for elastic scattering will be taken equal to the real part of \tilde{g}_{2D} . The three-dimensional atomic density $n(\vec{r}, z)$ of the trapped cloud is thus described by the product of $|\phi_0(z)|^2$ along z and of a Thomas-Fermi profile in the radial direction:

$$n(\vec{r}, z) = \frac{1}{\Re(g_{2D})} \left(\mu - \frac{1}{2} m \omega_r^2 r^2 \right) \frac{e^{-z^2/l_z^2}}{\sqrt{\pi} l_z} \quad (4.22)$$

where the value of the chemical potential μ is fixed by the normalisation of the atom number to N_p :

$$\mu = \sqrt{\frac{\Re(g_{2D}(\mu)) m \omega_r^2 N_p}{\pi}} \quad (4.23)$$

which is a self-consistent equation for μ .

Solving this equation, with up to 10^3 atoms per pancake, the central 2D density is below $2 \cdot 10^{10} \text{ cm}^{-2}$ and $\mu \leq 40 \text{ } \mu\text{K} \ll \hbar \omega_z$. This last inequality demonstrates that the second requirement of the quasi-2D regime is fulfilled.

Inelastic losses: To induce changes in the geometrical factor $|\eta|^2$, one may modify the chemical potential μ via the number of atoms for instance. The variation of $|\eta|^2$ with the atom number is shown in figure 4.4. As the inelastic collision rate β_{2D} is directly proportional to this factor, its value varies by almost 30% over the studied range, change which is accessible to a measurement.

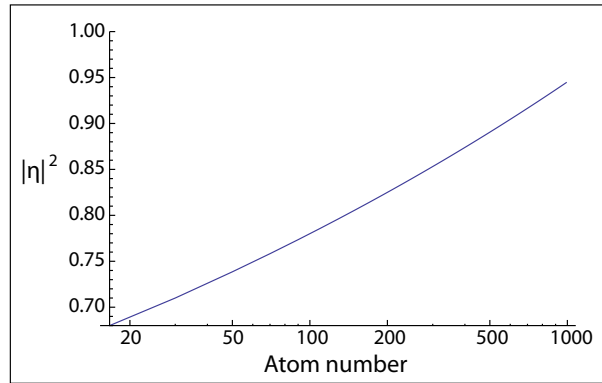


Figure 4.4: $|\eta|^2$ as a function of the atom number per pancake (logarithmic scale). A change of almost 30% can be observed over the studied range.

Collecting the ions produced by Penning ionisation events, the channeltron inside the science cell allows to determine the inelastic mean collision frequency (directly proportional to $|\eta|^2$) averaged over all the atomic clouds. It is then essential to insure that the studied atomic clouds have the same chemical potential, which means an equal filling. This can be conveniently achieved by conserving only the central pancakes.

Another advantage of working with a channeltron for the detection is the possibility to

work with small atom number, since ions can be very efficiently detected.

The typical lifetime of an atomic cloud can be obtained from a numerical integration of the following equation:

$$\frac{dN}{dt} = -\beta_{2D} \int n_{2D}^2(\vec{r}, t) d\vec{r} = -\frac{\beta}{\sqrt{\pi}l_z} |\eta(\mu)|^2 \int n_{2D}^2(\vec{r}, t) d\vec{r} \quad (4.24)$$

where the inelastic collision rate β_{2D} depends on the density via the chemical potential μ . The decay of the atom number will change the value of the chemical potential.

An order of magnitude of the typical lifetimes of such clouds can be deduced while neglecting the logarithmic variation of g_{2D} in μ . With this approximation the differential equation 4.24 can be written has:

$$\frac{dN(t)}{dt} = -\beta_{2D}(\mu) C_3 N(t)^{3/2} \quad (4.25)$$

with $C_3 = \sqrt{m/\tilde{g}_{2D}\omega_r}/3\sqrt{\pi}$

The $1/e$ lifetime ranges from 20 ms to 800 ms for atom number varying from 10^3 to 10. Those lifetimes are short compared to the time scale of the losses due to the scattering of photons from the lattice beams ($\Gamma_{scat} = 0.45 \text{ s}^{-1}$), so that the later can be neglected.

It is interesting to notice that the ion signal produced over time scales shorter than the $1/e$ lifetime of the cloud provides a direct access to $\beta_{2D}(\mu_i)$ and thus to a clear signature of the quasi-2D regime.

4.2 3D optical lattice: Mott Insulator - Superfluid phase transition

The Mott Insulator - Superfluid transition for bosonic atoms illustrates how cold atoms can be used to study many-body phenomena in dilute gases, as first suggested by Jaksch *et. al.* [53]. The Bose-Hubbard model has been first introduced in the context of the superfluid ^4He in [103] and is used in solid state physics. Within this framework, a comparative study between Helium in an optical lattice at $\Lambda = 1560$ nm and Rubidium with $\Lambda' = 852$ nm is conducted.

The behaviour of inelastic collisions in optical lattices has been first investigated with metastable Xenon, Argon and Krypton atoms [104, 105] in a four beam lattice configuration, for which the detuning was small. Inhibition of the inelastic collision rates resulting from the localisation of the atoms on the lattice sites could be observed.

Modeling the dynamics of metastable Helium atoms in a 3D optical lattice requires an extension of the Bose-Hubbard model in order to include dissipation effects, resulting from Penning ionisations. This problem has been recently investigated both for two-body losses [56, 100] and three-body losses [106] and presents intriguing features, especially the production of strongly correlated systems in which tunneling is suppressed. A remarkable example in one dimension is the Tonks-Girardeau (TG) gas, where bosons with strong repulsive interactions minimize their interaction energy by avoiding spatial overlap and acquire fermionic properties [50]. Such a strongly correlated phase could also be studied with He^* taking advantage of the Penning ionisation losses.

A rigorous analysis of the dissipation involves a master equation on the density matrix of the system, which can be interpreted in terms of an effective Hamiltonian, sum of the Bose-Hubbard Hamiltonian and a supplementary loss term.

A prospective study, describing the Penning collisions in the framework of a three-level system, demonstrate the occurrence of a strongly correlated many-body state within the range of our experimental parameters.

4.2.1 3D optical lattice properties

The optical access of the present cloverleaf magnetic trap has been optimised to allow the implementation of a three-dimensional optical lattice at $\Lambda = 1560$ nm. Three orthogonal standing waves, of wave vector $k = 2\pi/\Lambda$, will be overlapped on a waist $w_0 = 100$ μm creating a lattice whose minima are spaced by $\Lambda/2$. To have independent laser fields for each axis and avoid interferences between the three lattice beams, three AOMs will shift the beam frequencies by 110 MHz, 80 MHz and 40 MHz. Their efficiency can be analogically controlled to vary the beam intensity during the loading the lattice or the release of the atoms.

Neglecting the gaussian envelope of the focused lattice beam (which creates additional trapping frequencies of the order of few kHz), the trapping potential can be expressed

as:

$$U_{3D}(x, y, z) = 12U_0 \left(\sin^2(kx) + \sin^2(ky) + \sin^2(kz) \right) \quad (4.26)$$

whith U_0 the tunable trap depth created by a single beam of waist w_0 and power P , as in the previous section.

The expansion of $U_{3D}(x, y, z)$ around the trap center give access to the trapping frequency, identical for the three directions:

$$\omega_{3D} = \sqrt{\frac{4\pi^2 24U_0}{m\Lambda^2}} \quad (4.27)$$

The photon recoil energy for Helium atoms in a lattice of wavelength Λ ($E_{rec} = \hbar^2 k^2 / 2m$) is approximately 20 kHz. The depth reaches $U_0 = 145 E_{rec}$ for the maximum power of 5 W in each lattice beam. The trapping frequency is then: $\omega_{3D} = 2\pi \cdot 850$ kHz.

As a consequence deep optical lattices can be generated in which each well supports many eigenstates (up to 10^3) spaced by $\hbar\omega_{3D}$. In the regime where $T \geq E_{rec}$, all the atoms are in the lowest vibrational level at each site and their motion is frozen except for the small tunneling amplitude to neighbouring sites.

4.2.2 The Superfluid to Mott-insulator transition for Helium

The Bose-Hubbard model, which is commonly used to model this quantum phase transition, describes boson hopping with amplitude J to nearest neighbors on a regular lattice of sites labeled by index l . The particles interact with a zero-range on-site repulsion U disfavoring configurations with more than one atom per site. Writing \hat{b}_l^\dagger the creation operator of a boson at site l and $\hat{n}_l = \hat{b}_l^\dagger \hat{b}_l$ the associated number operator, the Hamiltonian reads:

$$\hat{H} = -J \sum_{\langle ll' \rangle} \hat{b}_l^\dagger \hat{b}_{l'} + \frac{U}{2} \sum_l \hat{n}_l (\hat{n}_l - 1) + \sum_l \epsilon_l \hat{n}_l \quad (4.28)$$

where $\langle ll' \rangle$ denotes a sum over nearest neighbour pairs. The last term is introduced to describe the effect of the non regular trapping potential via a variable on-site energy ϵ_l .

For $T \gg E_{rec}$, atoms are confined in the lowest band of the lattice. The width of this lowest band corresponds to the gain in kinetic energy J due to the nearest neighbour tunneling (more precisely $w = 4J$). An analytic expression can be obtained in this limit [107]:

$$J = \frac{4}{\sqrt{\pi}} E_{rec} \left(\frac{U_0}{E_{rec}} \right)^{3/4} \exp \left(-2 \sqrt{\frac{U_0}{E_{rec}}} \right) \quad (4.29)$$

h/J is the tunneling time scale increasing exponentially with the trap depth U_0 . In figure 4.5 a) the behaviour of h/J with the trap depth expressed in E_{rec} is reported together with h/J_{Rb} evaluated for Rubidium atoms in a lattice at 852 nm as in [54]. One can notice that the tunneling dynamics is approximately 6 times faster for Helium atoms, which corresponds to the ratio of the recoil energies.

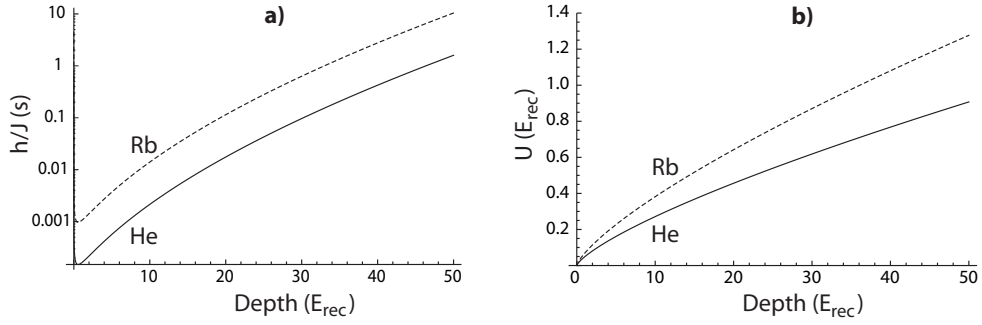


Figure 4.5: a) Tunneling time scale as a function of the trap depth in recoil energy in a semi-logarithmic scale. b) On-site interaction energy as a function of the trap depth in recoil energy. For both graphs the plain line corresponds to the evaluation for Helium atoms in a lattice at $\Lambda = 1560$ nm and the dashed line for Rubidium atoms in a lattice at $\Lambda' = 852$ nm.

The interaction between atoms is described by a zero-range potential U_{int} , only depending on the s -wave scattering length a_s :

$$U_{int}(\vec{x}) = \frac{4\pi\hbar^2 a_s}{m} \delta(\vec{x}) = g\delta(\vec{x}) \quad (4.30)$$

The interaction energy U on one lattice site then reads:

$$U = g \int |w(\vec{x})|^4 d\vec{x} = \sqrt{\frac{8}{\pi}} k a_s E_{rec} \left(\frac{U_0}{E_{rec}} \right)^{3/4} \quad (4.31)$$

where the analytic expression is obtained by taking $w(\vec{x})$ as the Gaussian ground state of the harmonic oscillator potential of the site, which is a good approximation in the limit where $U_0 \gg E_{rec}$ [107]. The on-site interaction U increases with the trap depth because of the squeezing of the atomic wave function.

The behaviour of the on-site interaction energy U as a function of the trap depth is reported both for Helium and Rubidium in figure 4.5. Since the photon recoil energy is more than 6 times larger for Helium, a deeper trap depth U_0 is needed to achieve the same depth in recoil units than for Rubidium. As a consequence, for a trap depth of $50 E_{rec}$ the interaction energy reaches 20 kHz for Helium whereas it remains below 4 kHz for Rubidium.

The assumption that the atoms occupy the ground state of the harmonic oscillator potential of each lattice site remains valid as long as $U \ll \hbar\omega_{3D}$, which is valid on the studied interval (for a trap depth of $50 E_{rec}$: $\frac{U}{\hbar\omega_{3D}} \approx 0.01$).

The ratio U/J determines which from kinetic or on-site interaction energy dominates. For large values of U/J , the on-site interaction dominates and the ground state is a product of local Fock-states with one or more atoms per site. As long as the gain in kinetic energy J is smaller than the on-site interaction U , atoms remain localised, forming a Mott-insulator state. Once J becomes larger than $2U$, the double occupancies become favorable and the atoms are delocalised over the lattice, corresponding to a superfluid state.

	E_{rec} (kHz)	$U_0^c(E_{rec})$	U_0^c (kHz)
He*	20	13.7	280
Rb	3	12.4	40

Table 4.1: Comparison of the trap depths required to cross the superfluid to Mott-insulator transition both for Helium in a 3D lattice at $\Lambda = 1560$ nm and Rubidium in a lattice at $\Lambda' = 852$ nm.

For a cubic three-dimensional lattice, the critical value for the transition from a Mott-insulator to a superfluid phase is expected at $(J/U)_c = 5.8 \times 6$.

Experimentally the ratio U/J can be tuned via the laser intensity as it obeys the following equation, obtained from the ratio of equations 4.29 and 4.31:

$$\frac{U}{J} = \frac{1}{\sqrt{2}} k a_s \exp\left(2\sqrt{\frac{U_0}{E_{rec}}}\right). \quad (4.32)$$

This ratio depends on the atomic specie used to study this phase transition, only via $k a_s$, which has a bounded value. As a consequence the transition will occur at a comparable trap depth in recoil units (but different in absolute units) for Helium and Rubidium atoms as summarised in table 4.1.

4.2.3 Dissipative Bose-Hubbard model

In a recent experiment [56], it has been shown in a 1D lattice that strong inelastic two-body losses can simulate a Pauli exclusion principle, allowing to create a dissipative but long-lived strongly correlated system. The experiment was realised with ^{87}Rb molecules, presenting similar two-body inelastic losses as metastable Helium atoms. The complete theoretical derivation of the effective model presented in this paragraph can be found in [100]. It is here extended to the case of a 3D optical lattice.

4.2.3.1 Effective losses on a single site

In a three dimensional gas, Penning losses are described by a rate constant $\beta_{p,u}$ introduced in chapter 0.1, where the index p or u specifies whether the atomic sample is spin polarised or not. The aim of this paragraph is first to derivate a loss rate $\Gamma_{u,p}$ for two atoms at the same lattice site.

In presence of inelastic collision, the strength of the interparticle interaction ($g = 4\pi\hbar^2 a/m$) can be described by a complex scattering amplitude a : $\Re(a) = a_s$ describes elastic collisions whereas $\Im(a) \leq 0$ describes inelastic losses. In this treatment the on-site interaction matrix element contains both the real part U , introduced in the previous paragraph, and an imaginary part:

$$\frac{\hbar\Gamma_{u,p}}{2} = \Im(g_{u,p}) \int |w(\vec{x})|^4 d\vec{x} = \frac{\hbar\beta_{u,p}}{2} \int |w(\vec{x})|^4 d\vec{x} \quad (4.33)$$

since the rate constant $\beta_{u,p}$ is related to $\Im(g_{u,p})$ via: $\beta = 8\pi\hbar\Im(a_{u,p})/m$. This imaginary part of the interaction constant governs the decay of the number of particles at the site l :

$$\frac{d\langle n_l \rangle}{dt} = -\Gamma_{u,p} \langle n_l (n_l - 1) \rangle \quad (4.34)$$

where $\Gamma_{u,p} = \beta_{u,p} \int |w(\vec{x})|^4 d\vec{x} = \beta_{u,p} U / \Re(g)$ is the loss rate for two atoms at one lattice site.

For a spin polarised sample of metastable Helium atoms ($\beta_p = 10^{-14} \text{cm}^3 \cdot \text{s}^{-1}$), Γ_p is represented as a function of the trap depth expressed in recoil energy in figure 4.6 a). A lattice site, initially containing two atoms, will thus be emptied within a second with a probability 1/2. If the atoms are not spin polarised, the inelastic rate constant is four orders of magnitude larger and this typical time reduces to 0.1 ms as depicted in figure 4.6 b). Those time-scales have to be compared with the tunneling time scale given by \hbar/J , which is approximately 5 ms at the quantum phase transition and increases up to one second for $U_0 = 50 E_{rec}$ (see figure 4.5). As a consequence Penning collisions are a small perturbation to the non-dissipative Bose-Hubbard model for spin polarised atoms as long as the trap depth remains below $35 E_{rec}$ (corresponding to $\Gamma_p \ll J/\hbar$) but constitute a major loss factor if the atoms have different spin states.

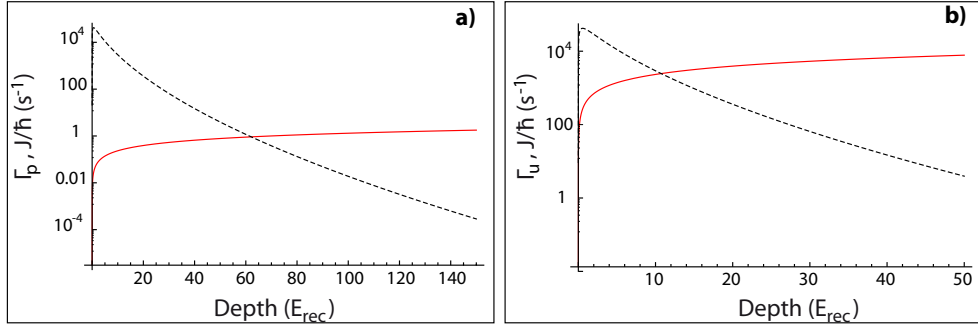


Figure 4.6: Loss rate Γ_p (spin-polarised case) a) and Γ_u (non-polarised case) b) as a function of the trap depth in recoil units. In both graphs, the tunneling rate J/\hbar is reported to ease the distinction of the different regimes.

4.2.3.2 Effective losses over the lattice

To describe this problem, a three-level model is introduced in figure 4.7. Starting from a Mott insulator state with unit filling, losses arises from a tunneling event followed by a decay of the resulting doubly occupied site. The initial state $|1\rangle$ containing two atoms at each lattice site is thus coupled to the state $|2\rangle$ via tunneling of amplitude $\Omega = 2J/\hbar$ (since two final states are possible: two atoms on the left or right lattice site). Those levels are spaced by an energy U , corresponding to the energy cost of a double occupancy, which will be written as a detuning $\Delta = U/\hbar$. The lifetime of the state $|2\rangle$ is limited by a decay rate $\Gamma_{u,p}$, corresponding to Penning ionisation events, which empty the doubly occupied lattice site. Due to the coupling Ω , the initial state $|1\rangle$ decays into the level

$|3\rangle$ with an effective rate Γ_{eff} , for which analytical expressions can be derived in the two limits of strong or weak losses (compared to Ω).

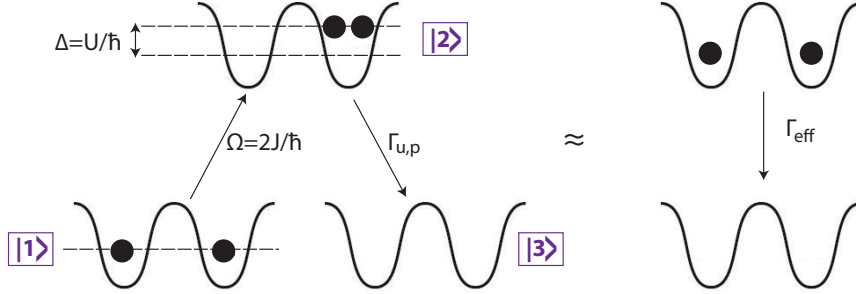


Figure 4.7: Particle losses in a double-well modeled as a three-level system described in the text.

The corresponding non-hermitian effective Hamiltonian can be written within the resolvente theory as [88]:

$$H = \hbar \begin{pmatrix} 0 & \Omega \\ \Omega & \Delta - i\frac{\Gamma_{u,p}}{2} \end{pmatrix} \quad (4.35)$$

The new eigenstates of this Hamiltonian will be denoted $|\tilde{1}\rangle$ and $|\tilde{2}\rangle$, with eigenenergies \tilde{E}_1 and \tilde{E}_2 respectively. The eigenenergies, complex solutions of the equation $\det(H - \lambda I)$ (I being the identity matrix), can be expressed in the two interesting limits of either a spin-polarised or an unpolarised atomic sample.

Regime of weak losses ($\Gamma_p \ll \Omega$): In such a regime, describing a polarised sample of metastable Helium, Penning losses constitute a non-perturbative probe of the dynamics in the lattice. The eigenvalues of the matrix 4.35 can be expressed up to the second order in the small parameter Γ_p/Ω following [88]:

$$\tilde{E}_1 = \frac{\hbar\Delta}{2} - \frac{\hbar\Omega_{eff}}{2} - i\frac{\hbar\Gamma_2}{2} \quad (4.36)$$

$$\tilde{E}_2 = \frac{\hbar\Delta}{2} + \frac{\hbar\Omega_{eff}}{2} - i\frac{\hbar\Gamma_1}{2} \quad (4.37)$$

with:

$$\Omega_{eff} = \sqrt{4\Omega^2 + \Delta^2} \quad (4.38)$$

$$\Gamma_1 = \frac{\Gamma_p}{2} \left(1 - \frac{\Delta}{\Omega_{eff}} \right) \quad (4.39)$$

$$\Gamma_2 = \frac{\Gamma_p}{2} \left(1 + \frac{\Delta}{\Omega_{eff}} \right) \quad (4.40)$$

Two limits are here interesting to discuss:

- $\Delta \gg \Omega$, corresponding to the limit of a deep Mott insulator: the non-perturbed states are only weakly coupled. The lowest correction order in the decay rate Γ_1 of the state $|\tilde{1}\rangle$ then gives:

$$\Gamma_1 \approx \Gamma_p \left(\frac{\Omega}{\Delta} \right)^2 \quad (4.41)$$

- $\Delta \ll \Omega$, corresponding to a superfluid state: in such a case the instability of the level $|2\rangle$ is equally shared between $|\tilde{1}\rangle$ and $|\tilde{2}\rangle$, both having a decay rate equal to $\Gamma_p/2$.

The evolution from the initial state $|1\rangle$ is a complicated damped Rabi oscillation between the two eigenstates of the matrix 4.35. The dominant loss rate will be a smooth interpolation from $\Gamma_p/2$ in the superfluid regime towards Γ_1 given by equation 4.41. The losses will thus remain weak and the polarised sample of metastable Helium can be described within the non-dissipative Bose-Hubbard model.

Regime of strong losses ($\Gamma_u \gg \Omega$): This limit is achieved for unpolarised atoms for a trap depth $U_0 \approx 20E_{rec}$. The coupling being weak, the eigenvalues of the matrix 4.35 will only slightly deviate from the initial energies and thus one may write: $\tilde{E}_1 = \tilde{E}_1^{(1)}$ and $\tilde{E}_2 = \hbar\Delta - i\hbar\Gamma_u/2 + \tilde{E}_2^{(1)}$. The corrective terms $\tilde{E}_1^{(1)}$ and $\tilde{E}_2^{(1)}$ can be obtained up to the second order in Ω/Γ_u and one gets:

$$\tilde{E}_1 = \hbar\Delta' - i\hbar\frac{\Gamma'}{2} \quad (4.42)$$

$$\tilde{E}_2 = \hbar\Delta - \hbar\Delta' - i\hbar\frac{\Gamma_u}{2} \quad (4.43)$$

where:

$$\Delta' = -\Delta \frac{4\Omega^2}{\Gamma_u} \frac{1}{1 + \left(\frac{2\Delta}{\Gamma_u}\right)^2} \quad (4.44)$$

$$\Gamma' = \frac{4\Omega^2}{\Gamma_u} \frac{1}{1 + \left(\frac{2\Delta}{\Gamma_u}\right)^2} \quad (4.45)$$

The system initially in the state $|1\rangle$ will thus evolve, under the tunneling coupling, to the perturbed state $|\tilde{1}\rangle$ in the stationary regime and one concludes that the atoms remain on their original sites with only a minor loss rate Γ_{eff}^1 :

$$\Gamma_{eff} = \Gamma' = \frac{8J^2}{\hbar^2\Gamma_u} \left(\frac{1}{1 + (2U/\hbar\Gamma_u)^2} \right) \quad (4.46)$$

which is inversely proportional to the inelastic collision rate Γ_u . This shows that for strong inelastic collisions ($\Gamma_u \gg J/\hbar$) particle losses are inhibited: $\Gamma_{eff} \ll J/\hbar$. This can be understood in terms of a quantum Zeno effect: losses act as a continuous measurement,

¹We find here the same result than in [56], working in a similar limit.

preventing tunneling events and thus losses.

From this decay rate of two atoms in neighboring sites, one has to deduce the effective decay rate κ over the optical lattice. Equation 4.34 may be rewritten by introducing the pair correlation function $g^{(2)} = \langle n_l(n_l - 1) \rangle / \langle n_l \rangle^2$:

$$\frac{d\langle n_l \rangle}{dt} = -\Gamma_u g^{(2)} \langle n_l \rangle^2 \quad (4.47)$$

As $J/\hbar \ll \Gamma_u$, the probability to have more than two atoms at a lattice site is negligible and one may write: $g^{(2)} = 2p_2/p_1^2$, where p_i is the probability of having i particle at the considered site l . On the site l , p_2 and p_1 are linked via the expression of the losses:

$$p_2\Gamma_u = 6p_1^2\Gamma_{eff} \quad (4.48)$$

where $6p_1^2$ is the probability of having an atom at site l and a second atom in one of the six neighboring sites.

Finally equation 4.47 can be summed over the lattice sites, assuming an initial unit filling for all the lattice sites. In this regime where $\Gamma_{eff} \ll J/\hbar$, the particles have time to redistribute across the lattice between successive loss events. Therefore in the summation over the lattice site, one may consider that the temporal evolution is the same on all the sites and so: $\sum_l \langle n_l \rangle = N_0 \bar{n}$, where N_0 is the number of sites or equivalently the initial number of atoms in the lattice. As a consequence the temporal evolution of the number of atoms in the lattice follows:

$$\frac{dN}{dt} = -\frac{\kappa}{N_0} N^2(t) \quad (4.49)$$

where $\kappa = 12 \Gamma_{eff}$.

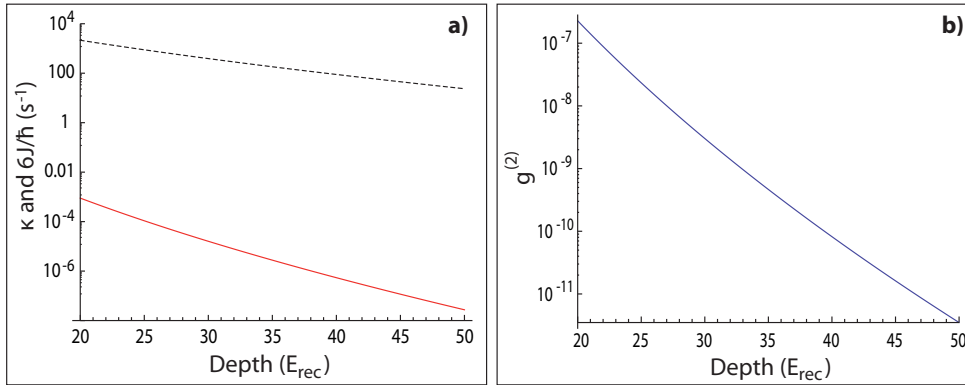


Figure 4.8: a) Effective loss rate over the lattice in the regime of strong inelastic losses. The naive evaluation leading to a loss rate equal to $6J/\hbar$ (black dashed line) largely overestimate the effective loss rate κ (red plain line) resulting from a Zeno blockade of the system dynamics. b) Pair correlation function $g^{(2)} = \kappa/\Gamma_u$ for different trap depths.

Without this quantum Zeno effect, a naive evaluation of the loss rate over the lattice would only involve the tunneling rate J/\hbar , limiting time scale of the problem. In a 3D lattice one atom may tunnel towards 6 neighbouring sites, one would expect the loss rate

to be equal to $6J/\hbar$. The variations of κ and $6J/\hbar$ with the trapping depth are shown in figure 4.8 and show a strong reduction of the losses resulting from the fast dissipation, which freezes the initial state. This situation differs fundamentally from experiments involving deep Mott-insulator states where tunneling is negligible on the experimental time scale and thus losses are suppressed. The mechanism presented here drives the system into a strongly correlated regime. In this limit, the pair correlation function $g^{(2)}$ vanishes, as a result of the fermionisation of the atomic wave-functions. Figure 4.8b) shows an evaluation of $g^{(2)} = \kappa/\Gamma_u$ as a function of the trap depth, which ranges from 10^{-7} to 10^{-11} , much smaller than the typical values ($\approx 10^{-4}$) reported in [56].

The effective realisation of such a strongly correlated system with metastable Helium atoms in a lattice is delicate. One may first load a polarised sample into the optical lattice of desired depth, avoiding then large Penning losses during this stage. Once a unit filling is insured, the atomic sample could be depolarised by means of RF induced transitions between Zeeman substates, which can be done locally using magnetic field gradients for instance [108].

4.3 Conclusion

The cloverleaf magnetic trap presented in chapter 2 has been designed in view of loading a cold cloud of metastable Helium into optical lattices of different dimensionalities. Many interesting phenomenons could be investigated taking advantage of the inelastic Penning losses characteristic of this metastable atom. Among them, two possible experimental studies are described in this chapter.

A one-dimensional optical lattice at $\Lambda = 1560$ nm allows to reach a quasi-2D collisional regime as defined in [45, 46]. The motion along the lattice can be frozen, forcing the atomic wave-function into the ground-state of the axial harmonic oscillator of frequency ω_z . It has been demonstrated that the two conditions to enter this quasi-2D regime can be fulfilled ($k_B T$ and $\mu \ll \hbar\omega_z$). The deep confinement provided by the 1D optical lattice allows here to reach the strong confinement regime, since typically $\tilde{g}_{2D} \approx 0.9$, on the contrary to most of the experiments involving 2D gas, which have been performed in the weak confinement limit ($\tilde{g}_{2D} \ll 1$).

In such a case, the elastic and inelastic collision rates are modified by a geometrical factor $|\eta|^2$, showing an intriguing temperature dependency. This effect can not be studied directly as the atomic cloud will be degenerated, even for small atom number. The kinetic energy is then replaced by the chemical potential. It has been shown, that varying the number of atoms and thus the chemical potential, strong modifications in the geometrical factor can be induced. The channeltron positioned in the science cell provides a direct access to the inelastic collision rate, without any restriction on the atom number. The quasi-2D collisional regime should thus induce a measurable change in the inelastic Penning collision rates.

The description of metastable Helium in a three-dimensional optical lattice requires an extension of the Bose-Hubbard model, in order to describe the losses induced by Penning ionisations.

In this chapter, a simple three-levels system models those losses, either for a polarised gas (weak losses) or for an unpolarised one (strong losses). In the case of weak losses, metastable Helium is well described within the non-dissipative Bose-Hubbard model and should undergo a Mott Insulator - Superfluid transition at a trap depth of $U_0 = 13.7 E_{rec}$. In this regime, the ion signal constitutes a probe of the atomic density and of the dynamics in the optical lattice.

For strong losses, the ability to reach a strongly correlated system, in which tunneling is suppressed by a strong dissipation, has been demonstrated. Large two-body losses thus result in a stabilisation of the system, suppressing double occupancy of lattice sites and as a consequence the losses events. Such open quantum systems are similar to systems studied in quantum optics, which are driven by an external field and coupled to the environment inducing a non-equilibrium dynamics. Diehl *et al.* suggested to take advantage of this novel possibility to drive an atomic system into a many-body quantum state [55].

Chapter 5

Spectroscopy of a forbidden line of ^4He

In atomic systems, theoretical predictions as well as experimental measurements, have reached an impressive accuracy. As a two-electron atom, Helium has been the favorite testing ground for fundamental two-electron quantum electrodynamics (QED) theory. Therefore many frequency metrology studies have been conducted on Helium [109, 110, 35], all involving atomic beam or gas discharges.

The recent production of degenerate gases of ^4He [25, 111] and later ^3He [112, 113] marks a further step in those studies, allowing to reach a higher experimental accuracy.

This chapter presents experimental results achieved during a visit in the group of Wim Vassen at the Vrije Universiteit (VU - Amsterdam) between October 2009 and January 2010. Within 4 months of experimental work, together with R. Van Roij, PhD student in the group, and later on with M. Hoogerland, visitor from the University of Auckland, the first observation of the forbidden $2^3S_1 \rightarrow 2^1S_0$ transition ^4He at $\Lambda = 1557$ nm was realised. Combining the techniques of ultracold atoms and of the optical frequency comb [114, 115], we measured the transition frequency within 10 kHz accuracy corresponding to a relative accuracy of 10^{-11} .

The narrow natural linewidth of this transition (8 Hz) presents an opportunity to test atomic structure calculations and especially quantum electrodynamics (QED) corrections. This transition is also the first direct link between singlet (para-helium) and triplet (ortho-helium) states since electric dipole transitions are forbidden between those two families. The transition at 1557 nm is a magnetic dipole transition, also called "forbidden transition" due to its very low transition rate $\Gamma_{ts} \approx 10^{-7}$ Hz [116], fourteen orders of magnitude smaller than the one of the cooling transition $2^3S_1 \rightarrow 2^3P_2$. As a consequence, two main experimental requirements have to be fulfilled: a long probing duration and a narrow linewidth for the spectroscopy light.

The first section presents the main features of the experimental setup at the VU-Amsterdam along with the characterisation of the implemented crossed dipole trap at $1.5 \mu\text{m}$. A trapped cloud of cold He^* constitutes an ideal experimental situation for frequency metrology allowing long probing duration.

The measurement of the $2^3S_1 \rightarrow 2^1S_0$ transition, observed via losses in trapped ultracold 2^3S_1 atoms is described in the second section. The obtained accuracy relies notably on the frequency comb technique, which will be briefly recalled and detailed in Appendix B. The different experimental shifts are then explained and evaluated, in order to deduce an intrinsic value for the atomic transition frequency.

Most of the final data have been taken and analysed by R. Van Roij and M. Hoogerland after my stay. The last section details the data analysis procedure and the evaluation of the final accuracy of this spectroscopy measurement.

5.1 Experimental setup

The experimental setup at the VU-Amsterdam offers the unique possibility to produce degenerate samples of both the bosonic ${}^4\text{He}$ and fermionic ${}^3\text{He}$ isotopes [112, 113]. This advantage enabled in 2007 a comparative study of the Hanbury Brown-Twiss effect for boson and fermion: two particles interference lead to bunching or antibunching behaviour, depending on their quantum statistics as experimentally shown in [20].

For ${}^4\text{He}$, Bose-Einstein condensation has been achieved in 2006 [27]. As the experimental techniques to produce bosonic degenerate gases at the VU are very similar to the one used at the ENS (see chapters 1 and 2), no detailed description will be provided here. A complete characterisation of the experimental setup can be found in the latest PhD thesis from the group of W. Vassen [71, 72, 117].

This section focuses on the experimental and detection techniques, which constitute key features of the present measurement. I contributed to the full characterisation of the crossed dipole trap, prerequisite of the spectroscopy experiment.

5.1.1 Main features of the experimental setup at the VU-Amsterdam

In Amsterdam, the Bose-Einstein condensate is produced in a large vacuum chamber (roughly 300 mm diameter) and not in a quartz cell. A better collection efficiency at the MOT stage is achieved using large diameter MOT beams ($\varnothing = 4$ cm) trapping up to few 10^9 atoms. After loading a cloverleaf magnetic trap, a 12 s RF evaporation ramp produces degenerate gases with typically several 10^6 atoms.

The large dimensions of the vacuum chamber also give the opportunity to use large microchannel plate (MCP) detectors. A microchannel plate consists in an array of $12 \mu\text{m}$ diameter channels over an active area of 14.5 mm diameter. Each microchannel is an electron multiplier, in which the multiplication is induced by a strong electric field as already described in chapter 1.1.4.

Two MCP detectors have been mounted inside the vacuum chamber to detect specifically He^* atoms falling after release and He^+ ions produced by Penning ionisations in the cloud. MCPs, if equipped with delay line-anodes or phosphorescent screens, are utilised to obtain spatial information. This mode of operation was not applied here, but the time-resolved signals provide useful diagnosis.

The atomic detector, first MCP, is mounted on a translation stage 17 cm below the trapped cloud and is isolated by a metal grounded grid to prevent positively charged particles from being attracted to its surface (see figure 5.5).

When the trap is switched off, due to their large internal energy, He^* atoms falling upon the detector produce a time-of-flight (TOF) signal. The temporal width of the signal is a direct measure of the temperature of the sample (as detailed in chapter 1) and of the fraction of atoms which are condensed. The signal area corresponding to the absolute atom number has been calibrated with absorption imaging.

The second MCP detector is located 10 cm above the trap center and is biased with a voltage of -2 kV to attract He^+ ions. With the maximal gain, single particles produce a voltage pulse which can be distinguished from the noise by discriminators and counted. The ion detector has been used in such a counting mode during the spectroscopy experiment.

5.1.2 Optical dipole trap

The dipole trap light is produced by a NP-Photonics erbium doped fiber laser amplified to provide 2 W of output power at 1557 nm. The central wavelength is tunable over 30 GHz and the specified linewidth at short time scales (≈ 1 ms) reaches 10 kHz (FWHM). The optical crossed dipole trap consists of a single beam, passing twice through the vacuum chamber with orthogonal polarisations to avoid interferences. The two resulting beams, focused to waists of $80 \mu\text{m}$ and $90 \mu\text{m}$, intersect at their foci under an angle of 19° as sketched in figure 5.1. The main disadvantage of this scheme is the loss of power on the returning beam induced by the vacuum windows, non-coated at $1.5 \mu\text{m}$ (approximately 85% of transmission each pass).

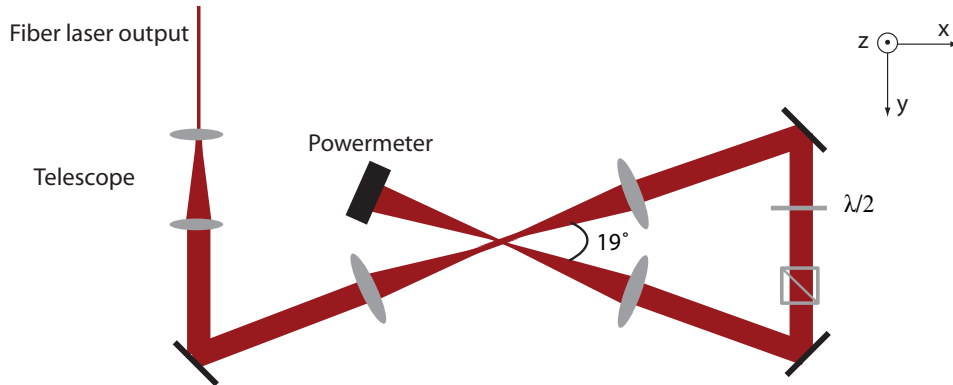


Figure 5.1: a) *Dipole trap setup.* The fiber output of the fiber laser at 1557 nm is expanded by a factor 5 into a two-lenses telescope. The resulting beam is passing twice through the vacuum chamber, providing two focused beams, which are crossing under an angle of 19° at waists of $90 \mu\text{m} \times 80 \mu\text{m}$. To avoid interferences, the polarisation is rotated by 90° before the reflection using a half waveplate denoted $\lambda/2$ positioned after a high quality polarised beam splitter.

Because of the large dimensions of the vacuum chamber and the restricted optical access, the minimal distance between the lenses for the dipole trap and the atomic cloud is of the order of 40 cm. We worked with a focal length $f=50$ cm, which provides a waist $w_0=100\ \mu\text{m}$ for an incoming beam of waist $w=2.5$ mm, following the relation $w = \frac{f\Lambda}{\pi w_0}$. A telescope, schematised in figure 5.1, expands the output beam from the fiber laser source ($w_{\text{fiber}} \approx 0.5$ mm) by a factor of 5. The two lenses are mounted on a two-dimensional micrometric translational stage in order to overlap precisely the waists of the two beams.

The minimal power needed to trap atoms is 40 mW (measured on the powermeter after the two passes through the vacuum chamber depicted in figure 5.1). The power can be increased up to 500 mW, which corresponds to trap depths ranging from $1\ \mu\text{K}$ ($1 E_{\text{rec}}$) to $15\ \mu\text{K}$ ($14 E_{\text{rec}}$). For a power of 400 mW the measured trapping frequencies are $\frac{1}{2\pi}(\omega_x, \omega_y, \omega_z) = (140, 840, 960)$ Hz in good agreement with a theoretical evaluation (the x, y, z axis are defined on figure 5.1).

Since the optical trap is shallow, He^* atoms are first evaporatively cooled in the magnetic trap close to degeneracy ($T > T_c \approx 2\ \mu\text{K}$ for $2 \cdot 10^6$ atoms in the magnetic trap). The dipole trap is switched on during the last 2 seconds of evaporative cooling and the magnetic fields are ramped down within 60 ms. The loading efficiency is of the order of 50%, leading to a transfer of typically 10^6 atoms.

The $1/e$ -lifetime of the trapped cloud is limited by background collisions to 13.5 s, similar as in the magnetic trap (see figure 5.2). The spin-polarisation of the sample is maintained applying a constant bias magnetic field $B_0=2.1$ G in order to inhibit the inelastic Penning collisions. After 2 seconds in the dipole trap, the atomic TOF signal on the MCP detector shows a clear signature of Bose-Einstein condensation.

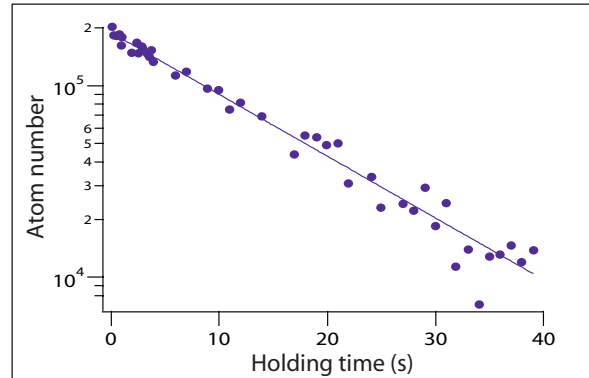


Figure 5.2: Lifetime measurement of $2 \cdot 10^5$ atoms in the dipole trap. The points represent the experimental data and the plain line an exponential fit setting a $1/e$ lifetime of 13.5 ± 0.3 s.

The degenerate cloud is thus described in the Thomas-Fermi approximation [11], where the density profile follows:

$$n(\mathbf{r}) = |\Psi(\mathbf{r})|^2 = \frac{\mu - V(\mathbf{r})}{g} \quad (5.1)$$

with $V(\mathbf{r})$ is the harmonic trapping potential, $g = 4\pi\hbar^2 a_s/m$ and μ the chemical

potential depending on the atom number N , the scattering length a_s :

$$\mu = \frac{1}{2}\hbar\bar{\omega} \left(\frac{15Na_s}{\bar{R}} \right)^{2/5} \quad (5.2)$$

Here we have introduced the average harmonic oscillator frequency $\bar{\omega} = (\omega_x\omega_y\omega_z)^{1/3}$ and the associated length $\bar{R} = \sqrt{\hbar/m\bar{\omega}}$.

The edge of the cloud is therefore given by $V(\mathbf{r}) = \mu$ providing the Thomas-Fermi radii:

$$R_i = \sqrt{\frac{2\mu}{m\omega_i^2}} \quad (5.3)$$

The typical Thomas-Fermi radii of the obtained degenerate cloud are ranging from 11 μm to 18 μm along the y and z axis, and from 107 μm to 64 μm along the x axis. The central density of the cloud is approximately $5 \cdot 10^{13} \text{ cm}^{-3}$.

This degenerate cloud of 10^6 atoms in the 2^3S_1 metastable state constitutes the starting point of the spectroscopy experiment.

5.2 Spectroscopy measurement

The metrology at $1.5\ \mu\text{m}$ is a project already investigated by W. Vassen in [113] for a measurement realised on an atomic beam or atoms confined in an optical lattice.

Here we report on the first direct measurement of the $2^3S_1 \rightarrow 2^1S_0$ transition in a Bose-Einstein condensate of ${}^4\text{He}$ metastable atoms confined in an optical dipole trap.

An overview on earlier frequency metrology studies in Helium motivates the spectroscopy of this narrow transition, which brings a first direct link between ortho- and para-helium. Our measurement relies on optical frequency comb techniques [114, 115] to reach a kHz accuracy on the laser frequency determination. The frequency comb allows also to stabilise the frequency of the spectroscopy light on long time scales (several seconds).

5.2.1 Frequency metrology studies on Helium

Precision spectroscopy on Helium provides sensitive tests of quantum electrodynamics (QED). The QED of free particles (electrons and muons) is a well-established theory providing accurate cross sections among others. In contrast, the QED theory of bound states, determining the atomic energy levels and their lifetimes, needs further precision tests. Three small parameters play a key role:

- the fine structure constant α , involved in relativistic corrections,
- the strength of the Coulomb interaction $Z\alpha$ with Z the atomic number, related to the effect of finite nuclear size,
- the ratio m_e/M between the electron and the nucleus masses accounting for the motion of the nucleus induced by the electron.

Theoreticians are confronted to two kinds of problems: first calculating the expansion of the energy levels in those three parameters up to a certain order and second finding an effective approach to estimate the size of uncalculated higher-order corrections.

The simplicity of this two-electron system allows very accurate calculations of its spectrum. An Helium energy level is conventionally expressed as the sum of three terms: the nonrelativistic energy, the lowest order relativistic correction (up to the second order in the fine structure constant α) and the Lamb shift, which includes QED corrections and the high order relativistic terms. For the two first terms the achieved theoretical uncertainties are smaller than the experimental ones. Present day theory focus on higher order corrections and cross terms for the Lamb shift (including terms up to $O(\alpha^3)$). Due to the large electron density at the position of the nucleus, measurement of S-state energies are the most sensitive to quantum electrodynamics (QED) and nuclear size effects. Low-lying S-states, having the largest higher-order corrections, are the most sensitive tests of atomic structure calculations.

For Helium, optical spectroscopy involving the ground state 1^1S_0 poses unique experimental challenges because of the huge energy gap of about 20 eV to the lowest excited level 2^3S_1 . To excite the 2^1P_1 state, one photon of 58 nm wavelength is required [118] and for the 2^1S_0 two photons of 120 nm.

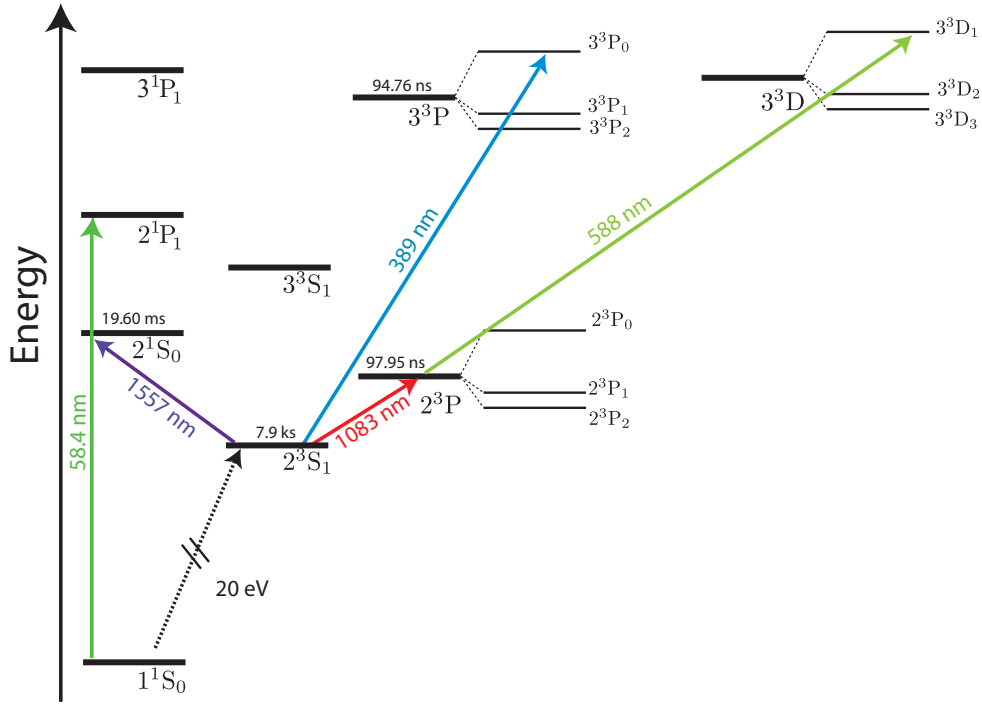


Figure 5.3: Energy levels of ${}^4\text{He}$ (not to scale) and main results of frequency metrology in ${}^4\text{He}$. The present spectroscopy is realised between the two metastable states 2^3S_1 and 2^1S_0 at 1557 nm, first direct link between singlet and triplet states in ${}^4\text{He}$.

Most spectroscopic studies realised so far use the 2^3S_1 or 2^1S_0 metastable states as lower levels and are reported on the energy level scheme (figure 5.3). Metrology measurements inside the para-helium family were dedicated to the $1^1S_0 \rightarrow 2^1P_1$ transition at 58 nm [118] and the series of $2^1S_0 \rightarrow n^1P$ transitions [119].

Transitions measured from the 2^3S_1 state reached 3^3D_1 [109] with two photons and 3^3P_0 [120], both in the ortho-helium family. The fine structure splitting of the 2^3P level has been studied with the highest grade of accuracy in [35], and the one of the 3^3P level in [121]. A good summary of the overall status of the Helium energy level spectrum, both theoretical and experimental, is provided in a recent publication by Morton, Wu and Drake [33].

The transition excited here links two metastable states: the 2^3S_1 triplet state having a lifetime of 7900 s and the 2^1S_0 singlet state with a lifetime of 20 ms, only limited by decay to the ground state 1^1S_0 via two UV photons [122]. The natural linewidth of 8 Hz is $2 \cdot 10^5$ times narrower than for the transition to 2^3P , which has been most prominently used for spectroscopy in Helium so far. The 1557 nm transition, also because it involves two S-states, constitutes therefore an ideal testing ground for QED calculations [33].

Due to spin-conservation rules, the spectra of para-helium and ortho-helium are not connected via electric dipole transitions. So far, triplet and singlet states energies were only linked via the continuum, relying on theoretical evaluations of ionisation energies [123]. Thus the $2^3S_1 \rightarrow 2^1S_0$ transition frequency was deduced from a combination of two

Transition and reference	Transition frequency (MHz)
Measurement of $2^3S_1 \rightarrow 3^3D_1$ [109]	786 823 850.002(56)
3^3D_1 ionisation energy [123]	366 018 892.97(2)
Measurement of $2^1S_0 \rightarrow 7^1D_2$ [110]	893 162 323.880(120)
7^1D_2 ionisation energy [123]	67 169 717.156(2)
$2^3S_1 \rightarrow 2^1S_0$	192 510 701.94(13) MHz

Table 5.1: *Value and accuracy of the indirect evaluation of the $2^3S_1 \rightarrow 2^1S_0$ transition relying on two experimental results and theoretical evaluation of ionisation energies. Errors on the final digits are quoted in the usual way in parantheses. The final error is the quadratic sum of all the contributing errors. This indirect determination reaches an accuracy of 130 kHz.*

spectroscopy measurements and theoretical ionisation energies from high n states. The values are summarised in table 5.1. Error bars in the theoretical evaluation of ionisation energies are indeed smaller for high lying n levels since the main source of uncertainty comes from relativistic and QED corrections of order α^4 , which are the highest for low lying S -states. This indirect evaluation of the transition frequency reaches an accuracy of 130 kHz.

In this section we will describe the spectroscopy of the $2^3S_1 \rightarrow 2^1S_0$ transition, first direct link between singlet and triplet states of Helium. This magnetic dipole (M1) transition has a transition rate of $\Gamma_{ts} = 9.1 \cdot 10^{-8}$ Hz [116], which is fourteen orders of magnitude smaller than for the cooling transition $2^3S_1 \rightarrow 2^3P_2$. As a consequence long probing duration is required in this experiment. Cold atoms techniques, allowing the storage of ${}^4\text{He}^*$ atoms in a crossed dipole trap for several seconds, constitutes therefore a major advantage over atomic beam experiments.

5.2.2 Measurement and lock of the laser frequency

The NP-Photonics fiber laser produces both the dipole trap and the spectroscopy beams (see figure 5.5). As already mentioned, the laser wavelength is tunable over 30 GHz and will be scanned around the $2^3S_1 \rightarrow 2^1S_0$ transition frequency. The frequency is precisely determined from a comparison with an optical frequency comb, which is the key point of the spectroscopy measurement.

Frequency comb technology [114, 115], based on lasers which are mode-locked to a resonant optical cavity, enabled the relative link of optical frequency to radio-frequency where direct electronic frequency counting is possible (up to hundreds of GHz). Mode-locking introduces a fixed phase relationship between the modes of a laser cavity and produces a serie of optical pulses separated in time by the round-trip time in the laser cavity. The spectrum of such a pulse train is a series of equally spaced sharp spectral lines separated by the *repetition rate*, denoted f_{rep} , as schematised in figure 5.4. A constant frequency offset f_{ceo} , the *carrier envelope frequency*, shifts the comb. A complete review on frequency combs can be found in [124] and the principles are presented in Appendix B.

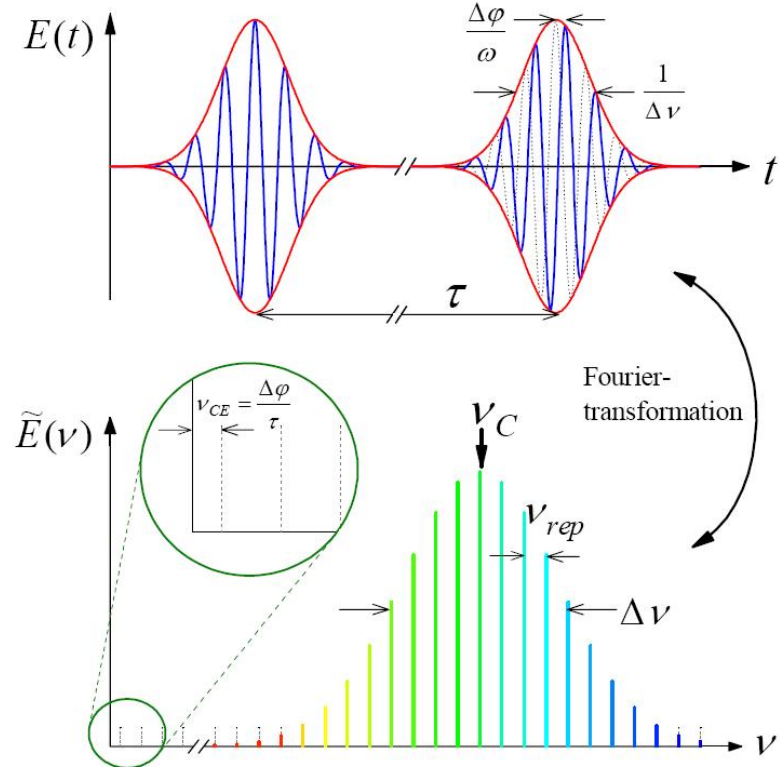


Figure 5.4: *Principle of a frequency comb. A mode-locked laser produces short optical pulses, equally spaced in time. The frequency spectrum is a comb of sharp spectral lines spaced by f_{rep} having an offset f_{ceo} resulting from the phase $\Delta\Phi$ accumulated during each round trip in the cavity.*

In the VU-Amsterdam laboratories, such combs are a daily used technique in the group of K. Eikema, working on high precision metrology [125, 126, 127]. We had the opportunity to use a frequency comb based on a mode-locked erbium doped fiber laser at $1.5 \mu\text{m}$ (Menlo System) with a repetition rate of 250 MHz. Both the repetition rate and the carrier envelope offset frequency are referenced to a GPS-controlled Rubidium clock (PRS10 Stanford Research).

As depicted in figure 5.5, a part of the laser light is split and fiber coupled to the frequency comb. We measure the beat note frequency between our laser and one of the comb mode on a fast photodiode. The lowest frequency beat f_{beat} matches exactly the difference between the laser frequency f_{laser} and the comb mode frequency $f_{ceo} + n f_{rep}$, where n is the unknown integer number of the closest comb mode:

$$f_{laser} = f_{ceo} + n f_{rep} + f_{beat} \quad (5.4)$$

With this technique, a few kHz accuracy for the laser frequency measurement is achieved but the value is provided only modulo 250 MHz. For an absolute determination, a wavemeter accurate to 200 MHz can be used. As wavelength measurement of infra-red

light is not standard, a part of the $1.5\ \mu\text{m}$ light is passing through a doubling crystal (PPLN type from Thorlabs) to generate a $778\ \text{nm}$ laser beam, which is sent into a wavemeter.

This measurement of the beat frequency also allows for an active stabilisation of the laser frequency at a preset value. Indeed the NP-Photonics laser has a specified linewidth of $10\ \text{kHz}$ (FWHM) on time scales shorter than $1\ \text{ms}$, but drifts over $1\ \text{MHz}$ within $2\ \text{s}$. Aiming for long probing duration (few seconds), the laser frequency has to be locked. Therefore the beat frequency is continuously measured by a counter. Its value is sent to the computer via GPIB and regulated by a numerical feed-back loop (proportional-integrator type, PI) to match a set-point value. The analogic error signal produced by the PI loop controls the piezo-electric element of our laser. Although the lock to the frequency comb provides a good long-term stability (corresponding to the Rubidium clock stability), the large comb linewidth of $300\ \text{kHz}$ (FWHM) could broaden our laser narrow linewidth. To avoid this, the time scale of our numerical regulation is limited to $0.2\ \text{ms}$ so that the laser is not to tightly lock to the frequency comb. This locking scheme results finally in a measured long-term laser linewidth of $70\ \text{kHz}$ (FWHM). The set frequency is known within the comb accuracy on long time-scale (several seconds for a typical scan), which is below $2\cdot 10^{-12}$, corresponding to $400\ \text{Hz}$ at for the laser frequency.

5.2.3 Spectroscopy of the forbidden transition

One last point needs to be clarified before describing the experimental sequence: the detection of the fraction of atoms excited in the singlet state. As detailed in paragraph 5.3.3 where AC Stark shifts are evaluated for the triplet and singlet states, atoms promoted in the 2^1S_0 state are expelled from the laser field. The interplay between three time scales has to be considered here:

- time needed to exit the dipole trap volume: assuming a temperature of $9\ \mu\text{K}$ ($T_c \approx 1\ \mu\text{K}$ and maximal trap depth corresponding to $9\ \mu\text{K}$), an atom needs one μs to leave the $80\ \mu\text{m}$ beam waist;
- lifetime of the singlet state: the 2^1S_0 state has a lifetime of $20\ \text{ms}$, only limited by the decay to the ground state via two UV photons [122];
- time scale of the Rabi transitions: considering an intensity I_0 of resonant light on the atomic cloud, the Rabi pulsation Ω_{Rabi} can be evaluated from:

$$\Omega_{Rabi} = \sqrt{\frac{6\pi c^2}{\hbar\omega_{ts}^3} \Gamma_{ts} \langle J_1, M_1, 1 - q | J_2, M_2 \rangle^2 I_0} \quad (5.5)$$

where $\omega_{ts}/2\pi$ is the transition frequency at $1557\ \text{nm}$, $\Gamma_{ts}=9.1\ 10^{-8}\ \text{Hz}$ [116] the transition rate constant and $\langle J_1, M_1, 1 - q | J_2, M_2 \rangle^2$ the squared Clebsch-Gordan coefficient of the $|J_1, M_1\rangle \rightarrow |J_2, M_2\rangle$ transition excited by light with polarisation $q=-1,0,1$. For the most intense probe beam intensity used, the Rabi frequency reaches $200\ \text{Hz}$ corresponding to a $5\ \text{ms}$ time scale.

Since the time needed to escape the cloud is much shorter than the other two time scales, each atom in the singlet state will be lost from the atomic cloud. The excitation of the $2^3S_1 \rightarrow 2^1S_0$ transition is thus detected by probing **atomic losses**.

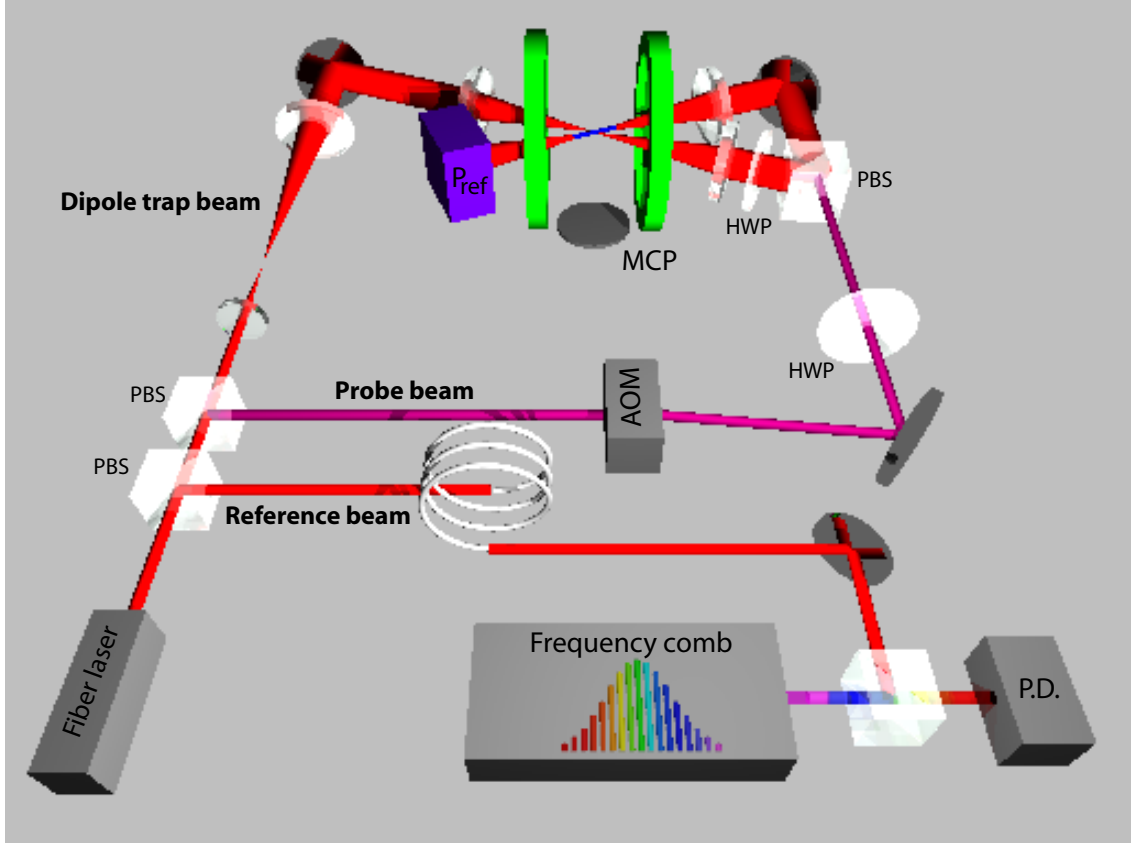


Figure 5.5: *Schematics of the experimental setup. The laser output is divided into three beams: the **dipole trap beam**, the **probe beam**, up-shifted by 40 MHz with an AOM and the **reference beam** fiber-coupled to the frequency comb to measure and lock the laser frequency. The probe-beam is overlapped with the returning dipole trap beam and its waist at the cloud position is measured to be $120 \mu\text{m}$. HWP denotes half-waveplates, PBS polarised beamsplitters, MCP refers to the atomic microchannel detector and P.D. is the fast photodiode used for the measurement of the beat frequency.*

The experiment is now carried out as follows: atoms are transferred from the magnetic trap into the dipole trap and a rethermalisation time of 2 seconds enables to obtain a degenerate gas of atoms in the metastable 2^3S_1 state. Subsequently, a spectroscopy beam up-shifted by 40 MHz as compared to the dipole trap light illuminates the atomic cloud. This beam has a waist of $120 \mu\text{m}$ at the position of the atoms and is overlapped with the returning dipole trap beam. After a specific interaction time t_{int} , the probe and dipole trap beams are switched off. Atoms released from the trap fall onto the MCP detector and their number is recorded. The complete experimental setup is schematised in figure 5.5.

This sequence is repeated for different laser frequencies, changed by 20 kHz steps over typically 800 kHz, in order to scan across the atomic transition. The dipole trap frequency is also scanned but remains 40 MHz away from resonance and thus the weak $2^3S_1 \rightarrow 2^1S_0$ transition is not affecting the trapping potential.

As soon as atoms are promoted to the 2^1S_0 state, atom losses are observed as shown in figure 5.6. After 2 s of probing, approximately 80% of the atoms are lost. The line shape is fitted by a Gaussian of 56 ± 3 kHz σ -width and a center position known within 1.4 kHz accuracy (one- σ confidence interval).

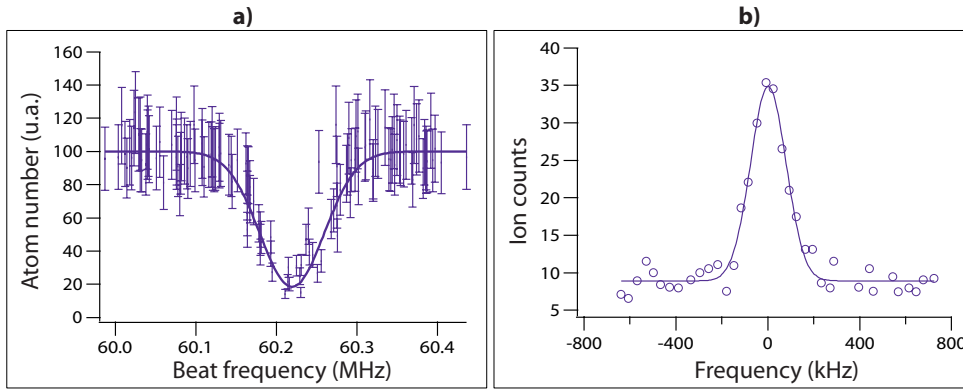


Figure 5.6: a) Remaining atom number after 2 s probing as a function of the beat frequency. The beat frequency is measured between the reference beam and the frequency comb. A Gaussian fit of the data gives a σ -width of 56 ± 3 kHz for a center at $60,219 \pm 1.4$ kHz. The error bars corresponds to shot-to-shot fluctuations of the initial atom number of 20%, which are directly reported onto the final atom number, assuming a constant excitation probability. b) Number of ions produced during the 2 s probing as a function of the frequency (scan realised at a different date than the losses signal). The plain line corresponds to a gaussian fit having a width of 182 ± 8 kHz (FWHM).

For longer interaction time t_{int} ($t_{int} \approx 4$ s) between the spectroscopy beam and the atomic sample, all the atoms can be transferred in the singlet state. However, t_{int} is set to 2 seconds in order to avoid a broadening of the experimental line, induced by a too large efficiency. With this settings, the signal over noise ratio reaches 80%.

Shot-to-shot fluctuations in the atom number, measured to be of the order of 20%, affects the precision of the determination of the line center. This effects, taken into account in the statistical error bar on each data point (see figure 5.6), leads to the determination of the transition frequency within 1.4 kHz accuracy. The stability of the transfer from the magnetic trap into the optical, mainly responsible of those fluctuations, has now been improved.

The error bar on the set frequency determination does not appear in figure 5.6 since it is below 1 kHz (see section 5.2.2).

5.2.4 Resonance observed on the ion signal

As mentioned in section 5.1.1, a second MCP detector, located above the trapping volume, is dedicated to the ion detection. During the probing duration, the ions produced by Penning collisions in the cloud are counted. The atoms in the 2^3S_1 are spin-polarised by a bias field of $B_0 = 2.1$ G in order to avoid losses due to Penning collisions (see chapter 0.1). On the contrary singlet atoms should Penning ionise with the polarised triplet ones and give raise to a coincidence between atomic losses and ion production. A typical ion signal recorded during a scan across the resonance is shown in figure 5.6 b) and has the expected behaviour.

To roughly estimate the ion production rate, one has to determine the probability of a Penning collision between singlet and triplet atoms. The number of collisions N_c experienced by a singlet atom during dt is given by:

$$N_c = \beta_{st} dt \int n_t(\mathbf{r}) n_s(\mathbf{r}) d^3\mathbf{r} \quad (5.6)$$

where β_{st} is the Penning collision rate constant between singlet and triplet atoms. This constant, which has never been measured, will be supposed here similar to the Penning ionisation rate constant of unpolarised triplet atoms: $\beta_{st} \approx 10^{-10} \text{ cm}^3 \cdot \text{s}^{-1}$. For this evaluation the space dependent densities $n_t(r)$ for triplet atoms and $n_s(r)$ for singlet ones are replaced by the central densities $n_{t,0}$ and $n_{s,0}$ and thus the spatial integral by a multiplication by the trap volume V . Concerning the triplet atoms the central density is $n_{t,0} \approx 10^{13} \text{ cm}^{-3}$ for 10^6 trapped atoms. Since typically half of the atoms are promoted into the 2^1S_0 state over 2 s, on short time scales of the order of $1 \mu\text{s}$, only one singlet atom is present in the trap volume and $n_{s,0}V = 1$.

Because singlet atoms, which are anti-trapped in the dipole trap, leave the cloud within $\tau = 1 \mu\text{s}$ (see paragraph 5.2.3), the probability of Penning ionising with a triplet atom is:

$$P_c = \beta_{st} n_{t,0} \tau = 10^{-3} \quad (5.7)$$

During the 2 s probing at resonance, $5 \cdot 10^2$ ions should be produced by Penning ionisation. In [71] a 5% detection efficiency for the ion MCP detector has been measured. This naive estimation predicts the detection of 25 ions at resonance, which is of the same order of magnitude than the measurement. This number depends of course on the exact value of the triplet-singlet Penning rate constant β_{st} and on the average time τ spent by singlet atoms in the cloud.

The background signal of 5 to 10 ions results from Penning collisions between spin-polarised triplet atoms. Indeed the Penning collision rate for spin-polarised atoms is approximately $2 \cdot 10^{-14} \text{ cm}^{-3} \cdot \text{s}^{-1}$, corresponding for a central density of $n_{t,0} \approx 10^{13} \text{ cm}^{-3}$ to a production of 20 ions per second. Due to the 5% detection efficiency of the ion detector, one expects to record few ions over the 2 seconds probing. The ion signal provides thus a clear additional diagnosis on the transition.

This signal has been used to discriminate bad shots (no atoms loaded in the trap and thus no ions detected) from real atom losses due to the probe beam (where more than 30 ions detected). It could in addition provide the first measurement of the singlet-triplet

Penning rate constant β_{st} . Indeed, with a better knowledge of the singlet dynamics and thus of τ , a measurement of the number of ions produced for different triplet densities is a direct measurement of β_{st} .

5.3 Evaluation of the experimental frequency shifts

The position of the line, obtained as described in the previous section, is influenced by all non-zero magnetic or electrical fields required for the measurement and also by atomic interactions. To extract an intrinsic value for the transition frequency, those systematic experimental shifts have to be evaluated precisely.

For low-temperature samples, where only s-wave collisions occur, triplet and singlet atoms experience a different mean field energy, inducing a *mean-field shift* in the atomic transition.

Another frequency shift arises from the bias magnetic field $B_0 = 2.1$ G maintaining the spin polarisation of the triplet atoms: a *Zeeman shift* of the resonance frequency has to be taken into account.

Third, intimately connected to the principle of this experiment, an *AC Stark shift*, produced by both the dipole trap and the spectroscopy beams, affects differently the triplet and singlet states and thus the atomic transition.

5.3.1 Mean field shift

The shift discussed here results from the non ideality of the considered atomic gas. The vector of interactions are collisions and more specifically in a very dilute gas, binary collisions. The collision is then characterised by a scattering amplitude, which depends on the energy of the colliding particles. In the limit of low temperatures where only s-wave scattering occurs, a single scalar parameter, the scattering length a_s , characterises entirely the collision. The interaction between one atom and the others can be treated within a mean-field approximation, resulting in an additional energy term, called mean field energy:

$$E_{mean\,field} = \frac{4\pi n}{m} a_s. \quad (5.8)$$

It is proportional to the atomic density n and the scattering length a between one atom and all the others, and inversely proportional to the atomic mass m .

A cold collision frequency shift [128] originates from the difference in mean field energy between the ground and excited states. The corresponding frequency difference $\Delta\nu_{mean\,field}$ can be expressed as:

$$\Delta\nu_{mean\,field} = \frac{4\pi n_t}{m} (a_s^{ts} - a_s^{tt}), \quad (5.9)$$

where n_t is the atomic density in the 2^3S_1 triplet state, a_s^{tt} and a_s^{ts} the triplet-triplet and triplet-singlet scattering lengths respectively. In contrast to a_s^{tt} which has been accurately measured ($a_s^{tt} = 7.51$ nm [38]), a_s^{ts} is not known. As this shift is proportional to the atomic cloud density n_t , spectroscopy measurements have been performed varying this parameter. At our level of accuracy no effect on the resonance frequency could be observed.

For a typical atomic density $n_t = 3 \cdot 10^{13}$ cm⁻³, the mean field energy of atoms in the triplet state contributes to a 6 kHz frequency shift, smaller than our final error bar. If the triplet-singlet scattering length a_s^{ts} is of the same order of magnitude than a_s^{tt} , the total shift involving the difference between those two scattering lengths could be much smaller than 6 kHz and may thus be neglected in the evaluation of the total error.

An improvement of this accuracy could provide a first measurement of a_s^{tt} or at least an upper bound for its value.

5.3.2 Zeeman shift

A bias magnetic field $B_0 = 2.1$ G is required to maintain the spin polarisation of the atoms in the 2^3S_1 state and thus inhibit Penning collisions. It induces also a large shift in the measured transition frequency. The potential energy of an atom with a magnetic moment $\vec{\mu}$ in a constant external field \vec{B}_0 is expressed as a scalar product:

$$U = -\vec{\mu} \cdot \vec{B}_0. \quad (5.10)$$

When the quantisation axis is along the magnetic field vector, the projection of the magnetic moment becomes $\mu = -gm_J\mu_B$, with μ_B the Bohr magneton, g the Lande factor ($g = 2$ for 2^3S_1 Helium atoms) and m_J the spin projection quantum number.

In this measurement, only the triplet state atoms, in a $m_J = 1$ Zeeman state, are sensitive to the magnetic field B_0 . Atoms in the 2^1S_0 singlet state have indeed $m_J = 0$. The total frequency shift on the atomic transition is then equal to $2\mu_B B_0/h$.

This Zeeman shift is directly measured inducing RF-transition between the Zeeman substates of the triplet state. A RF wave of frequency f_{RF} is applied during 0.5 ms on the ($2^3S_1, m_J = 1$) atoms trapped in the crossed dipole trap. Subsequently the different Zeeman substates are separated during their 5 ms time-of-flight (TOF) by a magnetic field gradient and imaged. When $f_{RF} = 2\mu_B B_0/h$, the $m_J = 0$ and $m_J = -1$ spin states are populated and three well separated clouds are imaged as shown in figure 5.7.

As will be detailed in section 5.3.3, this method provides a measurement of a pure Zeeman shift, with no differential AC Stark shift ¹.

The population of the $m_J = 0$ and $m_J = -1$ spin states is then plotted as a function of the RF frequency (figure 5.7 b)), leading to a determination of the large Zeeman shift (typically 6.1 MHz) accurate at the 10 kHz level, which corresponds to a 4 mG accuracy on the magnetic field value. However, despite this very accurate measurement, the Zeeman shift remains the main source of unaccuracy in this experiment. Indeed the magnetic field value fluctuates at the level of 6 mG during a scan of the spectroscopy beam across the transition, resulting in a 15 kHz rms error on the measured shift. To correct for magnetic field drifts on long time scales, the Zeeman shift is measured before each spectroscopy scan.

To suppress those problems, one could think of working on the $2^3S_1, m_J = 0 \rightarrow 2^1S_0, m_J = 0$ atomic transition insensitive to magnetic fields. But the large Penning collision constant for triplet atoms in an $m_J = 0$ state ($\beta_{00} = 6.6(4) \cdot 10^{-10} \text{ cm}^3 \cdot \text{s}^{-1}$ [41]) is incompatible with the long probing duration required in this spectroscopy experiment. A more realistic approach is to implement an active stabilisation in order to reduce the drifts of the bias field below the 1 mG level (typical for metrology experiments).

¹Since the laser light is far detuned from the $2^3S_1 \rightarrow 2^1S_0$, the fine structure of the triplet state is not resolved and the AC Stark shift is the same (at the 10 Hz level) for the different Zeeman substates (see paragraph 5.3.3).

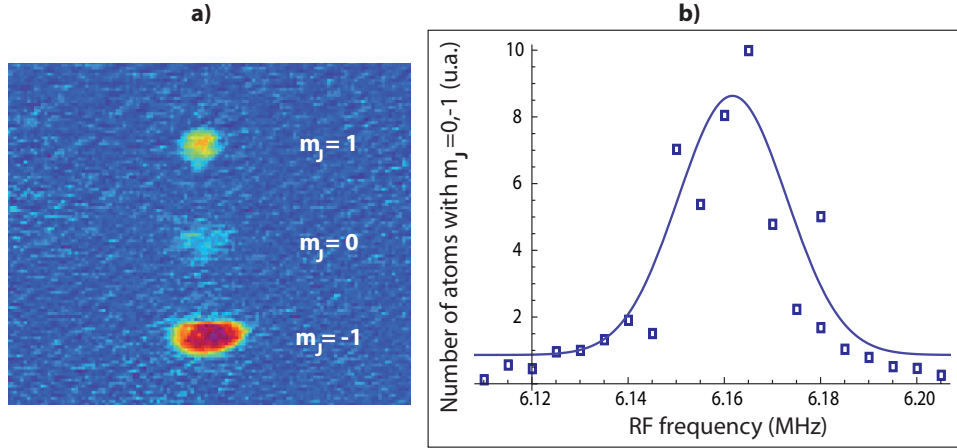


Figure 5.7: a) Absorption image of the trapped atoms taken after a resonant RF excitation of frequency $f_{RF} = 2\mu_B B_0/h$. The different spin populations are separated during a 5 ms TOF in a magnetic field gradient. The RF pulse duration is too long to induce a coherent transfer in one or the other spin states and therefore the relative population of $m_J = 0$ and $m_J = -1$ is varying from shot to shot. b) Number of atoms in $m_J = 0$ and $m_J = -1$ states as a function of the RF frequency. Each point corresponds to the average of three measurements. The plain line represents a gaussian fit yielding a width of $\sigma = 26.5$ kHz (FWHM). The center position is then known within an accuracy of $\sigma/2$. This scan provides a measurement of a $6.16(1)$ MHz Zeeman shift, corresponding to a bias magnetic field $B_0 = 2.200(4)$ G.

5.3.3 AC Stark shift

As explained in chapter 3.1, laser electric fields affect the energy levels of a non-resonant two-level system producing an effective trapping potential when its intensity varies spatially. For all electric fields produced experimentally, this interaction can be treated within perturbation theory. S-states having no permanent electric dipole, the first order perturbation cancels.

The second order Stark shift on the energy level i due to non-resonant transitions to levels k , of frequency ω_{ki} , is expressed as:

$$E_{Stark}^{(2)} = \sum_q \frac{(E_0^q)^2}{2\hbar} \sum_k (d_{ki}^q)^2 \frac{\omega_{ki}}{\omega_{ki}^2 - \omega_l^2} \quad (5.11)$$

where E_0^q is the electric field component of polarisation q , d_{ki}^q is the matrix transition element including the Clebsh-Gordan coefficient of the transition from the state i to the state k with a polarisation q . Thus the AC Stark shift varies linearly with the laser intensity equal to: $I = c\epsilon_0 E^2/2$.

Here both the dipole trap and the probe beam will contribute to this light shift.

Concerning the triplet level, the main shift is induced by the non-resonant $2^3S_1 \rightarrow 2^3P$ cooling transition at 1083 nm. This produces a red-shift, responsible for the trapping of the 2^3S_1 atoms inside the spatially varying intensity profile. As can be seen in equation 5.11, the three polarisations of the light field ($q=1,0,-1$) will induce different AC Stark

Level considered	Transition considered	AC Stark shift (kHz/100 mW)
2^3S_1	$2^3S_1 \rightarrow 2^3P$	- 23(7)
2^1S_0	$2^1S_0 \rightarrow 2^1P_1$	40(12)
	$2^1S_0 \rightarrow 3^1P_1$	-0.60(0.18)
	$2^1S_0 \rightarrow 4^1P_1$	-0.23(0.07)
Total AC Stark shift	$2^3S_1 \rightarrow 2^1S_0$	63(19)

Table 5.2: AC Stark shifts induced on the triplet 2^3S_1 and singlet 2^1S_0 states by the main non-resonant transitions by 100 mW of measured power, with a ratio of 2 between the spectroscopy and dipole trap beams. The error bars quoted in parentheses correspond to a 10% error on the measurement of the beam waists and a 10% error on the power measurement. The total light shift expected on the transition frequency is then 63(19) kHz per 100 mW of laser power measured on the photodiode denoted P_{ref} in figure 5.5, power which is quoted on the horizontal axis in figure 5.8.

shifts. Corrections for the different polarisation states of the light are of the order of the ratio between the fine structure splitting ($\approx 10^9$ Hz) and the laser detuning from the transition at 1083 nm ($\approx 10^{14}$ Hz). This corresponds to corrections at the 10^{-5} level corresponding to few Hz on shift of few tens of kHz. Those small corrections can thus be omitted together with the exact repartition of the light intensity between the different polarisation states $q=1,0,-1$.

The singlet level will be shifted by non-resonant transitions to the states 2^1P_1 ($\lambda = 2058.7$ nm, $\Gamma = 0.0197 \cdot 10^8$ Hz), 3^1P_1 ($\lambda = 501.7$ nm) and 4^1P_1 ($\lambda = 396.6$ nm) from the para-helium family. The transition frequencies and rate coefficient are taken from the NIST database. The total shift is dominated by the effect of the 2^1P_1 state, producing a blue shift and thus expelling the atoms in the 2^1S_0 state from the light field.

The AC Stark shifts have been evaluated for both the triplet and singlet levels and are presented in table 5.2 for 100 mW of laser intensity measured on the powermeter. The transmission of the vacuum windows and the waists of the dipole trap and probe beams have been measured and used as input parameters in this theoretical evaluation. Taking a 10 % error into account on both measurements, the evaluated light shift has a 30% uncertainty.

5.3.4 Conclusion on systematic experimental shifts

Two last sources of systematic frequency shift need to be discussed before concluding this section. First, since the atomic sample consists in a pure Bose-Einstein condensate, no Doppler shift has to be taken into account here.

An incompressible shift results from the momentum transfer from a 1557 nm photon to an atom and is calculated to be 20.6 kHz for ${}^4\text{He}$. No further shift due to the absorption of photons from the beam is involved in this experiment. Indeed as explained in paragraph 5.2.3, triplet atoms absorb only one photon from the spectroscopy beam before

escaping the trap. As a consequence no cooling or heating processes is induced and no light-force-induced line center shift is expected.

Each measured position of the atomic transition is then systematically shifted by the recoil shift of 20.6 kHz, the Zeeman shift and the AC Stark shift. The mean-field shift is neglected at our level of accuracy. The data analysis procedure implemented to correct the line position for those shifts is detailed in the next section.

5.4 Intrinsic transition frequency and measurement accuracy

This section is dedicated to the determination of the field-free resonance position and the evaluation of the final measurement accuracy.

5.4.1 Derivation of the field-free transition frequency

Each scan across the resonance provides a position of the resonance accurate to 1.4 kHz (one- σ confidence interval). The Zeeman shift is measured, following the procedure described in paragraph 5.3.2, and subtracted to the line position. Another possibility would have been to take advantage of the linear variation of this shift with the bias magnetic field B_0 : obtaining the line position for different values of B_0 allows to extrapolate to the magnetic-field free atomic resonance. Since the Zeeman shift measurement has a 5 kHz accuracy, the accuracy improvement resulting from this long procedure is not required.

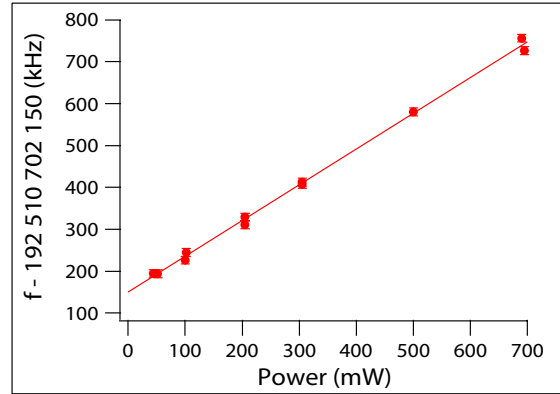


Figure 5.8: Measured transition frequency as a function of the total laser power. Each point is obtained by performing three measurements, all having been corrected for the Zeeman shift and the recoil shift. The error bars on each point takes several effects into account: the fit accuracy to assign the transition frequency of typically 1.4 kHz (one- σ confidence interval), the error of 15 kHz rms due to the magnetic field drifts and the Doppler broadening. The red line represents a linear fit of the experimental data intersecting the y axis at $f=192\ 510\ 702.151(6)$ MHz. The slope is evaluated to 85 ± 2 kHz/100 mW.

In order to correct for the AC Stark shift, the previous procedure has been realised for five different laser intensities. As shown in figure 5.8, the total power (measured for both beams on the photodiode P_{ref}) has been varied between 40 mW and 700 mW, keeping a ratio of 2 between the power in the dipole trap and in the spectroscopy beams. The slope of the obtained line is 85 ± 2 kHz/100 mW, of the same order than expected from the evaluation reported in table 5.2.

As the light shift increases linearly with the total laser power, an extrapolation to zero intensity is possible. The intersect with the y axis in figure 5.8 gives the intrinsic transition frequency $f=192\ 510\ 702.150(6)$ MHz for ${}^4\text{He}$. This value is in good agreement with

the QED calculations [33] and the ionisation energies of those states [123] as summarised in table 5.3.

5.4.2 Experimental broadening and measurement accuracy

Each step of the procedure leading to the intrinsic frequency transition has now to be analysed regarding its contribution to the final measurement accuracy. Indeed the position of the line determined from one measurement has to be shifted by the different systematic shifts (recoil, Zeeman and Stark shift) as described above, and thus the accuracy on the position of the intrinsic transition is limited by the accuracy on the evaluation of those different shifts.

The atom number fluctuations contribute for a 1.4 kHz unaccuracy (see paragraph 5.2.3) on the line position but has no impact on the systematic shifts taken into account in this study. Indeed only the mean field shift, neglected here, is density dependent.

An additional source of unaccuracy are the magnetic field drifts during one scan across the transition. As already discussed in paragraph 5.3.2, the Zeeman shift evaluation contains a 15 kHz error corresponding to 5 mG fluctuations of the bias field B_0 . Working in a magnetic trap would have induced a larger broadening because the shot-to-shot stability of the bias field, resulting of the compensation of two large magnetic fields, is more difficult to insure. The cloverleaf magnetic trap design described in [129], similar to the one of Wim Vassen's group, results in fluctuations of 30 mG corresponding to a 84 kHz error. The dipole trap is therefore more appropriate for a spectroscopy measurement at the 10 kHz level.

Finally, even if the atomic sample consists in a pure condensate at zero-temperature, this spectroscopy experiment involves Doppler broadening. The finite size of the condensate indeed implies a distribution of non-zero momenta. In the Thomas-Fermi approximation, the condensate wave function $\Psi(x, y, z)$ in an harmonic trapping potential is:

$$|\Psi(x, y, z)|^2 = n_0 \left(1 - \left(\frac{x}{R_x} \right)^2 - \left(\frac{y}{R_y} \right)^2 - \left(\frac{z}{R_z} \right)^2 \right) \quad (5.12)$$

where R_i are the Thomas-Fermi radii defined in paragraph 5.1.2. The distribution of momenta p_i along the i axis is given by the square of the Fourier transform of the wave function $\Psi(x, y, z)$ [69]:

$$|\Psi(p_i)|^2 = \left[J_2 \left(\frac{p_i R_i}{\hbar} \right) \left(\frac{p_i R_i}{\hbar} \right) \right]^2 \quad (5.13)$$

with J_2 the Bessel function of order 2 having a rms width of $\Delta p_i = \sqrt{21/8} \hbar / R_i$. The corresponding Doppler broadening is inversely proportional to the condensate size R_i and therefore more pronounced along tightly confining axis:

$$\Delta \nu_{p,i} = \sqrt{\frac{21}{8}} \frac{\hbar}{m R_i \Lambda_0}. \quad (5.14)$$

Experimentally the finite size of the condensate contributes to a maximum 1.5 kHz additional broadening, one order of magnitude smaller than the other broadening sources.

After correcting the line position for the Zeeman shift and the recoil shift, the error attributed to the point is the quadratic sum of the errors induced by the shot-to-shot changes of the atom number, the magnetic field drifts and the Doppler broadening, all acting independently. Since the measurement duration is long compared to the time scales of power fluctuations, one may consider the latest as being averaged. The total error is thus of the order of 15.6 kHz, constant for all data points and dominated by the error on the magnetic field determination.

At a particular laser intensity, the measurement is reproduced 3 to 4 times, the resulting statistical error is reduced to 9 kHz.

As a consequence, the final accuracy of our measurement is set by the accuracy of the linear fit on the measured transition frequencies for different laser intensities (see figure 5.8). We finally achieve a 6 kHz (one- σ confidence interval) accuracy, corresponding to a measurement of the $2^3S_1 \rightarrow 2^1S_0$ transition at a 10^{-11} level. This error is substantially smaller than the errors quoted for both the QED calculations and the indirect evaluation detailed in table 5.1 as summarized in table 5.3.

Source	$2^3S_1 \rightarrow 2^1S_0$ transition frequency (MHz)
QED calculations [33]	192 510 703.4(3.0)
Indirect evaluation (table 5.1)	192 510 701.96(13)
Present experiment	192 510 702.150(6)

Table 5.3: *Values for the $2^3S_1 \rightarrow 2^1S_0$ transition frequency. Our experimental result is in good agreement with both the QED calculations and the indirect evaluation using experimental data and ionisation energies (see table 5.1).*

5.5 Conclusion and perspectives

During my stay at the VU-Amsterdam in the group of Wim Vassen, a crossed dipole trap for metastable Helium, producing a degenerate sample of up to 10^6 metastable atoms, has been implemented and characterised. We realised the first direct observation of the $2^3S_1 \rightarrow 2^1S_0$ magnetic dipole transition via losses in a trapped condensate of metastable ^4He atoms. After a careful evaluation of the statistical errors and systematic shifts, the transition frequency is determined within 6 kHz (one- σ confidence interval) to be $f=192\,510\,702.150(6)$ MHz. This measurement is in agreement with both the QED evaluations and the indirect evaluation combining experimental and theoretical knowledge (see table 5.1).

This first direct measurement of the transition linking the para- and ortho-states family in the ^4He spectrum combines the advantages of the cold atoms field, having a condensate of $^4\text{He}^*$ atoms, with state-of-the-art frequency combs technology. Active stabilisation of the magnetic fields and a more advanced method to lock the laser frequency (using an optical cavity to keep a narrow linewidth) should lead to a kHz accuracy. However the present experimental error of 6 kHz is substantially smaller than estimates of non-evaluated higher order terms in QED calculations (presently evaluated at 3 MHz [33]) and presents a significant challenge for groups involved in atomic structure theory.

New insights in the scattering between triplet and singlet atoms may be investigated improving the present experimental setup. As already mentioned, improving the experimental accuracy could allow for a determination of the triplet-singlet scattering length a_{ts} via the mean-field shift which is density dependent (see paragraph 5.3.1). Moreover, the ion signal recorded on the MCP detector while exciting atoms into the 2^1S_0 state could provide a first measurement of the singlet-triplet Penning ionisation rate constant β_{st} as explained in paragraph 5.2.4.

This study has also demonstrated the principle of an efficient source of cold atoms in the singlet state: all the triplet atoms can indeed be transferred into this state. A dipole trap could be designed to trap them simultaneously with the cold 1^1S_0 ground state atoms that are produced after two-photon decay, allowing for a precise spectroscopy on the $2^1S \leftrightarrow 1^1S$.

Finally, this spectroscopy measurement offers an alternative to the so far best measurement of the isotope shift realised on the $2^3S_1 \rightarrow 2^3P$ cooling transition [35] achieving a 5 kHz accuracy. Indeed the experimental setup in Amsterdam provides degenerate gases of both isotopes ^3He and ^4He . The transition frequency for ^3He has been measured in March 2010 by the Amsterdam group within the same accuracy than ^4He (article to be submitted).

In the isotope shift QED effects cancel partly giving access to accurate measurement of nuclear charge radius differences between both isotopes, testing nuclear size calculations of few-nucleons systems. An accuracy of 1 kHz would provide a measurement of the charge radius difference at the level of 0.001 fm, competitive with the present best determination.

Chapter 6

Conclusion

As mentioned in the introduction of this thesis, working with ultracold metastable Helium atoms presents two major advantages:

- the atomic properties such as energy levels or interaction potential are theoretically well studied and a comparison of the experimental results with the theory is challenging,
- the large inelastic Penning losses constitute a non-destructive diagnostics of the collision dynamics.

The different topics addressed in this work illustrate those two features, either via experimental results or prospective studies.

The two first chapters present the first construction steps towards a new generation of experiments with condensed metastable Helium gas in either an optical dipole trap or an optical lattice. The new detection device added to the setup provides a key feature for the future experiments. The signals obtained so far, either from ions produced in the trapped cloud by Penning collisions or by metastable atoms, have been analysed and provide quantitative evaluations of the dynamics of the trapped sample or of its temperature. A novel cloverleaf magnetic trap, allowing an in-situ loading of a magnetically trapped cold atomic cloud into an optical lattice of various dimensionality, has been implemented. We could load efficiently 10^8 atoms and achieve a phase-space density of $\chi \approx 7 \cdot 10^{-6}$ after a 1D Doppler cooling stage. The first approaches in evaporative cooling this atomic sample demonstrated a critical instability of the bias field. The relative position of the magnetic coils has now been changed in order to reach more stability.

Prospective experiments involving metastable Helium atoms in optical potential are detailed in chapters 3 and 4. After a brief introduction on optical potentials, the dipole trap, which will be implemented in the next future, is characterised. The magnetic field being a free parameter, the variation of the spin relaxation and relaxation induced Penning ionisation rate constants can be experimentally determined. Following the theoretical results from [22, 23], we present a new theoretical evaluation integrating the latest molecular potential available [36]. The realisation of the measurement could provide new informations on the interatomic potential of the $^5\Sigma_g^+$ electronic state. This measurement relies on the ability to distinguish between losses due to Penning ionisation, producing a signal

on the channeltron detector, from other loss mechanisms.

This ability opens many other possibilities. It would for instance allow to verify whether the limiting process for the lifetime of a dimer of metastable Helium $^4\text{He}_2^*$ is the auto-ionisation Penning induced by spin relaxation. This assumption leads to a theoretical evaluation of $\approx 120 \mu\text{s}$ lifetime [40], two orders of magnitude larger than the measured value of $1.4 \pm 0.3 \mu\text{s}$ [39].

The channeltron provides also a direct detection of ions produced during the decay of photoassociated exotic molecules, as realised previously in our group [38, 39, ?]. Photoassociation experiments on BEC attracted a lot of interest from the theoretical point of view, but only few experimental realisations: saturation of the photoassociation rate [130, 131], dynamics of the molecule formation [132, 131], creation of correlated atom pairs [133].

Chapter 4 focuses on prospective studies of intriguing aspects of Penning losses in 1D and 3D optical lattices.

The deep trapping potential produced by a 1D optical lattice at $\Lambda = 1560 \text{ nm}$ allows to reach the strong confinement regime, freezing the atomic motion along one direction. In this reduced dimensionality, both elastic and inelastic collisions are modified [45, 46] and present interesting signature. Confinement-induced resonances (CIR), occurring in such regimes, have been recently experimentally observed in 2D lattices [51]. The investigation of mixed-scattering occurring when the collision partners are confined in different dimensions (3D and 2D in this case) have revealed mixed-dimensional resonances [52]. Nevertheless until recently the strong confinement regime had no experimental realisation [101]. A prospective study demonstrates that quasi-2D collisional effects could be measured on inelastic Penning rates in independent degenerated clouds of metastable Helium. The study of strongly correlated many-body systems has motivated many experimental studies. A remarkable example in one dimension is the Tonks-Girardeau (TG) gas, where bosons with strong repulsive interactions minimize their interaction energy by avoiding spatial overlap and hence acquire fermionic properties [50]. This strongly correlated phase could also be studied with He^* taking advantage of the Penning ionisation losses. Within the formalism of a three-level model, the losses in a 3D optical lattice of metastable Helium atoms, either polarised or not, are evaluated. This study demonstrates the possibility to achieve a strongly correlated regime, as in which large two-body losses result in a stabilisation of the system, suppressing double occupancy of lattice sites and as a consequence the losses (similar effect than in one dimension [56]).

The last chapter reports on a direct spectroscopy measurement of the $2^3S_1 \rightarrow 2^3P_2$ transition of ^4He , realised in the group of W. Vassen at the VU-Amsterdam. This determination involved the state-of-the-art techniques of cold atoms, probing a degenerate sample of metastable Helium trapped in an optical dipole trap, and of optical frequency combs, allowing both to lock and accurately control the laser frequency (within the experimental time-scale). The obtained value of $f = 192\,510\,702.150(6) \text{ MHz}$ is in agreement with the actual determinations, either from QED or from indirect evaluations.

Several results concerning spectroscopy studies conducted on Helium are recalled, showing the strong interest raised by its simple energy level structure. This spectroscopy measurement offers an alternative to the so far best measurement of the isotope shift realised

on the $2^3S_1 \rightarrow 2^3P$ cooling transition [35] achieving a 5 kHz accuracy. The experimental setup at the VU-Amsterdam provides degenerate gases of both isotopes ^3He and ^4He and allowed a determination of the transition frequency for ^3He , which has been measured in March 2010 within a comparable accuracy than ^4He (to be submitted). In the calculation of isotope shift QED effects cancel partly. As a consequence accurate measurements of nuclear charge radii differences between the two isotopes, testing nuclear size calculations of few-nucleons systems. An accuracy of 1 kHz would provide a measurement of the charge radius difference at the level of 0.001 fm, which is competitive with the present best determination.

With an improved accuracy, different properties of the scattering between triplet and singlet atoms (more specifically: the scattering length and the Penning ionisation rate) could also be deduced.

Appendix A

Optical imaging

This appendix details the method used to determine the atom number via absorption imaging on the $2^3S_1 \rightarrow 2^3P_2$ transition. The main limits result from the 2% quantum efficiency of our CCD camera at $\lambda_0 = 1083$ nm. Working with large photon number impose a trade off between the intensity of the imaging beam, which has to remain below I_{sat} in order to remain in the limit of a linear absorption and the probing duration, which has to remain short compare to the cloud expansion after release from the trap.

The first section provides a description of the present imaging system and the general framework for the determination of the atom number.

The second section addresses the problems linked to the unpure polarisation of the probe beam and discusses the corrective factors, accounting for optical transitions between degenerated levels.

A third section presents the chosen parameters for the beam intensity and probe duration and their impact on the determination of the atom number and the cloud temperature.

A.1 Absorption imaging

A.1.1 Experimental setup

The imaging beam is propagating in the $x = 0$ plane of the magnetic trap along an axis making an angle of 45° with the z axis as depicted in figure A.1 and linearly polarised. After a single pass through the cloud, it is retroreflected with an orthogonal polarisation in order to avoid any radiation pressure effects as will be detailed in the following section.

The imaging system consists of two lenses of focal lengths $f_1 = 20$ cm and $f_2 = 15$ cm respectively. The choice of f_1 is imposed by the geometry of the magnetic trap, which sets the smallest distance from the cell center at 20 cm. The magnification on the CCD camera is thus $g = 0.75$.

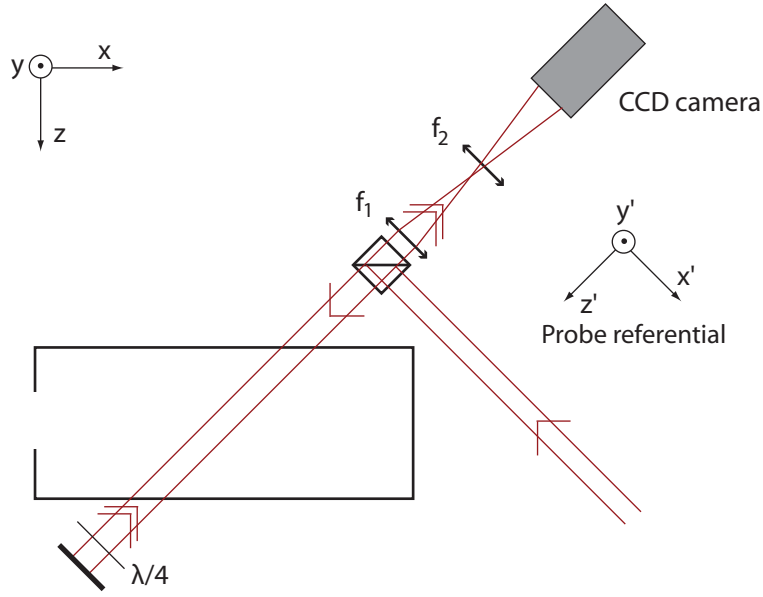


Figure A.1: *Schematics of the imaging system. The probe beam is retroreflected with an orthogonal polarisation and extracted with a polarising beam splitter. The imaging lenses have focal length of $f_1 = 20$ cm and $f_2 = 15$ cm. The magnification on the CCD camera has been measured to be $g = 0.75$.*

A.1.2 Absorption from the atomic cloud

For a two level system, the total scattering rate γ_p from the light field having detuning Δ from the atomic transition can be expressed as [134]:

$$\gamma_p = \frac{s\Gamma_0/2}{1 + s + (2\Delta/\Gamma)^2} \quad (\text{A.1})$$

with $\Gamma_0 = 2\pi 1.62 \text{ MHz}$ the linewidth of the considered atomic transition and s the saturation parameter defined as the ratio of the beam intensity I over the saturation intensity $I_{sat} = \pi\hbar c\Gamma/3\lambda_0^3$. The amount of absorbed power per unit of volume is then given by $\hbar\omega_0\gamma_p n$, where n is the atomic density.

If the probe beam intensity I is small compared to I_{sat} , the population of the excited state and thus stimulated emission (adding photons into the probe beam) may be neglected. In this limit the power dP absorbed from the probe in a volume $dx'dy'dz'$ can be simply expressed as:

$$dP = \hbar\omega_0\gamma_p n(x', y', z') dx' dy' dz' = -dI(x', y', z') dx' dy' \quad (\text{A.2})$$

where the atomic density is denoted $n(x', y', z') dx'$ and the probe intensity variation $dI(x', y', z')$. In this model a new referential is chosen so that the probe beam propagates along the z' axis.

The cross section λ for light absorption is then defined as $dP = \lambda n I$ and written as:

$$\lambda = \lambda_0 \frac{1}{1 + s + (2\Delta/\Gamma)^2} \quad (\text{A.3})$$

with $s \ll 1$ and λ_0 the resonant cross section:

$$\lambda_0 = \frac{\hbar\omega_0\Gamma}{2I_{sat}} = \frac{3\lambda_0^2}{2\pi} \quad (\text{A.4})$$

In this limit, the profile of a probe beam with an initial intensity I_0 after propagation along an axis z' through the atomic cloud is then:

$$I_{abs}(x', y') = I_0 \exp\left(-\lambda \int n(x', y', z') dz'\right) \quad (\text{A.5})$$

A.1.3 Determination of the atom number

The atom number is determined for a resonant probe ($\Delta=0$) in the limit of a small intensity compared to the saturation intensity. The analysed image results from three images: the first one records the absorption of the atomic cloud I_{abs} , the second is taken few hundreds of ms after releasing the cloud to calibrate the intensity sent onto the atoms I_0 . The third image is taken without probe beam in order to subtract the background light, denoted I_b from the two first images.

Since the probe beam is retroreflected, it is absorbed twice by the atomic cloud and one obtains:

$$I_{abs}(x', y') = I_0(x', y') \exp\left(-2\lambda \int n(x', y', z') dz'\right) \quad (\text{A.6})$$

where I_0 is the initial intensity of the probe beam.

For a thermal cloud having a gaussian shape with radii denoted $\sigma_{x',y',z'}$, the atomic density can be written as:

$$n(x', y', z') = \frac{N_0}{(2\pi)^{3/2} \sigma_{x'} \sigma_{y'} \sigma_{z'}} \exp\left(-\frac{x'^2}{2\sigma_{x'}^2}\right) \exp\left(-\frac{y'^2}{2\sigma_{y'}^2}\right) \exp\left(-\frac{z'^2}{2\sigma_{z'}^2}\right) \quad (\text{A.7})$$

and thus the atom number N_0 is obtained by integration of this density along x' , y' and z' . From equation A.6, N_0 is extracted from the three images taken by a two-dimensional integration:

$$N_0 = \frac{1}{2\lambda} \int \ln\left(\frac{I_{abs}(x', y') - I_b(x', y')}{I_0(x', y') - I_b(x', y')}\right) dx' dy' \quad (\text{A.8})$$

One has now to convert the integration over the continuous variables x' and y' into a summation over the pixels of the camera, by taking into account the magnification of the system g and the pixel size p . One pixel corresponds to a squared surface of size p/g in the volume containing the cloud:

$$N_0 = \frac{1}{2\lambda} \frac{p}{g} \sum_{k,l} \ln\left(\frac{I_{abs}(k, l) - I_b(k, l)}{I_0(k, l) - I_b(k, l)}\right) \quad (\text{A.9})$$

where k and l denotes the pixel numbers.

Since the probe profile is imaged on a 20% fraction of the CCD array, a squared box limits the range for the integration around it. Indeed outside the probe, one has $I_{abs}(k, l) \approx I_b(k, l) \approx I_0(k, l)$ and the corresponding pixels will produce non negligible numerical noise. Therefore they are not considered in the summation.

To obtain the widths of the cloud, the optical density is summed along one direction and fitted by a gaussian along the orthogonal direction. Nevertheless, because the probe beam is not propagating along one of the trap axis, the cloud widths related to the trapping frequencies (denoted σ_x and σ_y) are given by:

$$\sigma_x = \sigma_{x'} \tag{A.10}$$

$$\sigma_y = \sqrt{\frac{\sigma_{x'}^2 + \sigma_{y'}^2}{2}} \tag{A.11}$$

The determination of those quantities is essential to evaluate the cloud temperature as detailed in section A.3.

A.2 Polarisation

A.2.1 Degenerated system

The $2^3S_1 \rightarrow 2^3P_2$ transition used for imaging is not a pure two-level system as described in the previous section. Indeed both the initial and final states are degenerate in a zero magnetic field as depicted in figure A.2.

If the levels are degenerate, several transitions may be excited depending on the probe beam polarisation. The decay rate from m_j to m_i is a fraction $C_{i,j}$ of the total decay rate Γ , where $C_{i,j}$ is the $|\langle J_1 1 m_i (m_j - m_i) | J_1 1 J_2 m_j \rangle|^2$ Clebsch-Gordan coefficient. The values of the Clebsch-Gordan coefficients for the different $(2^3S_1, m_i) \rightarrow (2^3P_2, m_j)$ transitions are reported in figure A.2.

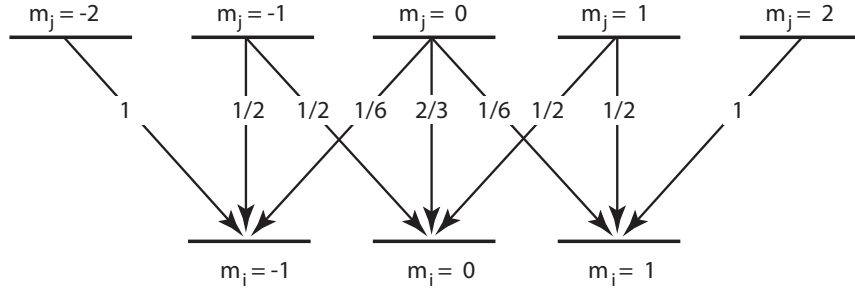


Figure A.2: Value of the Clebsch-Gordan coefficients C_{ij} for each subtransition $(J_2 = 2, m_j) \rightarrow (J_2 = 1, m_i)$. The relation $\sum_i C_{i,j} = 1$ is verified from each degenerate level m_j .

A.2.2 Imaging

Imaging of the MOT: In the MOT, the quadrupole field is pointing in all directions and no quantisation axis is properly defined. Taking this quantisation along the probe beam, the polarisation is linear during the imaging. Assuming that all sub-Zeeman levels of the 2^3S_1 metastable state are equally populated, with respective population denoted Π_i , three degenerate transitions are involved. The summation $\sum_j C_{ij} \Pi_i$ contributes for 5/9. This factor is taken into account in the analyses of the images.

Imaging of a magnetically trapped atomic cloud In the cloverleaf trap, the magnetic field direction is along the z axis of the magnetic trap and only the $m_i = 1$ state is populated. Imaging occurs only 1 or 2 ms after switching off the currents. At this time, the magnetic field is not zero and its direction depends on the inductance of the different coils. If one assumes that the compensation coils are responsible of the dominant magnetic field during the release of the atoms from the trap, the quantisation axis remains

along z during the imaging procedure.

The probe beam propagating at 45° of the quantisation axis contains then a mixture of circular and linear polarisations. The corresponding decomposition is: $(\frac{1}{\sqrt{2}}\pi, \frac{1}{2\sqrt{2}}\sigma_+, \frac{1}{2\sqrt{2}}\sigma_-)$ for the incoming beam and $(0, \frac{1}{2}\sigma_+, \frac{1}{2}\sigma_-)$ for the returning beam (see figure A.3). Assuming that the atoms remain in the $m_i=1$ during the switching of the fields, the corrective factor C reads:

$$C = \frac{1}{4\sqrt{2}} + \frac{1}{4} \left(1 + \frac{1}{\sqrt{2}}\right) + \frac{1}{24} \left(1 + \frac{1}{\sqrt{2}}\right) \approx 0.67. \quad (\text{A.12})$$

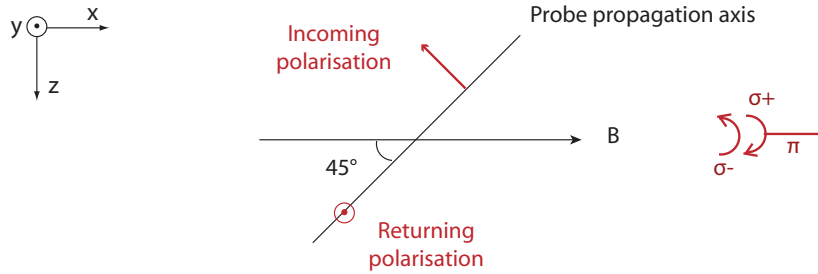


Figure A.3: *Schematic representation of the polarisation vectors of the probe beam, propagating along an axis making a 45° angle with the quantisation axis. The incoming beam polarisation can be decomposed as $(\frac{1}{\sqrt{2}}\pi, \frac{1}{2\sqrt{2}}\sigma_+, \frac{1}{2\sqrt{2}}\sigma_-)$. The retroreflected beam is a superposition of the two circular polarisations: $(0, \frac{1}{2}\sigma_+, \frac{1}{2}\sigma_-)$.*

The present analysis of the images from a magnetically trapped atomic cloud are realised under two assumptions: the direction of the field remains constant during the switching off of the magnetic field and the atoms remain in the $m_i=1$ Zeeman state. For a colder cloud, one could realise a Stern and Gerlach separation of the different spin states after the switching off of the fields to quantify the population in the different Zeeman-sublevels.

A.3 Linear absorption regime

The camera used is an Hamamatsu CCD camera with 512×512 pixels of $p = 24 \mu\text{m}$ size.

A.3.1 Long duration imaging

The low quantum efficiency of the CCD camera ($\eta_q = 0.02$) requires to send a large photon number onto the atomic cloud. One pixel can record at most $N_{max} = 2^{14}$ photoelectrons (14 bits memory CCD camera), setting a higher bound for the number of incident photons N_{inc} which has to be smaller than N_{max}/η_q . We typically work with $N_{mean} = N_{max}/4\eta_q$. For a probe duration of τ this corresponds to a minimal incident intensity expressed as:

$$I_{mean} = \frac{\hbar\omega_0 N_{max}}{4\eta_q \tau (p/g)^2} \quad (\text{A.13})$$

where p is the size of one pixel and g the magnification of the imaging system. In terms of the saturation parameter s , one gets:

$$s = \frac{I_{mean}}{I_{sat}} \quad (\text{A.14})$$

As one can notice from equation A.13, a small magnification g allows to image the atomic cloud over shorter durations τ for a fixed saturation parameter. However to have enough resolution on the spatial profile of the atomic cloud, the magnification has been fixed to $g = 0.75$. In these conditions, a typical BEC of length $100 \mu\text{m}$ is imaged in situ over 3 to 4 pixels.

With $g = 0.75$, a probing duration of $50 \mu\text{s}$ corresponds to $s \approx 1$. For this intensity range, the atom number is underestimated by a factor $\frac{1}{1+s}$ (see equation A.3 for resonant light). In order to remain in the linear absorption limit for which $s \ll 1$ we work with $\tau = 300 \mu\text{s}$ corresponding to $s = 0.1$.

A.3.2 Retroreflection of the imaging beam

While probing with a single pass beam, the cloud is disturbed and the atoms are detuned from resonance because of the Doppler shift. For Helium, the recoil velocity is $v_{rec} = \hbar k/m = 9.2 \text{ cm}\cdot\text{s}^{-1}$ with $k = 2\pi/\lambda_0$ the wave vector of the light. After α absorptions, the extra Doppler detuning is expressed as $\Delta = -\alpha k v_{rec}$. For a probe resonant with an atom at rest, the absorption rate defined in equation A.1 can be related to α :

$$\gamma_p = \frac{d\alpha}{dt} = \frac{\Gamma_0}{2} \frac{s}{1 + s + (2\alpha k v_{rec}/\Gamma_0)^2} \quad (\text{A.15})$$

The average time τ before n photons have been absorbed can be deduced from the discrete sum $\tau(n) = \sum_{\alpha=0}^n dt/d\alpha$. Introducing the velocity $v = n v_{rec}$ as the parameter instead of

the number of absorbed photons n , one obtains after summation:

$$\tau(v) = \frac{2}{\Gamma_0 s v_{rec}} \left(1 + s + \frac{4}{\Gamma_0^2} \left(\frac{1}{3} k^2 v^2 + \frac{1}{3} k^2 v v_{rec} + \frac{1}{6} k^2 v_{rec}^2 \right) \right) \quad (\text{A.16})$$

For large velocity v , the terms proportional to $v v_{rec}$ or v_{rec}^2 can be neglected. Solving equation A.16 with $s = 0.1$, an Helium atom absorbs up to 27 photons over 300 μs and the absorption rate drops by 88%.

To avoid this Doppler detuning, the probe beam is retroreflected to form a standing wave. The incoming beam and its retroreflection have orthogonal polarisations to prevent interferences. No more radiation pressure forces are exerted on the atoms which remain thus resonant with the probe, except for those due to an intensity imbalance in the two beams. Indeed, between 10% and 30% of the incoming beam intensity is absorbed by the cloud before being retroreflected (depending on the cloud optical density, higher in a molasse). It is therefore essential to have a low saturation parameter in order to reduce the radiation pressure forces as much as possible.

A.3.3 Imaging to probe the stray magnetic fields

Since the linewidth of the $2^3S_1 \rightarrow 2^3P_2$ is narrow ($\Gamma_0 = 2\pi \cdot 1.62$ MHz), a spectroscopy of the probe frequency allows to compensate or evaluate the stray magnetic fields.

Cancellation of the stray magnetic fields: In figure A.4, two scans of the probe frequency are realised in a zero field in a) and in a deliberate 3 G field along the direction of the Zeeman slower in b). In the first case, the 2 ± 0.2 MHz linewidth obtained from a lorentzian fit is in agreement with an intensity broadened linewidth $\Gamma_0 \sqrt{1+s}$, for $s = 0.4 \pm 0.15$ during the probing. The maximal atom number is obtained at resonance.

In presence of the magnetic field, three distinct lines can be observed corresponding to transitions between different m_i and m_j . Those data have been taken for a molasse where all the Zeeman sublevels are equally populated. In the presence of a magnetic field, the 2^3S_1 and 2^3P_2 levels are no longer degenerated and the detunings of all possible transitions are reported in figure A.4c) in MHz/G. Also the spectroscopy beam, propagating at 45° from the quantification axis contains all polarisations allowing to excite any transition. In a calibrated 3 G field, the detunings of the observed lines corresponds to the following transitions: (2) $m_i=0 \rightarrow m_j=0$, insensitive to the magnetic field, (1) $m_i=-1 \rightarrow m_j=-1$ (+ 0.7 MHz/G) and (3) $m_i=-1 \rightarrow m_j=-2$ (- 1.4 MHz/G). For smaller values of the magnetic field, the lines are no longer separated, but clearly disturb the symmetry of the lorentzian profile. This spectroscopy makes it possible to cancel the stray magnetic fields.

Magnetic field decay after switching off the magnetic trap: It is also possible to monitor the decay of the magnetic field after the switching off of the magnetic trap cur-

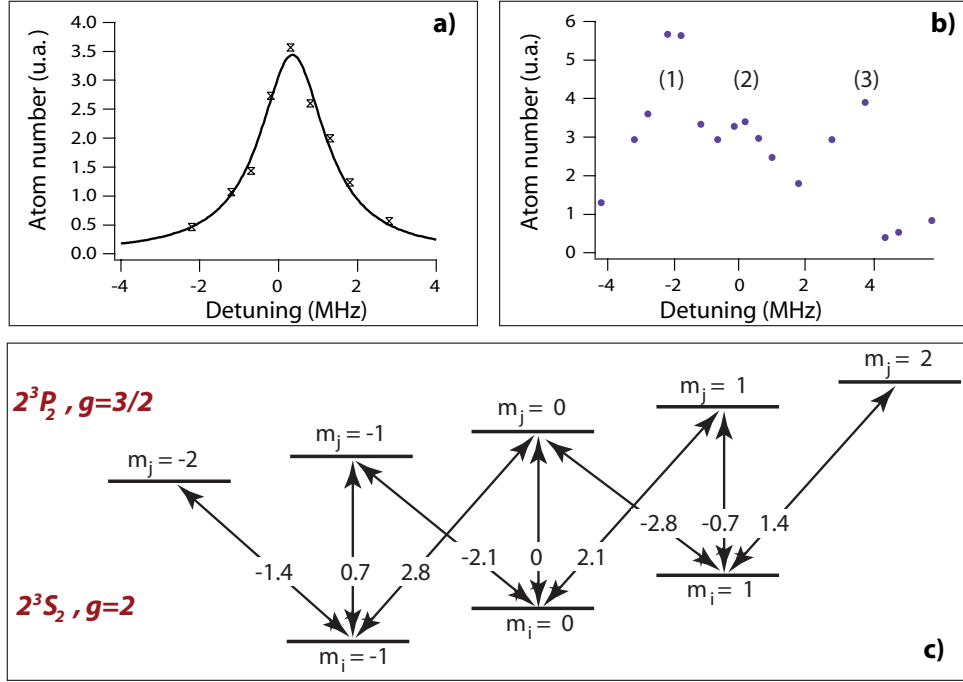


Figure A.4: a) Spectroscopy of the probe frequency after 1.5 ms time-of-flight of the atomic cloud initially trapped in the MOT. A lorentzian fit of the atom number gives the line center at resonance and a linewidth of 2 ± 0.2 MHz, larger than the natural linewidth due to residual stray magnetic fields. b) Spectroscopy of the probe frequency in a calibrated magnetic field along the Zeeman. Three lines corresponding to different optical transitions can be distinguished: $m_i=0 \rightarrow m_j=0$, insensitive to the magnetic field, $m_i=-1 \rightarrow m_j=-1$ and $m_i=-1 \rightarrow m_j=-2$. The positions of their center are in agreement with the corresponding detunings for a 3 G magnetic field as detailed in the text. c) Detuning from the resonance of the different possible $m_i \rightarrow m_j$ transitions in the presence of a magnetic field expressed in MHz/G. Since the 2^3S_1 and 2^3P_2 levels have different Lande factors g (as reported in the figure), only the $m_i=0 \rightarrow m_j=0$ transition is field insensitive.

rents from the evolution of the probe detuning with time as reported in figure A.5. In this case, the imaging transition is $m_i=1 \rightarrow m_j=2$ having a 1.4 MHz/G detuning from the resonance. The magnetic field decay shows two time scales: a fast exponential decay occurs during 2 ms, followed by a slower decay corresponding to the slow cancellation of the eddy currents. Given the temperature of the magnetically trapped cloud, time-of-flights longer than 4 ms could not be resolved. The time-of-flights shorter than 1.25 ms require a large detuning of the probe frequency for which the probe intensity was too small to image the atomic cloud.

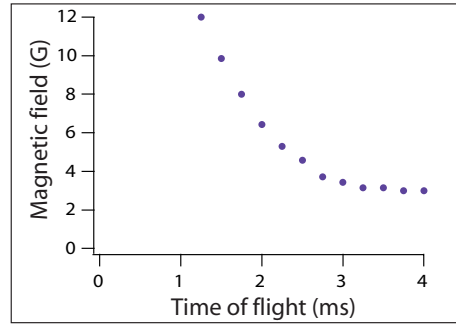


Figure A.5: *Magnetic field value corresponding to the probe detuning for different delays after switching off the currents in the magnetic trap. The curves shows a fast exponential during the 2 first ms followed by a much slower decay. The probe detuning remains almost constant detuning between 3 and 4 ms.*

A.3.4 Determination of the temperature

The temperature T is determined by the expansion of the cloud after being released from the trap. Along one direction, the width σ can be expressed as a function of time t :

$$\sigma(t) = \sqrt{\sigma_i^2 + \frac{k_B T}{m} t^2} \quad (\text{A.17})$$

with σ_i the initial width of the cloud along this direction. Many perturbative effects due to the long probing duration and the scattering of large photon number may have an impact on the temperature determination.

As a consequence of the long probing duration of the present imaging system, the cloud expansion is integrated during $\tau = 300 \mu\text{s}$. The averaged value of $\overline{\sigma(tp)}$ obtained from a gaussian fit of the integrated cloud profile is assimilated to the width of the cloud at the time t_p .

For $100 \mu\text{K} < T < 3 \text{ mK}$, it has been verified by numerical integration that this produces an error of at most 10% on the determination of the temperature (for measurements up to 4 ms time-of-flight as for typical data, see figure A.6 a)). For large time-of-flights, the width is simply proportional to time and the cloud width is always overestimated by the same quantity ($\Delta\sigma(t_p) = (k_B T/m)\tau$). This produces a global shift, but does not affect the slope and thus the temperature. The determination is only affected by the non-linear regime at short time-of-flights.

As the temperature reduces, the kinetics of the expansion is slower and the long probing duration affects less the temperature determination (figure A.6 b)). For $T < 100 \mu\text{K}$, errors are smaller than 6%.

Nevertheless, those errors are small compared to the statistical ones and can be neglected.

A red-detuned retro-reflected probe beam is analog to a 1D molasse, reducing the temperature along its axis. The spatial density density remains frozen over the probing time scale. The widths deduced from the gaussian fits on both direction are, in this limit, non perturbed by the imaging beam.

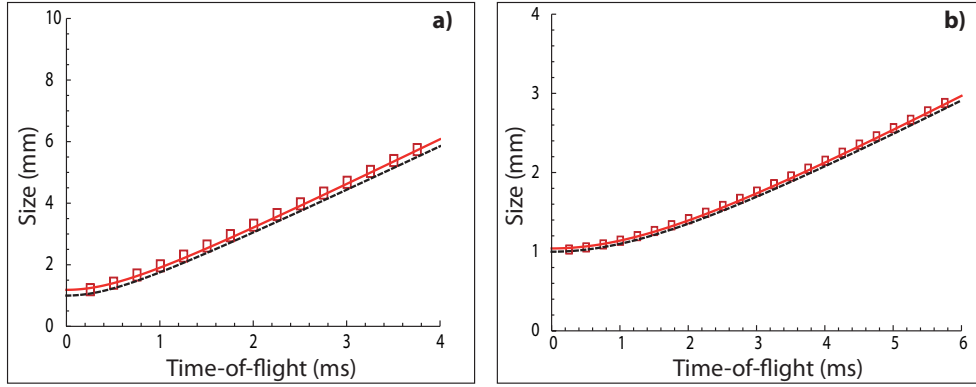


Figure A.6: a) Expansion of a cloud of initial width $\sigma_i = 1$ mm and of temperature $T = 1$ mK. The red data points represent the cloud width integrated over the $\tau = 300$ μ s probing duration, fitted by equation A.17. The dashed line represents the real evolution of the cloud width according to equation A.17. Neglecting the probing duration τ induces an error of 8% in the temperature determination. b) Same curves for $T = 100$ μ K. The temperature differs only by 3% with our determination.

Photon scattering also induces a broadening of the spatial distribution as detailed in [135]. The increase of the cloud widths is evaluated to be of the order of 0.2 mm and is therefore neglected.

It is worth noticing that the temperature has also been deduced from an RF spectroscopy in the magnetic trap and from the time-of-flight signal recorded on the channeltron. These three independent determinations are in good agreement as reported in chapter 2.

Appendix B

Frequency comb

Whereas frequencies up to 100 GHz are determined with a great accuracy with electronic counters, optical frequencies of several 100 THz are challenging to measure. The ten last years have shown a great advance in the control of the frequency spectrum produced by mode-locked lasers, which enable to generate a regular comb of frequency lines. For a sufficient broad comb, it is possible to determine the absolute frequencies of all the comb lines. This ability has revolutionised optical frequency metrology [114, 115].

In the group of W. Vassen (VU-Amsterdam), such a device allowed to both stabilise and measure accurately the frequency of the laser at 1560 nm exciting the $2^3S_1 \rightarrow 2^1S_0$ magnetic dipolar transition of metastable ^4He atoms as presented in chapter 5. This appendix is dedicated to the presentation of the general principle of a frequency comb, on which a complete review can be found in [124].

B.1 Mode locked lasers

This section is dedicated to the mode-locking technique, which produces the frequency spectrum of a frequency comb. It relies on the cancellation of the variations of the group velocity with the wavelength, so that the discrete frequencies selected by an optical cavity conserve a fixed phase relationship.

B.1.1 Compensation of the group velocity dispersion

The coupling of a continuous spectrum emitted by a laser into an optical cavity of length L produces a discrete set of frequencies. Constructive interference only occurs for frequencies ν_p such that the phase is repeated identically after a round trip through the cavity:

$$\nu_p = p \frac{c}{n(\nu_p)L} \quad (\text{B.1})$$

with c the speed of light and n the index of the cavity material. Those longitudinal modes oscillate independently from each other, as the phase of the light between different modes varies randomly. If many standing waves are coupled into the cavity, interference effects

tend to average to a near-constant output intensity.

Let us note $k(\omega)$ the wave vector of the electric field of the mode p , so that equation B.1 can simply be rewritten as $Lk(\omega_p) = 2\pi p$. Since the refractive index of the material depends on the frequency, the phase changes from mode to mode, so that each mode has a different phase velocity expressed as $v_{\phi,p} = \omega_p/k(\omega_p)$. If the variation of $k(\omega)$ is small around a central frequency denoted ω_c it can be developed following:

$$k(\omega) = k(\omega_c) + \left. \frac{dk}{d\omega} \right|_{\omega_c} (\omega - \omega_c) + \frac{1}{2} \left. \frac{d^2k}{d^2\omega} \right|_{\omega_c} (\omega - \omega_c)^2 + \frac{1}{6} \left. \frac{d^3k}{d^3\omega} \right|_{\omega_c} (\omega - \omega_c)^3 + O((\omega - \omega_c)^4). \quad (\text{B.2})$$

The second term corresponds to the delay introduced by the propagation through the cavity at a velocity $(\left. \frac{dk}{d\omega} \right|_{\omega_c})^{-1}$ called group velocity and denoted v_g , identical for all the longitudinal modes. The third term represents a dispersive effect, due to the variation of the group velocity with the frequency. Higher orders terms also contribute to further dispersion but significantly less.

From equation B.2, one can express the frequency difference between the mode p and $p + 1$ which is:

$$\omega_{p+1} - \omega_p = \frac{2\pi}{L} v_g - \frac{k''(\omega_c)}{2} v_g ((\omega_{p+1} - \omega_c)^2 - (\omega_p - \omega_c)^2) + O((\omega_p - \omega_c)^3) \quad (\text{B.3})$$

The dispersion of the group velocity $k''(\omega_c)$ and the terms of higher orders prevent to obtain a constant frequency spacing between consecutive longitudinal modes. In order to obtain a mode-locked laser, the dispersion of the group velocity along a round trip in the cavity is reduced as much as possible. In this case the frequency spacing between the longitudinal modes is fixed and equal to $\nu_{rep} = v_g/L$.

The first femtosecond lasers had an intra-cavity compensation for the group velocity dispersion, with two prisms expanding the optical path for the red-component of the spectrum.

A new solution relies on chirped mirrors having a negative group velocity. They consist of multiple layers of dielectric mirrors, whose widths increase with their depth. The layers reflect preferentially the blue wavelengths and the deepest one the red wavelengths. Accumulating several such mirrors in the cavity allows to equal in an acceptable way the optical length of the optical cavity seen by all the frequencies.

B.1.2 Spectrum of a mode-locked laser

For a mode-locked laser, all the longitudinal frequencies ν_p are equally spaced by ν_{rep} and centered around a central frequency denoted ν_c . Each longitudinal mode can thus be decomposed under the form: $\nu_p = \nu_c + n_p \nu_{rep}$. This spectrum spans an interval $\Delta\nu$, corresponding to the bandwidth of the laser injected into the optical cavity.

The width of each frequency peak of the comb resides in the quality factor of the cavity.

The electric field, $E(t)$, of the laser can thus be written as:

$$E(t) = \Re\left(\sum_n A_n e^{-i(\omega_c + n\omega_{rep})t}\right) = \Re\left(\left(\sum_n A_n e^{-in\omega_{rep}t}\right) e^{-i\omega_c t}\right) \quad (\text{B.4})$$

where the amplitudes A_n obey to a gaussian distribution of width $\Delta\omega$ and centered around ω_c .

In the second equality of equation B.4: $\sum_n A_n e^{-in\omega_{rep}t}$ corresponds to the Fourier transform of a periodical function $A(t)$ of period $2\pi/\omega_{rep}$. This shows that the temporal behaviour of the electric field is that of equally spaced laser pulses at a carrier frequency $\nu_c = \omega_c/2\pi$ and a temporal profil $A(t)$. The temporal width of such pulses is inversely proportional to the laser bandwidth following:

$$\Delta t = \frac{2 \ln(2)}{\pi} \frac{1}{\Delta\nu} \quad (\text{B.5})$$

for a gaussian distribution of the amplitudes A_n . Such pulsed lasers are widely used and achieve pulse duration of the order of 5 fs. The time-frequency correspondance for a mode-locked laser is depicted in figure B.1.

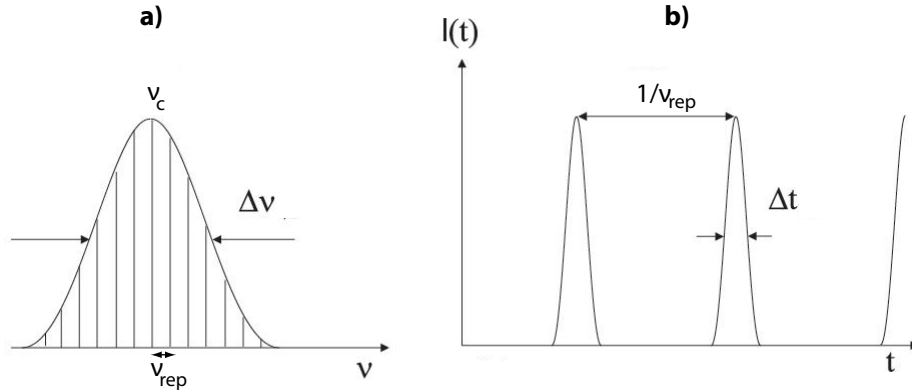


Figure B.1: a) Gaussian spectral intensity of a mode-locked laser. b) Corresponding intensity variation with time.

The dispersion inside the cavity results in a phase change after a round trip, denoted $\Delta\phi$:

$$\Delta\phi = \left(\frac{1}{v_g} - \frac{1}{v_\phi}\right) L\omega_c \bmod [2\pi] \quad (\text{B.6})$$

which shifts the carrier phase after each round trip with respect to the pulse envelope as depicted in figure B.2. Since this shift is affecting all the optical frequencies of the spectrum in the same way, it can be factorised and corresponds to an offset frequency ν_0 . As a consequence of the difference between phase and group velocities in the cavity, the central frequency ν_c is not an integer multiple of the repetition rate ν_{rep} and can be written as:

$$\nu_c = n_c \nu_{rep} + \nu_0 \quad (\text{B.7})$$

where $\nu_0 \leq \nu_{rep}$.

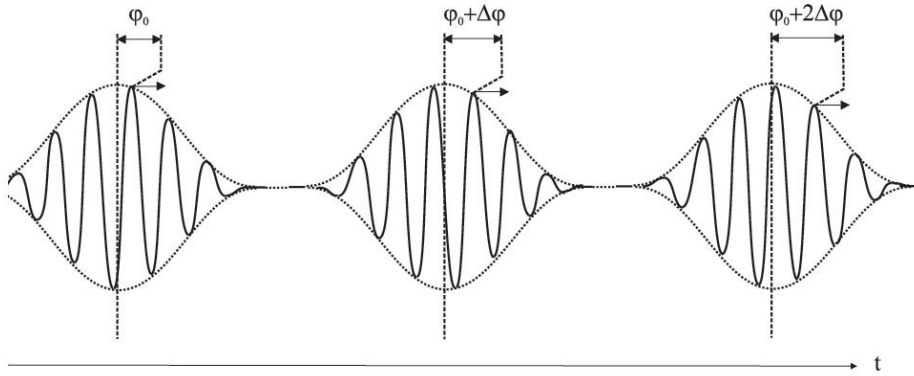


Figure B.2: *Evolution of the phase between successive pulses.*

To obtain the maximum laser bandwidth or the shortest pulse, spectrum broadening of monomode optical fibers has been first used. Recently, microstructured fibers (or photonic crystal fibers) have been designed [136], enlarging the spectrum up to 300 THz. Inside the fiber, the pulse spectrum is broadened by self-phase modulation due to the intensity dependent refractive index, soliton splitting, shock wave formation, and other nonlinear optical processes. The emerging white light can be dispersed with a grating to form a rainbow of colors. However, this is not ordinary white light. Remarkably, the processes generating the white light can be so highly reproducible that successive pulses are still correlated in their phases and can interfere in the spectrum to form a comb of several hundred thousand sharp spectral lines.

B.2 Frequency combs

For a frequency measurement to be absolute, it must be referenced to the hyperfine transition of ^{133}Cs that defines the second. The corresponding microwave frequency is defined to be exactly 9 192 631 770 Hz, which is approximately 10^5 smaller than optical frequencies. Thus a large frequency gap must be spanned to make an absolute optical frequency measurement.

The first optical frequency measurements required complex synthesis frequency chains, creating successive harmonics from the cesium radio frequency reference up to the optical domain. The choice of the studied transitions was constrained by the coincidence between the excitation laser and the etalon lasers available.

A laser frequency comb is the frequency spectrum of a mode locked laser, as depicted in figure B.3. As detailed in this section it provides a direct link between optical frequencies and microwave frequencies and makes it possible to realise an absolute measurement of optical frequencies.

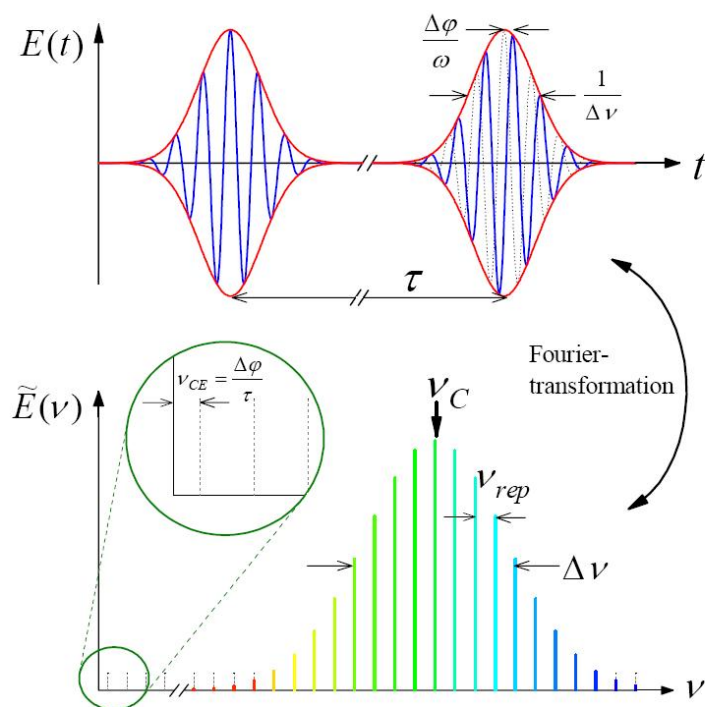


Figure B.3: *Fourier transformation of a mode-locked laser of carrier frequency ν_c and phase shift $\Delta\phi$, giving regular frequency lines spaced by ν_{rep} and offset by ν_0 .*

B.2.1 Absolute frequency measurement

The frequency spectrum of a comb relies on only two radio frequencies: the repetition rate ν_{rep} and the offset frequency ν_0 . Any unknown frequency ν can then be determined by first making a wavelength measurement with a conventional wavemeter that is sufficiently

accurate to determine the integer number m of the nearest comb line. The precise distance from this reference line is then measured by feeding a beat signal of frequency ν_{beat} to a microwave counter. It is thus essential to access and control the values of ν_{rep} and ν_0 to reconstitute the optical frequency ν given by:

$$\nu = \nu_0 + m\nu_{rep} + \nu_{beat} \quad (\text{B.8})$$

The repetition frequency ν_{rep} , typically of the order of 100 MHz, can be simply measured from a fast photodiode. This repetition rate is directly linked to the length of the cavity L , which fluctuates resulting for instance from temperature changes. ν_{rep} can thus be locked at a fixe value, retroacting on the length of the cavity, and referenced to a cesium or rubidium atomic clock.

The measurement of the offset frequency is not so simple. However, if the optical spectrum of the frequency comb spans an octave in frequency (meaning that the highest frequency is a factor of 2 larger than the lowest frequency), it is possible to access ν_0 from an interferometric measurement. A second harmonic crystal can be used to frequency double the lowest frequency having index k and produce almost the same frequency than the high-frequency comb line of index $2k$. Measuring the heterodyne beat between these yields a difference frequency:

$$2\nu_k - \nu_{2k} = 2(k\nu_{rep} + \nu_0) - (2k\nu_{rep} + \nu_0) = \nu_0 \quad (\text{B.9})$$

which is just the offset frequency. This scheme first proposed by T.W. Hansch [114] is called autoreferenced $f - 2f$. The control on ν_0 is realised via the power of the pump laser, which modifies the index of the non-linear fiber and thus the group velocity v_g from which the offset frequency depends.

B.2.2 Accuracy of an optical frequency measurement based on a frequency comb

Such a control on both ν_{rep} and ν_0 enables to synthesize several hundred thousands sharp optical reference frequencies which are precisely known in terms of the primary standard of time. The accuracy of an absolute frequency measurement using a frequency comb is thus linked to the quality of the radiofrequency standard, which is multiplied by a large integer m of the order of 10^5 . Experimental observation has clearly confirmed that the actual limitation with frequency comb measurements is the quality of the radio-frequency reference [137].

Optical clocks open the way to promising improvements of the accuracy of frequency measurements. Instead of running the frequency comb from microwave frequencies up to optical frequencies, it appears to be advantageous to stabilise the comb by an optical frequency standard. Such optical atomic clocks produce then stable clock signal in the radio-frequency domain [138, 139]. The most accurate absolute frequency determinations have been obtained using optical standards [140, 141].

Comparison between two separate frequency combs, both linked to a common reference source allows one to examine the intrinsic accuracy of the system, currently at a level of few parts in 10^{16} with no measurable systematic effects [142].

The metrology measurement, presented in chapter 5 relies on frequency comb technique allowing to reach a kHz accuracy on the laser frequency determination. In the Amsterdam VU laboratories, such combs are a daily used technique in the group of K. Eikema, working on high precision metrology. We had the opportunity to use a frequency comb based on a mode-locked erbium doped fiber laser at $1.5 \mu\text{m}$ (Menlo System) with a repetition rate of 250 MHz. Both the repetition rate and the carrier envelope offset frequency are referenced to a GPS-controlled Rubidium clock (PRS10 Stanford Research). Such a clock achieves an accuracy of about 5×10^{-12} .

B.3 Determination of an absolute optical frequency using two combs

This section describes a technique used at the VU in Amsterdam during my stay in the group of Wim Vassen to determine the absolute frequency of the infrared laser at $1.5 \mu\text{m}$. The laser frequency was referenced to one of the comb (Erbium doped) in order to insure its long term stability as described in chapter ???. As mentioned in section B.2, the integer number m of the nearest comb line can be obtained from a first measurement with a spectrometer having an accuracy smaller than ν_{rep} . Lacking a spectrometer, this integer can also be retrieved from two successive measurements with different values of ν_{rep} so that:

$$\nu_l = \nu_0 + m_1\nu_{rep,1} + \nu_{beat,1} \quad (\text{B.10})$$

$$= \nu_0 + m_2\nu_{rep,2} + \nu_{beat,2} \quad (\text{B.11})$$

and thus $m_1\nu_{rep,1} - m_2\nu_{rep,2} = \nu_{beat,2} - \nu_{beat,1}$, which can be solved for integer couples (m_1, m_2) .

Because of the large temporal drift of the laser, such a measurement was not possible. Therefore a second comb, centered around 800 nm , has been used to obtain two simultaneous measurements of the laser frequency. A part of the laser light was frequency doubled in a PPLN crystal (Thorlabs) and the beat frequency with the nearest comb modes both at 1557 nm and 778.5 nm were measured simultaneously leading to the following equation:

$$\nu_l = \nu_{0,1} + m_1\nu_{rep,1} + \nu_{beat,1} = 2(\nu_{0,2} + m_2\nu_{rep,2} + \nu_{beat,2}) \quad (\text{B.12})$$

where m_1 and m_2 are two unknown integers.

From this equation m_2 can be expressed as a function of m_1 . m_1 can be varied around its probable value and the fractional part of the resulting m_2 can be evaluated ($m_2 - E(m_2)$, where $E(x)$ denotes the integer part of x). This provides typically one pair of integers (m_1, m_2) fulfilling equation B.12 over 0.12 nm as shown in figure B.4.

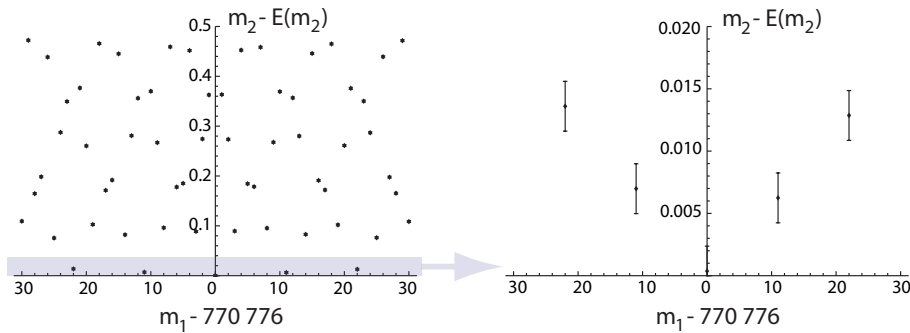


Figure B.4: Fractional part of m_2 as a function of the integer m_1 recentered around its most favorable value 770776 . The right graph corresponds to a zoom of the first graph around zero, selecting the most favorable value for m_1 . The error bar provided corresponds to the measurement error on $\nu_{beat,1}$ and $\nu_{beat,2}$. Only one pair of integers (m_1, m_2) fulfill the relation B.12 over a span of 15 GHz corresponding to 0.12 nm .

Bibliography

- [1] M. H. Anderson, J. R. Ensher, M. R. Matthews, C. E. Wieman, and E. A. Cornell. Observation of Bose - Einstein condensation in a dilute atomic vapor. *Science*, 269(5221):198–201, 1995. URL: <http://www.sciencemag.org/cgi/content/abstract/269/5221/198>, doi:10.1126/science.269.5221.198.
- [2] K. B. Davis, M. O. Mewes, M. R. Andrews, N. J. van Druten, D. S. Durfee, D. M. Kurn, and W. Ketterle. Bose-Einstein condensation in a gas of sodium atoms. *Phys. Rev. Lett.*, 75(22):3969–3973, Nov 1995. URL: <http://link.aps.org/abstract/PRL/v75/p3969>, doi:10.1103/PhysRevLett.75.3969.
- [3] C. C. Bradley, C. A. Sackett, J. J. Tollett, and R. G. Hulet. Evidence of Bose-Einstein condensation in an atomic gas with attractive interactions. *Phys. Rev. Lett.*, 75(9):1687–1690, Aug 1995. URL: <http://link.aps.org/abstract/PRL/v75/p1687>, doi:10.1103/PhysRevLett.75.1687.
- [4] F. London. The lambda-phenomenon of liquid helium and the bose-einstein degeneracy. *Nature*, 141:643, 1938.
- [5] A. Einstein. Quantentheorie des einatomigen idealen gases. *Sitzungsber. Kgl. Preuss. Aka. Wiss.*, 1924:261, 1924.
- [6] L.D. Landau and V.L. Ginzburg. On the theory of superconductivity. *JETP*, 20:1064, 1950.
- [7] E.P. Gross. Structure of a quantized vortex in boson system. *Il Nuovo Cimento*, 20:454, 1961.
- [8] L. P. Pitaevskii. Vortex lines in an imperfect bose gas. *Sov. Phys. JETP*, 13:451, 1961.
- [9] Franco Dalfovo, Stefano Giorgini, Lev P. Pitaevskii, and Sandro Stringari. Theory of bose-einstein condensation in trapped gases. *Rev. Mod. Phys.*, 71(3):463–512, Apr 1999. doi:10.1103/RevModPhys.71.463.
- [10] Anthony J. Leggett. Bose-einstein condensation in the alkali gases: Some fundamental concepts. *Rev. Mod. Phys.*, 73(2):307–356, Apr 2001. doi:10.1103/RevModPhys.73.307.
- [11] C. J. Pethick and H. Smith. *Bose-Einstein condensation in dilute gases*. Cambridge University Press, 2002.

- [12] L. P. Pitaevskii and S. Stringari. *Bose-Einstein Condensation*. Clarendon Press, 2003.
- [13] B. DeMarco and D. Jin. Onset of fermi degeneracy in a trapped atomic gas. *Science*, 285:5434, 1999.
- [14] F. Schreck, L. Khaykovich, K. L. Corwin, G. Ferrari, T. Bourdel, J. Cubizolles, and C. Salomon. Quasipure bose-einstein condensate immersed in a fermi sea. *Phys. Rev. Lett.*, 87(8):080403, Aug 2001. doi:10.1103/PhysRevLett.87.080403.
- [15] A. Truscott, K. Strecker, W. McAlexander, G. B. Partridge, and R. G. Hulet. Observation of fermi pressure in a gas of trapped atoms. *Science*, 291:2570, 2001.
- [16] Ph. Courteille, R. S. Freeland, D. J. Heinzen, F. A. van Abeelen, and B. J. Verhaar. Observation of a Feshbach resonance in cold atom scattering. *Phys. Rev. Lett.*, 81(1):69–72, Jul 1998. URL: <http://link.aps.org/doi/10.1103/PhysRevLett.81.69>, doi:10.1103/PhysRevLett.81.69.
- [17] S. Inouye, M. R. Andrews, J. Stenger, H.-J. Miesner, D. M. Stamper-Kurn, and W. Ketterle. Observation of feshbach resonances in a bose-einstein condensate. *Nature*, 392:151, 1998.
- [18] Immanuel Bloch, Jean Dalibard, and Wilhelm Zwerger. Many-body physics with ultracold gases. *Rev. Mod. Phys.*, 80(3):885–964, Jul 2008. doi:10.1103/RevModPhys.80.885.
- [19] R. Feynman. Simulating physics with computers. *International journal of theoretical physics*, 21:467, 1982.
- [20] T. Jelte, J. M. McNamara, W. Hogervorst, V. Vassen, W. and Krachmalnicoff, M. Schellekens, A. Perrin, H. Chang, D. Boiron, A. Aspect, and C. I. Westbrook. Comparison of the hanbury browntwiss effect for bosons and fermions. *Nature*, 445:402–405, 2007.
- [21] P. J. Leo, V. Venturi, I. B. Whittingham, and J. F. Babb. Ultracold collisions of metastable helium atoms. *Phys. Rev. A*, 64(4):042710, Sep 2001. doi:10.1103/PhysRevA.64.042710.
- [22] G. V. Shlyapnikov, J. T. M. Walraven, U. M. Rahmanov, and M. W. Reynolds. Decay kinetics and Bose condensation in a gas of spin-polarized triplet helium. *Phys. Rev. Lett.*, 73(24):3247–3250, Dec 1994. URL: <http://link.aps.org/doi/10.1103/PhysRevLett.73.3247>, doi:10.1103/PhysRevLett.73.3247.
- [23] P. O. Fedichev, M. W. Reynolds, U. M. Rahmanov, and G. V. Shlyapnikov. Inelastic decay processes in a gas of spin-polarized triplet helium. *Phys. Rev. A*, 53(3):1447–1453, Mar 1996. URL: <http://link.aps.org/doi/10.1103/PhysRevA.53.1447>, doi:10.1103/PhysRevA.53.1447.
- [24] O. Sirjean, S. Seidelin, J. Viana Gomes, D. Boiron, C. I. Westbrook, A. Aspect, and G. V. Shlyapnikov. Ionization rates in a bose-einstein condensate of metastable

- helium. *Phys. Rev. Lett.*, 89(22):220406, Nov 2002. doi:10.1103/PhysRevLett.89.220406.
- [25] A. Robert, O. Sirjean, A. Browaeys, J. Poupard, S. Nowak, D. Biron, C. I. Westbrook, and A. Aspect. A Bose-Einstein condensate of metastable atoms. *Science*, 292(5516):461–464, 2001. URL: <http://www.sciencemag.org/cgi/content/abstract/292/5516/461>, arXiv:<http://www.sciencemag.org/cgi/reprint/292/5516/461.pdf>, doi:10.1126/science.1060622.
- [26] F. Pereira Dos Santos, J. Léonard, Junmin Wang, C.J. Barrelet, F. Perales, E. Rasel, C.S. Unnikrishnan, M. Leduc, and C. Cohen-Tannoudji. Production of a Bose Einstein condensate of metastable helium atoms. *The European Physical Journal D*, 19(1):103–109, apr 2002. URL: <http://dx.doi.org/10.1140/epjd/e20020061>, doi:10.1140/epjd/e20020061.
- [27] A. S. Tychkov, T. Jeltsov, J. M. McNamara, P. J. J. Tol, N. Herschbach, W. Hogervorst, and W. Vassen. Metastable helium bose-einstein condensate with a large number of atoms. *Phys. Rev. A*, 73(3):031603, Mar 2006. doi:10.1103/PhysRevA.73.031603.
- [28] R. G. Dall and A. G. Truscott. Bose-Einstein condensation of metastable helium in a bi-planar quadrupole Ioffe configuration trap. *Optics Communications*, 270:255–261, feb 2007. URL: <http://dx.doi.org/10.1016/j.optcom.2006.09.031>, doi:10.1016/j.optcom.2006.09.031.
- [29] S. Charles Doret, Colin B. Connolly, Wolfgang Ketterle, and John M. Doyle. Buffer-gas cooled bose-einstein condensate. *Phys. Rev. Lett.*, 103(10):103005, Sep 2009. doi:10.1103/PhysRevLett.103.103005.
- [30] V. P. Mogendorff, E. J. D. Vredenbregt, and H. C. W. Beijerinck. Coupled-channel analysis of ne^* thermalization cross section. *Phys. Rev. A*, 73(1):012712, Jan 2006. doi:10.1103/PhysRevA.73.012712.
- [31] P. Spoden, M. Zinner, N. Herschbach, W. J. van Drunen, W. Ertmer, and G. Birkl. Collisional properties of cold spin-polarized metastable neon atoms. *Phys. Rev. Lett.*, 94(22):223201, Jun 2005. doi:10.1103/PhysRevLett.94.223201.
- [32] K. J. Matherson, R. D. Glover, D. E. Laban, and R. T. Sang. Measurement of low-energy total absolute atomic collision cross sections with the metastable 3p_2 state of neon using a magneto-optical trap. *Phys. Rev. A*, 78(4):042712, Oct 2008. doi:10.1103/PhysRevA.78.042712.
- [33] G. Drake and Z.-C Yan. High precision spectroscopy as a test of quantum electrodynamics in light atomic systems. *Canadian Journal of Physics*, 86:45–54, 2008.
- [34] J. C. J. Koelemeij, R. J. W. Stas, W. Hogervorst, and W. Vassen. Magneto-optical trap for metastable helium at 389 nm. *Phys. Rev. A*, 67(5):053406, May 2003. doi:10.1103/PhysRevA.67.053406.

- [35] P. Cancio Pastor, G. Giusfredi, P. De Natale, G. Hagel, C. de Mauro, and M. Inguscio. Absolute frequency measurements of the $2^3s_1 \rightarrow 2^3p_{0,1,2}$ atomic helium transitions around 1083 nm. *Phys. Rev. Lett.*, 92(2):023001, Jan 2004. doi:10.1103/PhysRevLett.92.023001.
- [36] Michal Przybytek and Bogumil Jeziorski. Bounds for the scattering length of spin-polarized helium from high-accuracy electronic structure calculations. *The Journal of Chemical Physics*, 123(13):134315, 2005. URL: <http://link.aip.org/link/?JCP/123/134315/1>, doi:10.1063/1.2042453.
- [37] J. Kim, U. D. Rapol, S. Moal, M. Walhout, and M. Leduc. Photoassociation experiments with ultracold metastable helium. *The European Physical Journal D*, 31:227, 2004.
- [38] S. Moal, M. Portier, J. Kim, J. Dugue, U. D. Rapol, M. Leduc, and C. Cohen-Tannoudji. Accurate determination of the scattering length of metastable helium atoms using dark resonances between atoms and exotic molecules. *Physical Review Letters*, 96(2):023203, 2006. URL: <http://link.aps.org/abstract/PRL/v96/e023203>, doi:10.1103/PhysRevLett.96.023203.
- [39] S. Moal, M. Portier, N. Zahzam, and M. Leduc. Lifetime of weakly bound dimers of ultracold metastable helium studied by photoassociation. *Phys. Rev. A*, 75(3):033415, Mar 2007. doi:10.1103/PhysRevA.75.033415.
- [40] Timothy J. Beams, Gillian Peach, and Ian B. Whittingham. Spin-dipole-induced lifetime of the least-bound $^5\sigma_g^+$ state of $he(2^3s_1) + he(2^3s_1)$. *Phys. Rev. A*, 74(1):014702, Jul 2006. doi:10.1103/PhysRevA.74.014702.
- [41] G. B. Partridge, J.-C. Jaskula, M. Bonneau, D. Boiron, and C. I. Westbrook. Bose-einstein condensation and spin mixtures of optically trapped metastable helium. *Phys. Rev. A*, 81(5):053631, May 2010. doi:10.1103/PhysRevA.81.053631.
- [42] Vanderlei Bagnato, David E. Pritchard, and Daniel Kleppner. Bose-einstein condensation in an external potential. *Phys. Rev. A*, 35(10):4354–4358, May 1987. doi:10.1103/PhysRevA.35.4354.
- [43] M. Olshanii. Atomic scattering in the presence of an external confinement and a gas of impenetrable bosons. *Phys. Rev. Lett.*, 81(5):938–941, Aug 1998. doi:10.1103/PhysRevLett.81.938.
- [44] T. Bergeman, M. G. Moore, and M. Olshanii. Atom-atom scattering under cylindrical harmonic confinement: Numerical and analytic studies of the confinement induced resonance. *Phys. Rev. Lett.*, 91(16):163201, Oct 2003. doi:10.1103/PhysRevLett.91.163201.
- [45] D. S. Petrov, M. Holzmann, and G. V. Shlyapnikov. Bose-einstein condensation in quasi-2d trapped gases. *Phys. Rev. Lett.*, 84(12):2551–2555, Mar 2000. doi:10.1103/PhysRevLett.84.2551.

- [46] D. S. Petrov and G. V. Shlyapnikov. Interatomic collisions in a tightly confined bose gas. *Phys. Rev. A*, 64(1):012706, Jun 2001. doi:10.1103/PhysRevA.64.012706.
- [47] T. L. Gustavson, A. P. Chikkatur, A. E. Leanhardt, A. Görlitz, S. Gupta, D. E. Pritchard, and W. Ketterle. Transport of bose-einstein condensates with optical tweezers. *Phys. Rev. Lett.*, 88(2):020401, Dec 2001. doi:10.1103/PhysRevLett.88.020401.
- [48] T. Kinoshita, B. Engeser, and D. S. Weiss. Observation of a one-dimensional tonks-girardeau gas. *Science*, 305:1125, 2004.
- [49] D. Rychtarik, B. Engeser, H.-C. Nägerl, and R. Grimm. Two-dimensional bose-einstein condensate in an optical surface trap. *Phys. Rev. Lett.*, 92(17):173003, Apr 2004. doi:10.1103/PhysRevLett.92.173003.
- [50] Elmar Haller, Mattias Gustavsson, Manfred J. Mark, Johann G. Danzl, Russell Hart, Guido Pupillo, and Hanns-Christoph Nägerl. Realization of an excited, strongly-correlated quantum gas phase. *Science*, 325:1224, 2009.
- [51] Elmar Haller, Manfred J. Mark, Russell Hart, Johann G. Danzl, Lukas Reichsöllner, Vladimir Melezhik, Peter Schmelcher, and Hanns-Christoph Nägerl. Confinement-induced resonances in low-dimensional quantum systems. *Phys. Rev. Lett.*, 104(15):153203, Apr 2010. doi:10.1103/PhysRevLett.104.153203.
- [52] G. Lamporesi, J. Catani, G. Barontini, Y. Nishida, M. Inguscio, and F. Minardi. Scattering in mixed dimensions with ultracold gases. *Phys. Rev. Lett.*, 104(15):153202, Apr 2010. doi:10.1103/PhysRevLett.104.153202.
- [53] D. Jaksch, C. Bruder, J. I. Cirac, C. W. Gardiner, and P. Zoller. Cold bosonic atoms in optical lattices. *Phys. Rev. Lett.*, 81(15):3108–3111, Oct 1998. URL: <http://link.aps.org/doi/10.1103/PhysRevLett.81.3108>, doi:10.1103/PhysRevLett.81.3108.
- [54] Markus Greiner, Olaf Mandel, Tilman Esslinger, Theodor W. Hansch, and Immanuel Bloch. Quantum phase transition from a Superfluid to a Mott insulator in a gas of ultracold atoms. *Nature*, 415(6867):39–44, 2002. URL: <http://dx.doi.org/10.1038/415039a>, doi:doi:10.1038/415039a.
- [55] S. Diehl, A. Micheli, A. Kantian, B. Kraus, H.P. Buchler, and P. Zoller. Quantum states and phases in driven open quantum systems with cold atoms. *Nature Physics*, 4:878, 2008.
- [56] N. Syassen, D. M. Bauer, T. Volz, D. Dietze, J. J. Garcia-Ripoll, J. I. Cirac, G. Rempe, and S. Durr. Strong dissipation inhibits losses and induces correlations in cold molecular gases. *Science*, 320:1329, 2008.
- [57] J. Dugué. *Sources Ultrafroides Avancées pour l'Interférométrie et la Physique Atomique*. PhD thesis, 2009.

- [58] J. Pereira Dos Santos, F. *Condensation de Bose-Einstein de l'hélium métastable*. PhD thesis, Université Pierre et Marie Curie, 2002. URL: <http://tel.archives-ouvertes.fr/tel-00002267>.
- [59] William D. Phillips and Harold Metcalf. Laser deceleration of an atomic beam. *Phys. Rev. Lett.*, 48(9):596–599, Mar 1982. URL: <http://link.aps.org/doi/10.1103/PhysRevLett.48.596>, doi:10.1103/PhysRevLett.48.596.
- [60] E. L. Raab, M. Prentiss, Alex Cable, Steven Chu, and D. E. Pritchard. Trapping of neutral sodium atoms with radiation pressure. *Phys. Rev. Lett.*, 59(23):2631–2634, Dec 1987. doi:10.1103/PhysRevLett.59.2631.
- [61] A. Browaeys. Two body loss rate in a magneto-optical trap of metastable helium. *Eur. Phys. J. D.*, 8:199, 2000.
- [62] Markus Greiner, Immanuel Bloch, Theodor W. Hänsch, and Tilman Esslinger. Magnetic transport of trapped cold atoms over a large distance. *Phys. Rev. A*, 63(3):031401, Feb 2001. doi:10.1103/PhysRevA.63.031401.
- [63] H. J. Lewandowski, D. M. Harber, D. L. Whitaker, and E. A. Cornell. Simplified system for creating a bose-einstein condensate. *Journal of Low Temperature Physics*, 132(5/6):309, Sept 2003.
- [64] Alan L. Migdall, John V. Prodan, William D. Phillips, Thomas H. Bergeman, and Harold J. Metcalf. First observation of magnetically trapped neutral atoms. *Phys. Rev. Lett.*, 54(24):2596–2599, Jun 1985. doi:10.1103/PhysRevLett.54.2596.
- [65] Wolfgang Petrich, Michael H. Anderson, Jason R. Ensher, and Eric A. Cornell. Stable, tightly confining magnetic trap for evaporative cooling of neutral atoms. *Phys. Rev. Lett.*, 74(17):3352–3355, Apr 1995. doi:10.1103/PhysRevLett.74.3352.
- [66] M.-O. Mewes, M. R. Andrews, N. J. van Druten, D. M. Kurn, D. S. Durfee, and W. Ketterle. Bose-einstein condensation in a tightly confining dc magnetic trap. *Phys. Rev. Lett.*, 77(3):416–419, Jul 1996. doi:10.1103/PhysRevLett.77.416.
- [67] T. Bergeman, Gidon Erez, and Harold J. Metcalf. Magnetostatic trapping fields for neutral atoms. *Phys. Rev. A*, 35(4):1535–1546, Feb 1987. doi:10.1103/PhysRevA.35.1535.
- [68] P. D. Lett, W. D. Phillips, S. L. Rolston, C. E. Tanner, R. N. Watts, and C. I. Westbrook. Optical molasses. *J. Opt. Soc. Am. B*, 6:2084, 1989.
- [69] Durfee D. S. Ketterle, W. and D. M. Stamper-Kurn. Making, probing and understanding bose-einstein condensates. *Proceedings of the International School of Physics "Enrico Fermi"*, Course CXL, 1999. doi:cond-mat/9904034.
- [70] P. O. Schmidt, S. Hensler, J. Werner, T. Binhammer, A. Gorlitz, and T. Pfau. Doppler cooling of an optically dense cloud of magnetically trapped atoms. *J. Opt. Soc. Am. B*, 20:960, 2003.

- [71] A. Tychkov. *Bose-Einstein condensation of metastable helium atoms*. PhD thesis, Vreij Universiteit - Amsterdam, 2008.
- [72] T. Jelten. *Quantum Statistical effects in ultracold gases of metastable helium*. PhD thesis, Vreij Universiteit - Amsterdam, 2008.
- [73] V. Krachmalnicoff. *Deux expériences de corrélations quantiques sur des gaz d'Hélium métastable: dégroupement de fermions et étude de bosons corrélés par collision de condensats*. PhD thesis, Université Paris XI, 2009.
- [74] Harald F. Hess. Evaporative cooling of magnetically trapped and compressed spin-polarized hydrogen. *Phys. Rev. B*, 34(5):3476–3479, Sep 1986. URL: <http://link.aps.org/doi/10.1103/PhysRevB.34.3476>, doi:10.1103/PhysRevB.34.3476.
- [75] A. G. Martin, K. Helmerson, V. S. Bagnato, G. P. Lafyatis, and D. E. Pritchard. rf spectroscopy of trapped neutral atoms. *Phys. Rev. Lett.*, 61(21):2431–2434, Nov 1988. doi:10.1103/PhysRevLett.61.2431.
- [76] C. Cohen-Tannoudji. Piégeage non dissipatif d'atomes neutres et refroidissement évaporatif. In *Cours de Physique atomique et moléculaire, Collège de France*, 1996.
- [77] D. Guéry-Odelin. *Dynamique collisionnelle des gaz d'alcalins lourds: du refroidissement évaporatif à la condensation de Bose-Einstein*. PhD thesis, Université Paris VI, 1998.
- [78] C. R. Monroe, E. A. Cornell, C. A. Sackett, C. J. Myatt, and C. E. Wieman. Measurement of cs-cs elastic scattering at $t=30 \mu\text{k}$. *Phys. Rev. Lett.*, 70:414, 1993.
- [79] H. Wu and C. Foot. Direct simulation of evaporative cooling. *J. Phys. B.*, 29:L321, 1996.
- [80] D. E. Pritchard, E. L. Raab, V. Bagnato, C. E. Wieman, and R. N. Watts. Light traps using spontaneous forces. *Phys. Rev. Lett.*, 57(3):310–313, Jul 1986. doi:10.1103/PhysRevLett.57.310.
- [81] Alan L. Migdall, John V. Prodan, William D. Phillips, Thomas H. Bergeman, and Harold J. Metcalf. First observation of magnetically trapped neutral atoms. *Phys. Rev. Lett.*, 54(24):2596–2599, Jun 1985. doi:10.1103/PhysRevLett.54.2596.
- [82] T. Bergeman, Gidon Erez, and Harold J. Metcalf. Magnetostatic trapping fields for neutral atoms. *Phys. Rev. A*, 35(4):1535–1546, Feb 1987. doi:10.1103/PhysRevA.35.1535.
- [83] Steven Chu, J. E. Bjorkholm, A. Ashkin, and A. Cable. Experimental observation of optically trapped atoms. *Phys. Rev. Lett.*, 57(3):314–317, Jul 1986. URL: <http://link.aps.org/doi/10.1103/PhysRevLett.57.314>, doi:10.1103/PhysRevLett.57.314.
- [84] M. D. Barrett, J. A. Sauer, and M. S. Chapman. All-optical formation of an atomic bose-einstein condensate. *Phys. Rev. Lett.*, 87(1):010404, Jun 2001. doi:10.1103/PhysRevLett.87.010404.

- [85] S. R. Granade, M. E. Gehm, K. M. O'Hara, and J. E. Thomas. All-optical production of a degenerate fermi gas. *Phys. Rev. Lett.*, 88(12):120405, Mar 2002. doi:10.1103/PhysRevLett.88.120405.
- [86] R. Grimm, M. Weidemüller, and Y. B. Ovchinnikov. *Advances in atomic, molecular and optical physics*. Academic Press, 2000.
- [87] Cohen-Tannoudji C. Dalibard, J. Dressed-atom approach to atomic motion in laser light: the dipole force revisited. *J.O.S.A.*, 2:1707, 1985.
- [88] Dupont-Roc J. Grynberg G. Cohen-Tannoudji, C. *Processus d'interaction entre photons et atomes*. Editions du CNRS, 1996.
- [89] Nir Davidson, Heun Jin Lee, Charles S. Adams, Mark Kasevich, and Steven Chu. Long atomic coherence times in an optical dipole trap. *Phys. Rev. Lett.*, 74(8):1311–1314, Feb 1995. URL: <http://link.aps.org/doi/10.1103/PhysRevLett.74.1311>, doi:10.1103/PhysRevLett.74.1311.
- [90] Roe Ozeri, Lev Khaykovich, and Nir Davidson. Long spin relaxation times in a single-beam blue-detuned optical trap. *Phys. Rev. A*, 59(3):R1750–R1753, Mar 1999. URL: <http://link.aps.org/doi/10.1103/PhysRevA.59.R1750>, doi:10.1103/PhysRevA.59.R1750.
- [91] J.P. Dowling and J. GeaBanaclouche. Evanescent light-wave atom mirrors, resonators waveguides and traps. *Advances in Atomic, Molecular, and Optical Physics*, 37:1–94, 1996.
- [92] J. Léonard. *Photo-association de l'hélium métastable au voisinage de la condensation de Bose-Einstein et formation de dimères géants*. PhD thesis, Université Pierre et Marie Curie, 2003. URL: <http://tel.archives-ouvertes.fr/tel-00004295>.
- [93] Zong-Chao Yan and J. F. Babb. Long-range interactions of metastable helium atoms. *Phys. Rev. A*, 58(2):1247–1252, Aug 1998. doi:10.1103/PhysRevA.58.1247.
- [94] J. Stärck and W. Meyer. Long-range interaction potential of the $3[\sigma]g+$ state of he2. *Chemical Physics Letters*, 225(1-3):229–232, 1994. URL: <http://www.sciencedirect.com/science/article/B6TFN-44WCW8J-75/2/043679120e0c27207a076bf270d97339>.
- [95] F. X. Gad
ea, T. Leininger, and A. S. Dickinson. Calculated scattering length for spin-polarized metastable helium. *Journal of Chemical Physics*, 117:7122, 2002.
- [96] A. S. Dickinson, F. X. Gad
ea, and T. Leininger. Scattering lengths for spin-polarized metastable helium-3 and helium-4. *J. Phys. B.*, 37:587, 2004.
- [97] C. Cohen-Tannoudji, B. Diu, and F. Laloë. *Mécanique Quantique*. Hermann, 1973.

- [98] M. Portier. *Molécules exotiques d'Hélium*. PhD thesis, Université Pierre et Marie Curie (Paris VI), 2007.
- [99] M. W. Müller, A. Merz, M. W. Ruf, H. Hotop, W. Meyer, and M. Movre. Experimental and theoretical studies of the Bi-excited collision systems $\text{He}^*(23\text{S})+\text{He}^*(23\text{S}, 21\text{S})$ at thermal and subthermal kinetic energies. *Zeitschrift für Physik D Atoms, Molecules and Clusters*, 21(2):89–112, 1991. URL: <http://dx.doi.org/10.1007/BF01425589>.
- [100] J. J. Garcia-Ripoll, S. Duerr, N. Syassen, D. M. Bauer, M. Lettner, G. Rempe, and I. Cirac. Dissipation-induced hard-core boson gas in an optical lattice. *New Journal of Physics*, 11:013053, 2009.
- [101] B. Fröhlich, M. Feld, E. Vogt, M. Koschorreck, W. Zwerger, and M. Köhl. Radiofrequency spectroscopy of a strongly interacting two-dimensional Fermi gas. *ArXiv e-prints*, November 2010. [arXiv:1012.0049](https://arxiv.org/abs/1012.0049).
- [102] Z. Hadzibabic, P. Kruger, M. Cheneau, S.P. Rath, and J. Dalibard. The trapped two-dimensional bose gas: from bose-einstein condensation to berezinskii-kosterlitz-thouless physics. *New Journal of Physics*, 10:045006, 2008.
- [103] Matthew P. A. Fisher, Peter B. Weichman, G. Grinstein, and Daniel S. Fisher. Boson localization and the superfluid-insulator transition. *Phys. Rev. B*, 40(1):546–570, Jul 1989. URL: <http://link.aps.org/doi/10.1103/PhysRevB.40.546>, doi: 10.1103/PhysRevB.40.546.
- [104] C. Orzel, S. D. Bergeson, S. Kulin, and S. L. Rolston. Time-resolved studies of ultracold ionizing collisions. *Phys. Rev. Lett.*, 80(23):5093–5096, Jun 1998. doi: 10.1103/PhysRevLett.80.5093.
- [105] Hideyuki Kunugita, Tetsuya Ido, and Fujio Shimizu. Ionizing collisional rate of metastable rare-gas atoms in an optical lattice. *Phys. Rev. Lett.*, 79(4):621–624, Jul 1997. doi:10.1103/PhysRevLett.79.621.
- [106] A. J. Daley, J. M. Taylor, S. Diehl, M. Baranov, and P. Zoller. Atomic three-body loss as a dynamical three-body interaction. *Phys. Rev. Lett.*, 102(4):040402, Jan 2009. doi:10.1103/PhysRevLett.102.040402.
- [107] Wilhelm Zwerger. Mott-Hubbard transition of cold atoms in optical lattices. *Journal of Optics B: Quantum and Semiclassical Optics*, 5(2):S9–S16, 2003. URL: <http://stacks.iop.org/1464-4266/5/S9>, doi:10.1088/1464-4266/5/2/352.
- [108] Immanuel Bloch, Markus Greiner, Olaf Mandel, and Theodor W. Hänsch. Coherent cold collisions with neutral atoms in optical lattices. *Philosophical Transactions of the Royal Society A: Mathematical, Physical and Engineering Sciences*, 361(1808):1409–1416, 2003. URL: <http://dx.doi.org/10.1098/rsta.2003.1210>, doi:10.1098/rsta.2003.1210.
- [109] C. Dorrer, F. Nez, B. de Beauvoir, L. Julien, and F. Biraben. Accurate measurement of the $2^3s_1 - 3^3d_1$ two-photon transition frequency in helium: New determination of

- the 2^3s_1 lamb shift. *Phys. Rev. Lett.*, 78(19):3658–3661, May 1997. doi:10.1103/PhysRevLett.78.3658.
- [110] W. Lichten, D. Shiner, and Zhi-Xiang Zhou. Measurement of the lamb shifts in singlet levels of atomic helium. *Phys. Rev. A*, 43(3):1663–1665, Feb 1991. doi:10.1103/PhysRevA.43.1663.
- [111] F. Pereira Dos Santos, J. Léonard, Junmin Wang, C.J. Barrelet, F. Perales, E. Rasel, C.S. Unnikrishnan, M. Leduc, and C. Cohen-Tannoudji. Production of a Bose-Einstein condensate of metastable helium atoms. *The European Physical Journal D*, 19(1):103–109, apr 2002. URL: <http://dx.doi.org/doi/10.1140/epjd/e20020061>, doi:10.1140/epjd/e20020061.
- [112] R. J. W. Stas, J. M. McNamara, W. Hogervorst, and W. Vassen. Simultaneous magneto-optical trapping of a boson-fermion mixture of metastable helium atoms. *Phys. Rev. Lett.*, 93(5):053001, Jul 2004. doi:10.1103/PhysRevLett.93.053001.
- [113] J. M. McNamara, T. Jeltès, A. S. Tychkov, W. Hogervorst, and W. Vassen. Degenerate bose-fermi mixture of metastable atoms. *Phys. Rev. Lett.*, 97(8):080404, Aug 2006. doi:10.1103/PhysRevLett.97.080404.
- [114] R. Holzwarth, Th. Udem, T. W. Hänsch, J. C. Knight, W. J. Wadsworth, and P. St. J. Russell. Optical frequency synthesizer for precision spectroscopy. *Phys. Rev. Lett.*, 85(11):2264–2267, Sep 2000. doi:10.1103/PhysRevLett.85.2264.
- [115] Scott A. Diddams, David J. Jones, Jun Ye, Steven T. Cundiff, John L. Hall, Jinnendra K. Ranka, Robert S. Windeler, Ronald Holzwarth, Thomas Udem, and T. W. Hänsch. Direct link between microwave and optical frequencies with a 300 thz femtosecond laser comb. *Phys. Rev. Lett.*, 84(22):5102–5105, May 2000. doi:10.1103/PhysRevLett.84.5102.
- [116] Grzegorz Łach and Krzysztof Pachucki. Forbidden transitions in the helium atom. *Phys. Rev. A*, 64(4):042510, Sep 2001. doi:10.1103/PhysRevA.64.042510.
- [117] R. J. W. Stas. *Trapping fermionic and bosonic helium atoms*. PhD thesis, Vrije Universiteit - Amsterdam, 2005.
- [118] K. S. E. Eikema, W. Ubachs, W. Vassen, and W. Hogervorst. Precision measurements in helium at 58 nm: Ground state lamb shift and the 1^1s - 2^1p transition isotope shift. *Phys. Rev. Lett.*, 76(8):1216–1219, Feb 1996. doi:10.1103/PhysRevLett.76.1216.
- [119] Craig J. Sansonetti and J. D. Gillaspay. Absolute ionization energy of the 2^1s level of helium. *Phys. Rev. A*, 45(1):R1–R3, Jan 1992. doi:10.1103/PhysRevA.45.R1.
- [120] F. S. Pavone, F. Marin, P. De Natale, M. Inguscio, and F. Biraben. First pure frequency measurement of an optical transition in helium: Lamb shift of the 2^3s_1 metastable level. *Phys. Rev. Lett.*, 73(1):42–45, Jul 1994. doi:10.1103/PhysRevLett.73.42.

- [121] P. Mueller, L.-B. Wang, G. W. F. Drake, K. Bailey, Z.-T. Lu, and T. P. O'Connor. Fine structure of the $1s3p\ ^3p_J$ level in atomic ^4He : Theory and experiment. *Phys. Rev. Lett.*, 94(13):133001, Apr 2005. doi:10.1103/PhysRevLett.94.133001.
- [122] Robert S. Van Dyck, Charles E. Johnson, and Howard A. Shugart. Radiative lifetime of the $2\ ^1s_0$ metastable state of helium. *Phys. Rev. A*, 4(4):1327–1336, Oct 1971. doi:10.1103/PhysRevA.4.1327.
- [123] D.C. Morton, Q. Wu, and G. Drake. Energy levels for the stable isotopes of atomic helium. *Canadian Journal of Physics*, 84:83–105, 2006.
- [124] Steven T. Cundiff and Jun Ye. Colloquium: Femtosecond optical frequency combs. *Rev. Mod. Phys.*, 75(1):325–342, Mar 2003. doi:10.1103/RevModPhys.75.325.
- [125] A. L. Wolf, S. A. van den Berg, C. Gohle, E. J. Salumbides, W. Ubachs, and K. S. E. Eikema. Frequency metrology on the $4s^2s_{1?2} - -4p^2p_{1?2}$ transition in $^{40}\text{Ca}^+$ for a comparison with quasar data. *Phys. Rev. A*, 78(3):032511, Sep 2008. doi:10.1103/PhysRevA.78.032511.
- [126] A. L. Wolf, S. A. van den Berg, W. Ubachs, and K. S. E. Eikema. Direct frequency comb spectroscopy of trapped ions. *Phys. Rev. Lett.*, 102(22):223901, Jun 2009. doi:10.1103/PhysRevLett.102.223901.
- [127] Dominik Z. Kandula, Christoph Gohle, Tjeerd J. Pinkert, Wim Ubachs, and Kjeld S. E. Eikema. Extreme ultraviolet frequency comb metrology. *Phys. Rev. Lett.*, 105(6):063001, Aug 2010. doi:10.1103/PhysRevLett.105.063001.
- [128] Thomas C. Killian, Dale G. Fried, Lorenz Willmann, David Landhuis, Stephen C. Moss, Thomas J. Greytak, and Daniel Kleppner. Cold collision frequency shift of the $1s-2s$ transition in hydrogen. *Phys. Rev. Lett.*, 81(18):3807–3810, Nov 1998. doi:10.1103/PhysRevLett.81.3807.
- [129] O. Sirjean. *Collisions ionisantes: un nouveau diagnostic pour les condensats d'Hélium métastable*. PhD thesis, Université Paris XI, Orsay, 2003.
- [130] Ionut D. Prodan, Marin Pichler, Mark Junker, Randall G. Hulet, and John L. Bohn. Intensity dependence of photoassociation in a quantum degenerate atomic gas. *Phys. Rev. Lett.*, 91(8):080402, Aug 2003. doi:10.1103/PhysRevLett.91.080402.
- [131] Thomas Gasenzer. High-light-intensity photoassociation in a bose-einstein condensate. *Phys. Rev. A*, 70(2):021603, Aug 2004. doi:10.1103/PhysRevA.70.021603.
- [132] Pascal Naidon and Françoise Masnou-Seeuws. Pair dynamics in the formation of molecules in a bose-einstein condensate. *Phys. Rev. A*, 68(3):033612, Sep 2003. doi:10.1103/PhysRevA.68.033612.
- [133] Pascal Naidon and Françoise Masnou-Seeuws. Photoassociation and optical feshbach resonances in an atomic bose-einstein condensate: Treatment of correlation effects. *Phys. Rev. A*, 73(4):043611, Apr 2006. doi:10.1103/PhysRevA.73.043611.
- [134] H. J. Metcalf and P. van der Straten. *Laser Cooling and Trapping*. Springer, 1999.

- [135] M. A. Joffe, W. Ketterle, A. Marin, and D. E. Pritchard. Transverse cooling and deflection of an atomic beam inside a zeeman slower. *JOSA B*, 10:2257, 1993.
- [136] J. K. Ranka, R. S. Windeler, and A. J. Stentz. Visible continuum generation in air-silica microstructure optical fibers with anomalous dispersion at 800 nm. *Opt. Lett.*, 25:25, 2000.
- [137] J. Ye, J. L. Hall, and S. A. Diddams. Precision phase control of ultrawide bandwidth laser - a network of ultrastable frequency marks across the visible spectrum. *Opt. Lett.*, 25:1675, 2000.
- [138] et al. Diddams, S. A. An optical clock based on a single trapped hg-199(+) ion. *Science*, 293:825, 2001.
- [139] Jun Ye, Long Sheng Ma, and John L. Hall. Molecular iodine clock. *Phys. Rev. Lett.*, 87(27):270801, Dec 2001. doi:10.1103/PhysRevLett.87.270801.
- [140] M. Niering, R. Holzwarth, J. Reichert, P. Pokasov, Th. Udem, M. Weitz, T. W. Hänsch, P. Lemonde, G. Santarelli, M. Abgrall, P. Laurent, C. Salomon, and A. Clairon. Measurement of the hydrogen 1s- 2s transition frequency by phase coherent comparison with a microwave cesium fountain clock. *Phys. Rev. Lett.*, 84(24):5496–5499, Jun 2000. doi:10.1103/PhysRevLett.84.5496.
- [141] X. Baillard, M. Fouché, R. Le Targat, P. G. Westergaard, A. Lecallier, F. Chapelet, M. Abgrall, G. D. Rovera, P. Laurent, P. Rosenbusch, S. Bize, G. Santarelli, A. Clairon, P. Lemonde, G. Grosche, B. Lipphardt, and H. Schnatz. An optical lattice clock with spin-polarized ^{87}Sr atoms. *The European Physical Journal D - Atomic, Molecular, Optical and Plasma Physics*, 48:11–17, 2008. 10.1140/epjd/e2007-00330-3. URL: <http://dx.doi.org/10.1140/epjd/e2007-00330-3>.
- [142] S. A. Diddams, L. Hollberg, S. A. Ma, and L. Robertsson. Femtosecond-laser-based optical clockwork with instability smaller than 6.3×10^{-16} in 1s. *Opt. Lett.*, 27:58, 2002.

Résumé :

Les thématiques abordées dans ce mémoire illustrent deux spécificités des gaz ultra-froids d'Hélium métastable : la possibilité de comparer les résultats expérimentaux à des évaluations théoriques précises (niveaux d'énergie, potentiels d'interaction) et une méthode de détection originale fournie par les ionisations Penning.

Nous présentons la construction et la caractérisation d'un nouveau piège magnétique offrant un large accès optique et permettant ainsi de combiner la production d'un condensat de Bose-Einstein et son chargement *in situ* dans un réseau optique 3D.

Les fondements théoriques des expériences prévues dans ces potentiels optiques sont ensuite détaillés. Dans un piège dipolaire croisé, l'influence du champ magnétique, devenu un paramètre libre, sur les taux de collisions Penning peut être mesurée et comparée à une nouvelle évaluation théorique.

Concernant l'Hélium dans des réseaux optiques, deux sujets sont développés : l'effet du confinement sur les collisions inélastiques Penning (réseau 1D), ainsi que la modélisation des pertes Penning dans un modèle de Bose-Hubbard dissipatif (réseau 3D).

Enfin, nous présentons la première mesure directe de la transition dipolaire magnétique $2^3S_1 \rightarrow 2^3P_2$, liant les familles singulet et triplet de l' ^4He . Cette expérience de spectroscopie, réalisée dans le groupe de W. Vassen, allie le domaine des atomes froids aux techniques des peignes de fréquences, afin d'obtenir une précision de 5 kHz.

Summary :

The thematics treated in this manuscript illustrate two specificities of ultracold metastable Helium gases: the ability to compare experimental measurement with precise theoretical evaluations (simplicity of the atomic structure) and to easily detect products of Penning ionisations.

We present the building and the characterisation of a novel magnetic trap with large optical access, allowing to combine the production of a Bose-Einstein condensate with its *in situ* loading into a 3D optical lattice.

The theoretical fundamentals of the experiments planned in those optical potentials are then detailed. In a crossed dipole trap, the influence of the magnetic field, now a free parameter, on the Penning collision rates can be measured and compared to a new theoretical evaluation.

Concerning Helium in optical lattices, two subjects are developed: the effect of the confinement on the inelastic Penning collisions (1D optical lattice) and the modelisation of the Penning losses via a dissipative Bose-Hubbard model (3D lattice).

Finally we present the first direct measurement of the dipolar magnetic transition $2^3S_1 \rightarrow 2^3P_2$, linking the singlet and triplet families in ^4He . This spectroscopy experiment, realised in the group of W. Vassen, combines cold atoms knowledge with the frequency comb technique, in order to reach an accuracy of 5 kHz.